Search for physics beyond the Standard Model in photon + missing transverse momentum final state in proton-proton collisions using the Compact Muon Solenoid detector at the Large Hadron Collider

By
Shamik Ghosh
PHYS05201304015

Saha Institute of Nuclear Physics, Kolkata

A thesis submitted to the

Board of Studies in Physical Sciences

In partial fulfillment of requirements
For the Degree of
DOCTOR OF PHILOSOPHY
of
HOMI BHABHA NATIONAL INSTITUTE

December, 2019

Homi Bhabha National Institute[1]

Recommendations of the Viva Voce Committee

As members of the Viva Voce Committee, we certify that we have read the dissertation prepared by **Shamik Ghosh** entitled **Search for physics beyond the Standard Model in photon + missing transverse momentum final state in proton-proton collisions using the Compact Muon Solenoid detector at the Large Hadron Collider** and recommend that it maybe accepted as fulfilling the dissertation requirement for the Degree of Doctor of Philosophy.

Subir Sarkar Date: 11/03/2020

Chairman - Prof. Subir Sarkar

Satyaki Bhattacharya Date: 11/03/2020

Guide / Convener - Prof. Satyaki Bhattacharya

Anjan Ananda Sen Date: 11/03/2020

Examiner - Prof. Anjan Ananda Sen

Suchandra Dutta Date: 11/3/2020

Member 1- Prof. Suchandra Dutta

Debasish Majumdar Date: 11/03/2020

Member 2- Prof. Debasish Majumdar

Final approval and acceptance of this thesis is contingent upon the candidate's submission of the final copies of the thesis to HBNI.

I/We hereby certify that I/we have read this thesis prepared under my/our direction and recommend that it may be accepted as fulfilling the thesis requirement.

Date: 11/03/2020 **Guide :** Satyaki Bhattacharya

Prof. Satyaki Bhattacharya

Place: SINP, KOLKATA

---

1 This page is to be included only for final submission after successful completion of viva voce.

STATEMENT BY AUTHOR

This dissertation has been submitted in partial fulfillment of requirements for an advanced degree at Homi Bhabha National Institute (HBNI) and is deposited in the Library to be made available to borrowers under rules of the HBNI.

Brief quotations from this dissertation are allowable without special permission, provided that accurate acknowledgement of source is made. Requests for permission for extended quotation from or reproduction of this manuscript in whole or in part may be granted by the Competent Authority of HBNI when in his or her judgment the proposed use of the material is in the interests of scholarship. In all other instances, however, permission must be obtained from the author.

Shamik Ghosh

Shamik Ghosh

DECLARATION

I, hereby declare that the investigation presented in the thesis has been carried out by me. The work is original and has not been submitted earlier as a whole or in part for a degree / diploma at this or any other Institution / University.

Shamik Ghosh

Shamik Ghosh

List of Publications arising from the thesis

Journal

1. CMS collaboration, Search for new physics in the monophoton final state in proton-proton collisions at $\sqrt{s} = 13$TeV.
   JHEP 10 (2017) 073

2. CMS collaboration, Search for new physics in final states with a single photon and missing transverse momentum in proton-proton collisions at $\sqrt{s} = 13$ TeV.
   JHEP 02 (2019) 074

3. S.Ghosh, A. Harilal, A.R. Saharanshu, S. Bhattacharya, R. Singh, A simulation study to distinguish prompt photon from π^0 and beam halo in a granular calorimeter using deep networks.
   JINST 14 P01011 (2019)

Conference Proceedings

1. Large Extra Dimensions search in the photon + MET final state in pp Collisions at $\sqrt{s} = 13$ TeV at CMS in LHC
   XXII DAE-BRNS High Energy Physics Symposium, 12-16 Dec 2016, University of Delhi, Delhi (India)
   Springer Proceedings in Physics, vol 203. Springer, Cham.

Shamik Ghosh

Shamik Ghosh

Conference Presentations

1. Large Extra Dimensions search in the photon + MET final state in pp Collisions at $\sqrt{s} = 13$ TeV at CMS in LHC

   XXII DAE-BRNS High Energy Physics Symposium, 12-16 Dec 2016, University of Delhi, Delhi (India)

   Poster presentation

2. Searches for dark matter in CMS in non-hadronic final states

   ICHEP2018: 39th International Conference on High Energy Physics, 4-11 Jul 2018, Seoul (Republic Of Korea)

   Poster presentation

3. Searches for dark matter in non-hadronic final states at CMS

   SUSY2018: 26th International Conference on Supersymmetry and Unification of Fundamental Interactions, 23-27 Jul 2018, Barcelona (Spain)

   Oral Presentation

4. Search for dark matter with CMS in final state with missing ET and a single photon

   DAE-HEP 2018: XXIII DAE-BRNS High Energy Physics Symposium, 10-14 Dec 2018, Chennai (India)

   Oral Presentation

5. A simulation study to distinguish prompt photon from π^0 and beam halo in a granular calorimeter using deep networks

   DAE-HEP 2018: XXIII DAE-BRNS High Energy Physics Symposium, 10-14 Dec 2018, Chennai (India)

   Poster Presentation

Shamik Ghosh

Shamik Ghosh

DEDICATIONS

Dedicated to Ma and Baba

ACKNOWLEDGEMENTS

First of all I would like to express my utmost gratitude to my supervisor Prof. Satyaki Bhattacharya for his guidance and for introducing me to the exciting world of high energy physics experiments. His enthusiasm and curiosity about physics and life has been contagious and a great source of motivation. His mentorship has often extended beyond academics and helped me immensely in this journey.

I also have had the good fortune of working with Prof. Sunanda Banerjee, my time with whom has been a continuous lesson in discipline, perseverance and humility. I sincerely thank him for all the things I could learn from him. Along with him I would like to thank Shikha di for making my time away from home at Fermilab so much more bearable. I would also like to thank Prof. Suchandra Dutta and Prof. Subir Sarkar for their constant support and guidance both in academics and administration. Also I would like to thank Mr. Pradip Dutta Sharma for being very helpful and considerate with administrative issues.

I have been lucky to work with all the wonderful people in 249, exchanging ideas and learning things together. I thank my seniors Sourav da, Ashim da, Suvankar da, Kuntal da, Atanu da and Kalyan da for their help and support; my batchmates Rome, Sukannya, Sourav, Rajarshi and Anisa, and my juniors Gourab, Pritam, Wadut, Debabrata, Sayan, Satyaki and Aranya for the wonderful environment we shared together, and the good friendships we formed, some of which I hope will last forever.

I would like to thank Shilpi di for being a truly kind and supportive senior, who was always there to help out with all kinds of problems in spite of her busy schedule. I would like to thank Bhawna for her help and contributions as a leader of our analysis group. I would also like to thank Arnab, Pingal, Sudipta, Suvayan and Kamal for being the best of friends one could ever hope for, right from our Masters days and sticking with me through thick and thin. I would like to thank Abhirami for being a great friend and for supporting me through a lot of tough times. I will always cherish the joy of exploring and discovering new ideas together.

Finally I would like to thank my family: my parents, my sister, my grandparents and my uncle for the unconditional love and faith they have bestowed upon me. Their sacrifices and unwavering support have made possible whatever miniscule contribution I could make to this vast ocean of science and I am thankful for every bit of it.

Contents

List of Figures

List of Tables

Summary

After the discovery of the Higgs boson, important physics goal of the LHC for the future include the search for BSM physics like Dark Matter and extra dimensions which are motivated by the presence of strong evidence from other sources particularly in the case of DM from astronomical observations. Dark Matter as well as ADD gravitons are invisible particles which give rise to missing transverse momentum(MET) and can be produced along with visible particles like a photon or a jet enabling us to hunt for them. Although jets have much higher event rates, photons give a cleaner final state with much greater control over backgrounds and have proved to be a very important channel both in ATLAS and CMS.

In this thesis, a search for new physics beyond the standard model at the LHC using data collected by CMS at center of mass energy 13TeV in final states with a single photon and large missing transverse momentum has been reported. There has been no observation of any deviation from Standard Model predictions and most stringent limits have been set on DM pair production and ADD extra dimension scenarios by employing novel techniques. For DM simplified models the observed (expected) lower limit on the mediator mass has been set at 950 (1150) GeV for dark matter mass around 1 GeV. For ADD model of large extra dimensions, for number of extra dimensions between 3 and 6, effective Planck scale $M_D$up to 2.85 to 2.90 TeV have been excluded.

Collimated neutral pion decays and machine induced backgrounds like beam halo photons have been very important backgrounds for the physics analysis descibed in the thesis and also for most other analyses with photons, but their estimations using traditional techniques described in the thesis have a lot of limitations. This has prompted the exploration of machine learning techniques to estimate these backgrounds using raw detector information. This thesis reports a new way of estimating experimental backgrounds using state of the art machine learning techniques for computer vision like deep Convolutional neural networks which has been shown to provide more powerful tests for hypothesis testing than traditionally employed techniques. This method is generic in scope and can be applied to any calorimeter with granular information.

Proper calibration of the calorimeters is an important aspect of an experiment which is

essential for proper measurements of jet energies and this thesis describes the calibration of CMS Hadron Calorimeter with isolated pions. An iterative method has been used for the calibration of HCAL with data taken by the detector during 2016. The calibration factors extracted with this method has been used to properly set the energy scale of the HCAL and has been used by all physics analyses carried out in CMS with 2016 data.

Summary

After the discovery of the Higgs boson, important physics goal of the LHC for the future include the search for BSM physics like Dark Matter and extra dimensions which are motivated by the presence of strong evidence from other sources particularly in the case of DM from astronomical observations. Dark Matter as well as ADD gravitons are invisible particles which give rise to missing transverse momentum(MET) and can be produced along with visible particles like a photon or a jet enabling us to hunt for them. Although jets have much higher event rates, photons give a cleaner final state with much greater control over backgrounds and have proved to be a very important channel both in ATLAS and CMS.

In this thesis, a search for new physics beyond the standard model at the LHC using data collected by CMS at center of mass energy 13TeV in final states with a single photon and large missing transverse momentum has been reported. There has been no observation of any deviation from Standard Model predictions and most stringent limits have been set on DM pair production and ADD extra dimension scenarios by employing novel techniques. For DM simplified models the observed (expected) lower limit on the mediator mass has been set at 950 (1150) GeV for dark matter mass around 1 GeV. For ADD model of large extra dimensions, for number of extra dimensions between 3 and 6, effective Planck scale $M_D$up to 2.85 to 2.90 TeV have been excluded.

Collimated neutral pion decays and machine induced backgrounds like beam halo photons have been very important backgrounds for the physics analysis descibed in the thesis and also for most other analyses with photons, but their estimations using traditional techniques described in the thesis have a lot of limitations. This has prompted the exploration of machine learning techniques to estimate these backgrounds using raw detector information. This thesis reports a new way of estimating experimental backgrounds using state of the art machine learning techniques for computer vision like deep Convolutional neural networks which has been shown to provide more powerful tests for hypothesis testing than traditionally employed techniques. This method is generic in scope and can be applied to any calorimeter with granular information.

Proper calibration of the calorimeters is an important aspect of an experiment which is essential for proper measurements of jet energies and this thesis describes the calibration of CMS Hadron Calorimeter with isolated pions. An iterative method has been used for the calibration of HCAL with data taken by the detector during 2016. The calibration factors extracted with this method has been used to properly set the energy scale of the HCAL and has been used by all physics analyses carried out in CMS with 2016 data.

Chapter 1

Introduction

The Standard Model(SM) of particle physics provides the best description of nature till date. It describes three of the four known fundamental interactions known to us and classifies all the elementary particles we have observed yet. It has been tested to high precision in many experiments. In spite of all its glory SM fails to explain the hierarchy problem and the nature of Dark Matter(DM) among others. DM particles can be produced in high energy proton-proton collisions at LHC if they interact with SM particles at the electroweak scale through new couplings and though these particles cannot be directly detected with detectors its their presence can be inferred from observation of events having large transverse momentum imbalance. Similarly the hierarchy problem has a proposed solution in the ADD(Arkani-Hamed, Dimopoulos, Dvali) model where compactified extra dimensions and gravitons are introduced where the gravitons can propagate in the extra as well as regular 4 dimensions unlike the SM particles. These gravitons also cannot be directly observed and hence their presence can be inferred from observation of events having large transverse momentum imbalance.

This thesis examines final states with large missing transverse momentum and a single photon with large transverse momentum and looks for an excess in events over the SM prediction. An excess or the lack of it is interpreted in terms of DM pair production as well as ADD graviton production. This thesis analyses data collected by Compact Muon Solenoid(CMS), one of the two general purpose detectors at LHC. The thesis is structured as follows. Chapter 2 gives a brief theoretical overview of SM and beyond SM theories which are relevant for the analysis. Chapter 3 describes briefly the layouts of the LHC and CMS with its various subdetectors. Reconstruction of collisions events and physics objects are discussed in Chapter 4. Chapter 5 describes in details the analysis performed with the data collected during 2016 run of LHC at center-of-mass energy 13TeV. Chapter 6 proposes an alternative approach to estimate some backgrounds of the analysis using machine learning techniques which show better efficiency than methods used traditionally.

Finally the last chapter of the thesis describes the calibration of the Hadron Calorimeter of the CMS using isolated tracks using data collected during 2016 run of LHC.

Chapter 2

The Theoretical Perspective

2.1 Standard Model of Elementary Particles

The Standard Model (SM) is a relativistic field theory which relates the fundamental interactions of elementary and composite particles. It is described by $SU(3)_C \otimes SU(2)_L \otimes U(1)_Y$ gauge theory. SM consists of Quantum Chromodynamic, which describes strong interaction and electro-weak theory which describes electromagnetic and weak interactions. SM has been validated by many experiments until now with high precision. According to SM matter is made up of fermions (described by Fermi-Dirac statistics) which are the elementary articles and the interaction between them is mediated by bosons (described by Bose-Einstein statistics). Fermions can be further categorized into two types : quarks and leptons. Both of them have no substructure and are defined by their mass and quantum number shown in Tables 2.1, 2.2. Table 2.3 shows the spin 1 bosons that mediate the forces. Photons mediate the electromagnetic force, gluons mediate the strong force whereas W± and Z bosons mediate the weak force.

Table 2.1: Standard Model particles : Leptons

Generation	leptons	mass(MeV/c^2)	charge (e)	spin
First	electron (e)	0.51	-1	1/2
	electron neutrino (ν_e)	$< 2 \times 10^{-6}$	0	1/2
Second	muon (μ)	105.7	-1	1/2
	muon neutrino (ν_μ)	< 0.19	0	1/2
Third	tau (τ)	1776.9	-1	1/2
	electron neutrino (ν_τ)	< 18.2	0	1/2

Table 2.2: Standard Model particles : Quarks

Generation	quarks	mass(MeV/c^2)	charge (e)	spin
First	up (u)	2.2	$+2/3$	1/2
	down (d)	4.7	$-1/3$	1/2
Second	charm (c)	1270	$+2/3$	1/2
	strange (s)	96	$-1/3$	1/2
Third	top (t)	172000	$+2/3$	1/2
	bottom (b)	4180	$-1/3$	1/2

Table 2.3: Standard Model particles : Gauge Bosons

gauge bosons	charge (e)	mass (GeV/c^2)	spin
gluon (g)	0	0	1
photon (γ)	0	0	1
W boson (W$\pm$)	$\pm$ 1	80.4	1
Z boson (Z^0)	0	91.2	1

2.1.1 Gauge Theories

In Standad Model, the interaction of fermions are described by the Dirac Lagrangian:

$$L = \overline{\psi}(i\gamma^\mu\partial_\mu - m)\psi \tag{2.1}$$

where ψ, γ_μ and m are fields representing particles, the gamma matrices and the mass of particles respectively. The fields of the theories transform under gauge symmetry with conserved charges which have been observed in the experiments. To make the Lagrangian gauge invariant, one needs to introduce gauge fields which transform as the adjoint representation of the gauge group.

2.1.2 Quantum Electrodynamics

Electromagnetic interaction is described by a gauge theory with U(1) symmetry group :

$$\psi \to \psi' = e^{-i\theta}\psi \tag{2.2}$$

where θ is a constant phase. To make this global symmetry of U(1) group local, the constant phases θ are made space-time dependent ($\theta \to \theta(x)$) and an additional vector field is introduced in the Lagrangian via covariant derivative.

$$D_\mu \equiv \partial_\mu - ieA_\mu(x) \tag{2.3}$$

whera A_μ and e are spin 1 vector field and charge of the fermion respectively. This A_μ field is a gauge boson field called photon, which mediates the electromagnetic interaction between charged particles. The term $\frac{1}{4}F_{\mu\nu}F^{\mu\nu}$ accounts for the kinetic energy of A_μ, which brings us to the complete lagrangian:

$$L = \overline{\psi(x)}(i\gamma^\mu D_\mu - m)\psi(x) - \frac{1}{4}F_{\mu\nu}F^{\mu\nu} \tag{2.4}$$

2.1.3 Quantum Chromodynamics

Interactions between quarks and gluons are described by quantum chromodynamics (QCD), gauge field theory with SU(3) symmetry group. Quarks which have identical properties otherwise have an added quantum number called color. This "color" comes in three variants, red green and blue and the quarks in terms of color charge are written as $q = (q^R, q^G, q^B)$. This quantum number and its conservation explains the observation of baryons like $\Delta^+(uuu)$ which would otherwise violate Pauli Exclusion Principle. Thus we have quarks in pairs(color-anticolor mesons) and triplets(baryons) and the mediators, gluons appear as eight color-anticolor vector fields. Local gauge invariance requires covariant derivative:

$$D_\mu \equiv \partial_\mu - ig_s\frac{\lambda^i}{2}A^i_\mu \tag{2.5}$$

where A^i_μ are the eight vector fields of gluons, g_s is the strong coupling constant and λ^i are 3×3 Gell-Man matrices. Under strong interactions, quarks have the property of interacting strongly at lower energies or larger distances and weakly at higher energies or shorter distances allowing for perturbative calculations. This is referred to as Asymptotic freedom. Expressing QCD-predicted cross section in terms of a beta function, we can write the strong coupling constant α_s as:

$$\frac{1}{\alpha_s} \propto \log(\frac{Q}{\Lambda}) \tag{2.6}$$

where Q and Λ are momentum transferred and QCD scale(interpreted as boundary between quasi-free quarks and gluons and hadron bound states) respectively. This shows that α_s becomes small as Q^2 becomes large.

2.1.4 Electroweak Theory and Spontaneous Symmetry Breaking

The Glashow-Salam-Weinberg electroweak gauge theory unifies the electromagnetic and the weak forces where both interactions are described by transformations under $SU(2)_L \otimes U(1)_Y$ symmetry group. Weak force describes heavy fermion decay to lighter ones through flavor changing processes. Both left and right-handed particles carry weak hypercharge (Y) which transforms under $U(1)_Y$ while only the left-handed particles carry weak Isospin (T_3) quantum number. Local gauge invariance requires covariant derivative which introduces four gauge boson fields $\vec{W}_\mu$ and B_μ associated with $SU(2)_L$ and $U(1)_Y$ symmetry groups:

$$D_\mu \equiv \partial_\mu - ig\frac{\vec{\tau}}{2}\vec{W}_\mu - ig'\frac{Y}{2}B_\mu \tag{2.7}$$

where g and g' are coupling constants for $SU(2)_L$ and $U1_Y$, $\vec{\tau}$ are $SU(2)_L$ generators and Y is weak hypercharge. Four kinetic energy terms of the four gauge fields are also added. The physical gauge boson fields are written as linear combinations of $\vec{W}_\mu$ and B_μ fields:

$$\begin{aligned} W_\mu^\pm &= \frac{(W_\mu^1 \pm iW_\mu^2)}{\sqrt{2}} \\ Z_\mu &= W_\mu^3 \cos\Theta_W - B_\mu \sin\Theta_W \\ A_\mu &= W_\mu^3 \sin\Theta_W + B_\mu \cos\Theta_W \end{aligned}$$

where Θ_W is the Weinber angle or the weak mixing angle which is used to relate the coupling constants g and g' as :

$$\begin{aligned} \sin\Theta_W &= \frac{g'}{\sqrt{g^2 + g'^2}} \\ \cos\Theta_W &= \frac{g}{\sqrt{g^2 + g'^2}} \end{aligned}$$

Θ_W is a free parameter of SM and $\sin^2\Theta_W$ has been measured to be $\sin^2\Theta_W = 0.22336$. Masses of gauge bosons, mixing angles and electric charge are related by:

$$\begin{aligned} \cos\Theta_W &= \frac{m_W}{m_Z} \\ e = g'\cos\Theta_W &= g\sin\Theta_W \end{aligned}$$

The W and Z mass terms do not come out of $SU(2)_L \otimes U(1)_Y$ as that would violate local gauge invariance but masses are needed for mediators to weakly couple to fermions and act only at short distances. This is possible through Higgs mechanism where scalar fields added to the Lagrangian via spontaneous symmetry breaking give masses to the vector bosons as well as maintain local gauge invariance of the full Lagrangian. Two complex scalar fields forming $SU(2)_L$ doublet ϕ when added generates gauge invariant potential term:

$$V(\phi^\dagger, \phi) = m^2\phi^\dagger\phi + \lambda(\phi^\dagger\phi)^2 \tag{2.8}$$

where m^2 and λ are real constants. When m^2 <0 and λ >0 the potential has a continuous set of minima given by $|\phi_0|^2 = -\mu^2/\lambda = v^2$. Fixing one of these points as the physical vacuum or VEV(Vacuum Expectation Value) breaks the $SU(2)_L \otimes U(1)_Y$ symmetry.

Particle excitations are calculated as fluctuations about the vacuum state and hence the scalar doublet is redefined in terms of the VEV and excitations. Following the Goldstone theorem, each spontaneously broken symmetry of the scalar doublet leads to a massless field in the doublet. The resulting three massless fields, called Goldstone bosons, are absorbed as the longitudinal components of the $W^\pm$ and Z gauge bosons. This generates mass terms for the vector bosons and fermions and gives relations between the $W^\pm$ and Z masses. The remaining real scalar field is the Higgs boson.

2.2 Beyond Standard Model

2.2.1 Limitations of Standard Model

Although the SM is a highly tested theory and makes accurate predictions about particle interactions, there are several phenomena that SM cannot explain like hierarchy problem, grand unification, neutrino mass and dark matter. In this thesis the main topics addressed are listed below :

- Hierarchy Problem
  Standard model does not include gravity and for low energies gravity has little effect. It is very weak compare to electromagnetic forces which can be understood from their ratios:

  $$\frac{F_{gravity}}{F_{em}} = 10^{-40} \tag{2.9}$$

  This apparent weakness of gravity is puzzling. Closely related is the question of fine tuning or why SM Higgs mass is light compared to Planck Scale. For fermions and gauge bosons the radiative corrections are small but not for Higgs since it is a scalar particle and these corrections would be comparable to the Planck scale. The bare mass has to cancel these corrections and while this is possible there is no fundamental understanding of this cancellation. A solution can come from theory of extra dimensions.

- Dark Matter
  Dark matter(DM) is another mystery which the SM fails to solve. There are strong astronomical evidences which suggest the presence of dark matter and it is thought that it makes up around 25% of the energy density of the universe. Weakly Interacting Massive Particles (WIMP) are strong candidates for dark matter and they can be produced in colliders. In R-parity conserving Minimal Supersymmetric Standard Model(MSSM), the lightest supersymmetric particle (LSP) is stable and provides a choice for WIMPs.

2.2.2 Extra Spatial Dimensions

There have been attempts to unify gravity with electromagnetism by adding extra dimensions much before SM. Notably Theodore Kaluza and Oscar Klein proposed an extra spatial dimension for this unification. This extra dimension is also interpreted to be compactified in a cylinder with dimension $\approx 10^{-30} cms$ where the extra spatial dimension is closed and periodic as:

$$x^{new} = x^{new} + 2\pi R \tag{2.10}$$

where R is the radius of the extra dimension. First derivatives of all physical quantities are assumed to vanish with respect to the extra dimension and this independence with respect to the extra dimension explains the invisibility if the 5-dimensional space from the 4-dimensional subspace.

Theories of compactified extra dimensions have been implemented into string theories like the 11-dimensional M theory but string theories make predictions for observable phenomena in energies unattainable by current accelerators. But theories inspired by string theory which predict effects in TeV scale are also present like the one proposed by Arkani-Hamed, Dimopolous and Dvali.

2.2.2.1 Large Extra Dimensions in ADD model

ADD model [1] postulates the presence of n compactified extra dimensions in addition to the 3+1 spacetime dimensions. Only gravity can propagate in all the dimensions while SM particles are restricted only to the standard 4 dimensions. Gravity becomes strong at smaller distances and weaker at larger distances. The name Large appears since certain model parameters allow for extra dimension radius to be of the order of μm.

Following ADD model paper, we assume n and M_D to be number of extra dimensions of radius R and fundamental scale of gravity in the 4+n dimensional theory. Using Gauss'

Law, the gravitational potential between two test masses m and M is given by:

$$V(r) = \frac{mM}{M_D^{n+2} R^n} \frac{1}{r} \qquad when \qquad r \gg R$$
$$V(r) = \frac{mM}{M_D^{n+2}} \frac{1}{r^{n+1}} \qquad when \qquad r \ll R$$

where r is the distance between the masses. This gives the effective Planck scale to be:

$$M_{Pl}^2 \approx M_D^{n+2} R^n \tag{2.11}$$

If this M_D is of the same order as the electroweak scale no fine tuning is required and the weakness of gravity is explained. This solves two problems of SM. The large Planck scale value can now be attributed to large size of R and the number of extra dimensions. We can derive an expression for R:

$$R = 10^{\frac{30}{n}-17} cm \times (\frac{1TeV}{m_{EW}})^{1+\frac{2}{n}} \tag{2.12}$$

For M_D=1TeV and n=3, R is around 10^{-9}m.

2.2.2.2 ADD model collider phenomenology

Keeping M_D at the TeV scale, for n=1, R becomes of the order of 10^{10}m leading to effects at the scale of solar system in the absence of which n=1 is excluded. For n=2, R is of the order of 10^{-5}m which could be probed in LHC but recent results excluded it too. Thus we consider n>2 where the scale of extra dimensions is $< 10^{-10}$m, a distance where gravity has not been probed. [2] gives an outline of the effective theory for ADD model where gravitons are included in QED and QCD lagrangians. In this theory a spin-2 graviton can propagate freely in 4+n dimensions and mediates the gravitational interaction. 4-dimensional projection of massless gravitons in the compactified extra dimensions leads to Kaluza-Klein towers of massive graviton modes. The massive graviton states are solutions to free field equations of particles in extra dimensions. For example the 5-dimensional Klein-Gordon equation for a massless particle with spin-0 is:

$$\partial_A \partial^A \Phi(x_A) = (\partial_\mu \partial^\mu - \partial^2)\Phi(x_\mu, x_5) = 0 \tag{2.13}$$

where A represents the standard 4 spacetime dimensions plus x_5, the added space-like extra dimension. Adding the periodic boundary condition $x_5 = x_5 + 2\pi R$ and Fourier expanding the fields gives:

$$\Phi(x_\mu, x_5) = \sum_{\alpha=-\infty}^{\infty} \phi_\alpha(x_\mu) e^{\frac{i\alpha x_5}{R}} \tag{2.14}$$

which yields for each of the fields ϕ_α :

$$\partial_\mu \partial^\mu \phi_\alpha = \frac{\alpha^2}{R^2} \phi_\alpha \tag{2.15}$$

This now becomes an infinite tower of 4-dimensional fields, where mass term $m_\alpha = \frac{\alpha^2}{R^2}$ represents discrete mass modes. Similar principles can be applied to spin-2 gravitons. The mass splitting between any two mass modes m_α and $m_{\alpha+1}$ depends on the size of the compactified extra dimensions and is given by

$$\Delta m \approx \frac{1}{R} = M_D (\frac{M_D}{M_{Pl}})^{\frac{2}{n}} \approx (\frac{M_D}{TeV})^{\frac{n+2}{2}} 10^{\frac{12n-31}{n}} eV \tag{2.16}$$

For $M_D = 1$TeV this would yield mass splittings of 46.4eV for n=3, 0.6MeV for n=5 and 37.2MeV for n=7. The gravitons couple to $T^{\mu\nu}$, the energy momentum tensor of the SM fields.

Graviton is stable in collider time scales since the decay is suppressed by a factor $\propto \frac{M_{Pl}^2}{m_\alpha^3}$ where m_α is mass of graviton mode. Gravitons would appear as stable non-interacting particles and would give rise to missing momentum in events where it is produced along with SM particles. It can be produced in processes like:

$$gg \to qG$$
$$q\bar{q} \to gG$$
$$qg \to qG$$
$$q\bar{q} \to \gamma G$$

The last process can give rise to a single high p_T photon in the final state along with a large missing transverse momentum (p_T^{miss}).

2.2.2.3 Status of Large Extra Dimension Searches

There have been searches based on ADD model in final states with energetic photon or jet with large missing momentum in $p-\bar{p}$ collisions in CDF [3] and D0 [4] experiments at Tevatron as well as $e^+ - e^-$ collision events in LEP [5] like L3,OPAL,ALEPH and DELPHI. At LHC, in both CMS and ATLAS, graviton searches fall in three general categories: mono-X searches, virtual graviton exchange search and black hole searches. Since the

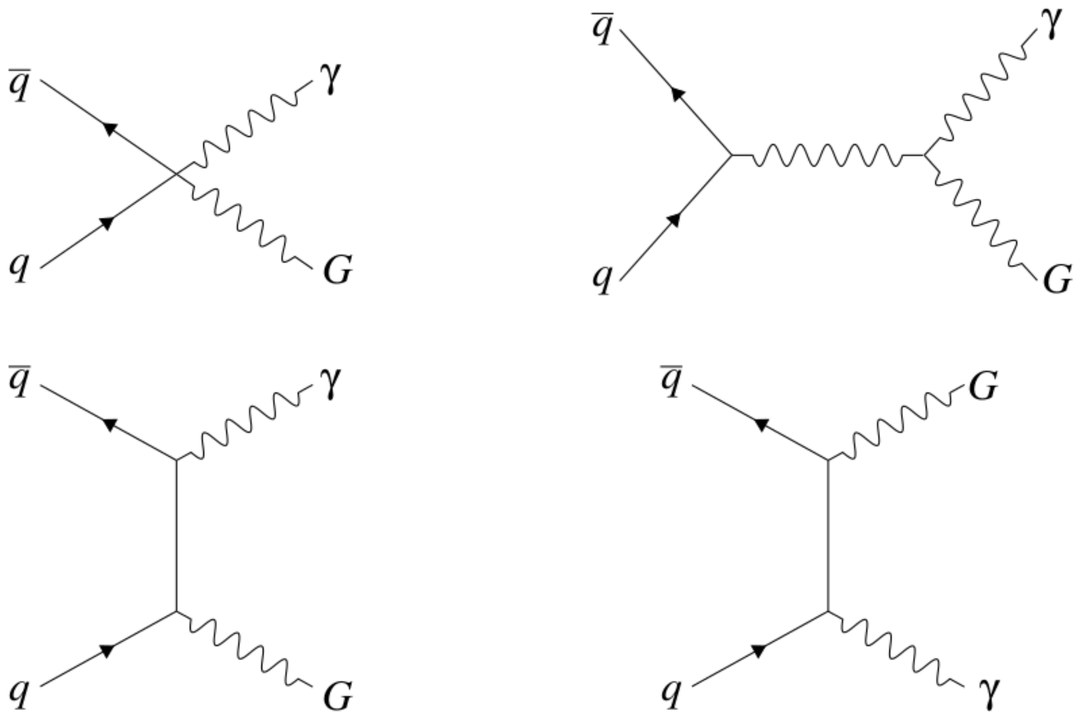

Figure 2.1: Feynman diagrams for graviton production through the process q$\bar{q} \rightarrow \gamma G$

thesis concerns mono-X searches only that is discussed below. In mono-X searches final states where X is jet(q/g) have a higher cross-section and hence have stronger limits due to the higher sensitivity. ATLAS sets upper limits at M_D =7.7 TeV for n=2 and 4.8TeV for n=6 with limits for intermediate n's being between these values [6]. CMS sets upper limits at 9.9 TeV for n=2 and 5.3 TeV at n=6 [7] .

2.2.3 Dark Matter

2.2.3.1 Observational Evidence

There are many astronomical observations which support the notion that ≈ 25% of the mass-energy of the universe is made up of Dark Matter (DM) [8]. Observations by Oort and Zwicky in Milky Way and Coma clusters pointed to the necessity of additional mass in galaxies than what was observed. This was further reinforced by the studies of Vera Rubin and collaborators [9] where they studied the rotational curve of galaxies. If it is assumed that the orbits of stars within a galaxy can mimic rotations of planets around the sun, from Newtonian gravity one would expect the velocity to fall off as $v(r) \propto \frac{1}{r^{0.5}}$, but it is observed to become flat. This is shown in figure 2.2 All these indicate presence of more matter than what is observable through electromagnetic radiation.

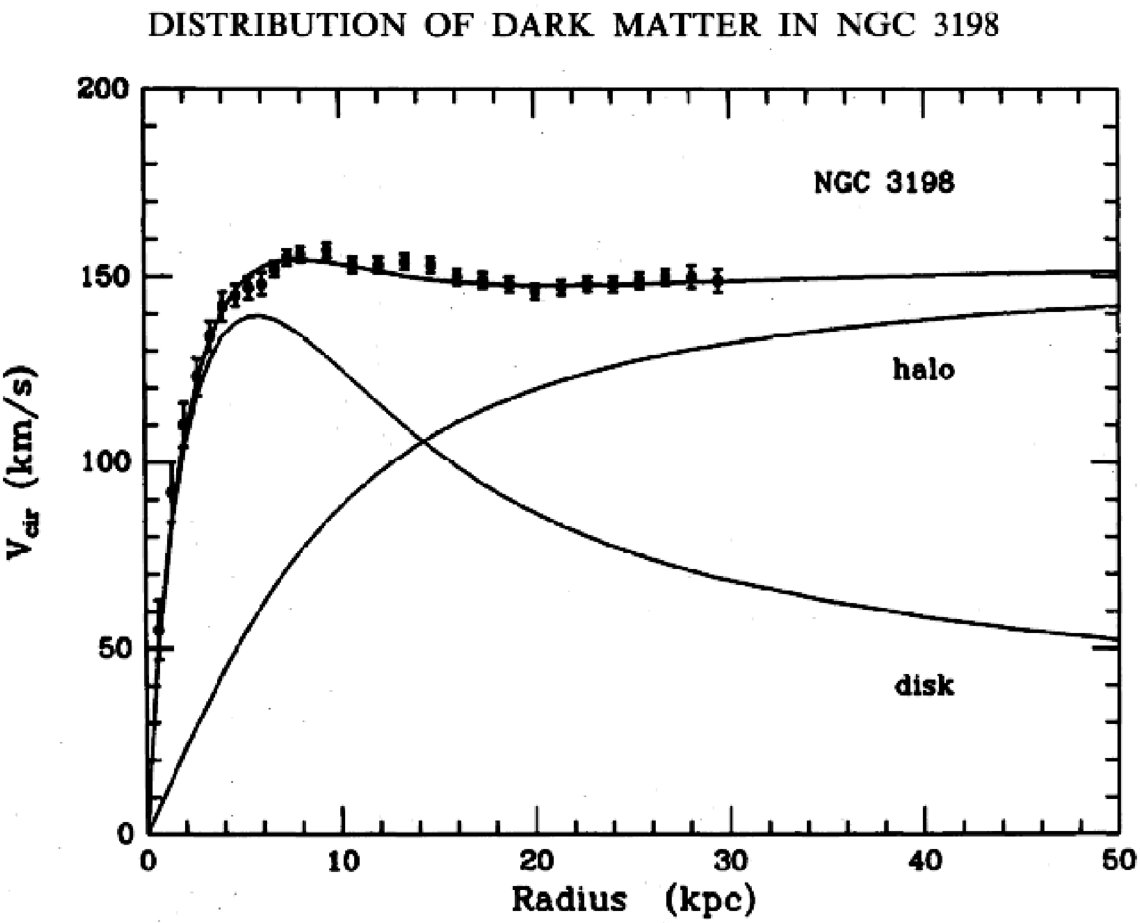

Figure 2.2: Rotational velocity for the NGC 6503 galaxy plotted as a function of radius from the galactic center. The dashed, dotted and dot-dashed lines represent the expected contributions from three components: the luminous disk, the gas content of the galaxy and the dark matter halo respectively. The full line is the combination of these three, which agrees very well with the observed data [10].

Weak Lensing measurements have also given indications of DM. Light from background galaxies is bent by gravitational lensing of clusters in front of it which can be measured from the amount of deflection. The most compelling evidence of DM comes from gravitational lensing from bullet clusters [11]. Bullet cluster formation took place when two clusters collided and the X-ray from one of them looked like a bullet. The X-ray spectrum contains majority of the baryonic component. While X-ray emitting material was found mostly concentrated in the central part of the cluster, the gravitational lensing pointed to matter densities away from the collision vertex of the two clusters. Also it is as if the visible matter from the two clusters was impacted heavily in the collision but the dark matter halo passed through silently without interactions.

2.2.3.2 Weakly Interacting Massive Particle (WIMP)

Structure formation in the universe requires DM candidate to be cold or non-relativistic when galaxy formations began. Also the candidate has to be stable so that it does not decay in cosological time scales along with interacting weakly with radiation. WIMPS are non-baryonic, non-relativistic stable fermions with masses in the rage of GeV-TeV .The interaction cross section of WIMPs is of the order of weak interaction to arrive at the correct relic density. This is known as WIMP miracle.

2.2.3.3 Dark Matter Experimental Searches

DM searches are of three types depending on which mode of DM interaction with matter is probed. Direct detection experiments (DAMA/LIBRA/XENON1T) search for evidence of χ-nucleon scattering in detectors which are usually buried deep underground to keep background interactions to a minimum. Indirect detection experiments (Fermi-LAT,AMS) look for excess SM particles produced from $\chi\bar{\chi}$ annihilations.
In colliders WIMPs can be created in p-p collisions giving rise to $\chi\bar{\chi}$ pairs which will not be detected since they interact weakly. When they are produced in association with a photon as $q\bar{q} \to \chi\bar{\chi}\gamma$, where the photon is radiated from incoming quarks, they may appear as an excess of $\gamma + p_T^{miss}$ events, where the SM expectation is from $Z(\nu\bar{\nu})\gamma$ events. The γ could have been jet or Z or W which would cumulatively be called mono-X searches. In fact mono-jet having higher cross-section has higher sensitivity but in this thesis we will always talk about mono-photon final state. The DM searches are interpreted in terms of the simplified models. Early experiments in Tevatron and LHC Run-1 used effective field theory to model dark matter signal where coupling structure and the effective scale were the only parameters of interest. This assumed that the mediators were very heavy and also for low effective scales EFT broke down. This also posed a problem when comparing results from direct detection experiments. For the Run-2 the recommendation

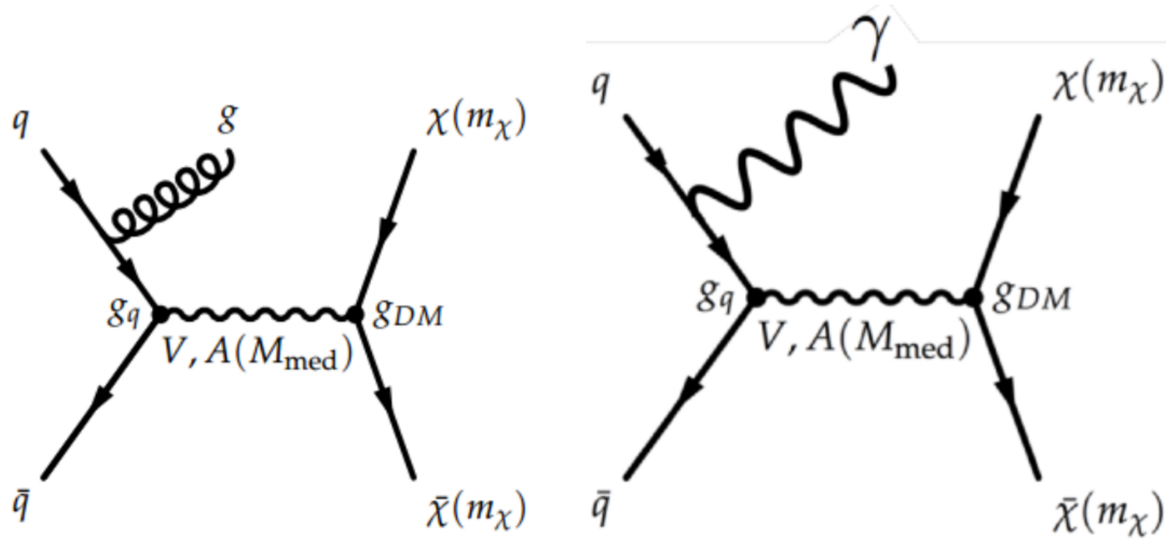

Figure 2.3: Feynman diagram showing pair production of dark matter in association with a gluon according to simplified model with parameters described in the text.

of LHC Dark matter forum (LHCDM) has been the use of benchmark simplified models where a physical mediator comes in the place of effective scale. Here the model has four parameters: mass of fermionic dark matter M_χ, mass of mediator M_{med}, coupling to the quarks g_q and g_{DM} the coupling to dark matter in s-channel(see figure 2.3). For t-channel which has not been considered in the thesis, there would be three parameters. The mediators can be Vector, Axial-Vector, Scalar and Pseudoscalar. In this thesis only vector and axial-vector mediators are considered since sensitivity is not there yet in monophoton channel for the other mediators. The g_q is set to be 0.25 for all flavors and g_{DM} is set to be 1. Minimal width assumption is made that mediator couples to SM and DM particles and to no added particles. Presence of extra particles would increase the width leading to decrease the sensitivity. Coupling to leptons is set to be 0.

2.2.3.4 Current Status of Dark Matter Searches.

Summary plots show the bounds on dark matter with 2016 data. From both figure 2.4 and figure 2.3 the mono-X searches give a best limit on DM mass at about 1.8TeV with mono-jet being the most sensitive channel. Also collider results can be cast to compare with direct detection experiments shown in figure 2.6 and 2.7. For the spin dependent case, the colliders set the strongest bounds whereas for spin independent case the direct detection experiments are much more powerful. However the power of collider bounds come here when the dark matter masses are low in all cases.

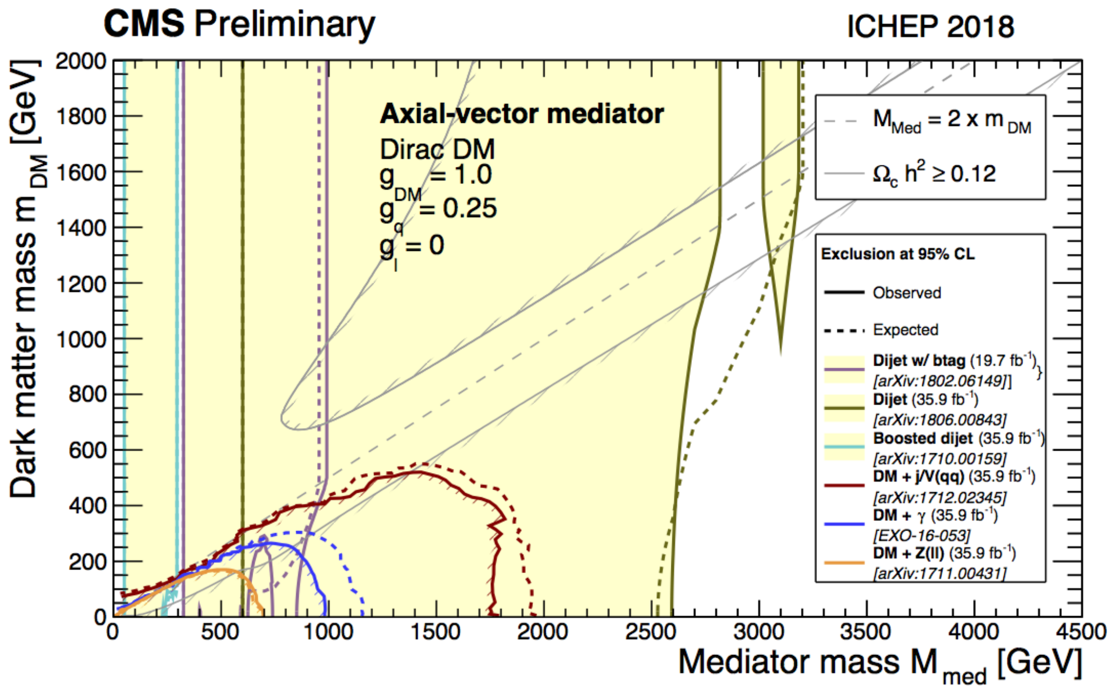

Figure 2.4: Exclusion plot in DM mass-mediator mass plane with contributions from mono-X as well as dijet and other resonance searches for axial vector mediator.

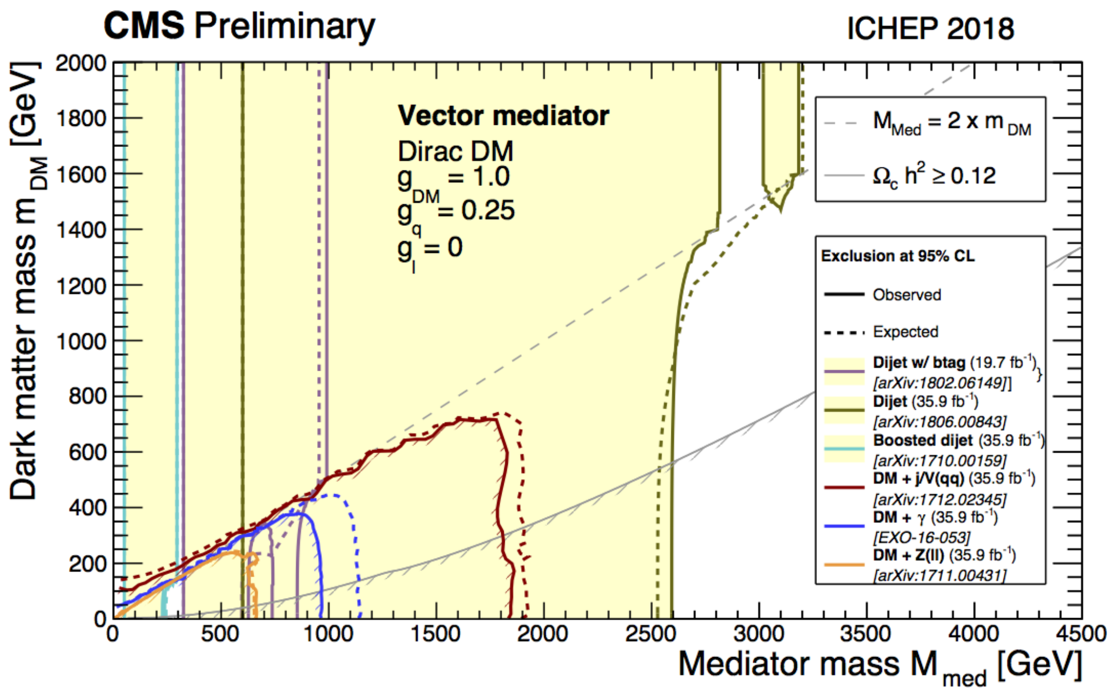

Figure 2.5: Exclusion plot in DM mass-mediator mass plane with contributions from mono-X as well as dijet and other resonance searches for vector mediator.

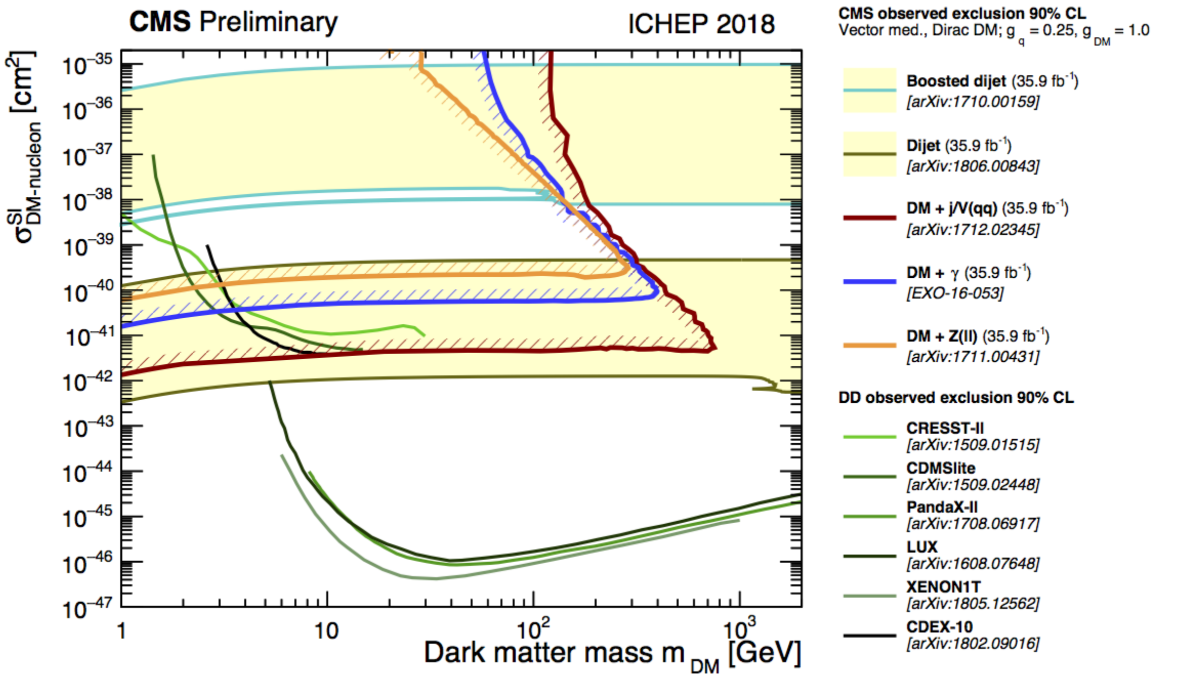

Figure 2.6: Summary plot comparing collider bounds with direct detection bounds for spin-independent(SI) case in DM mass-SI cross section plane.

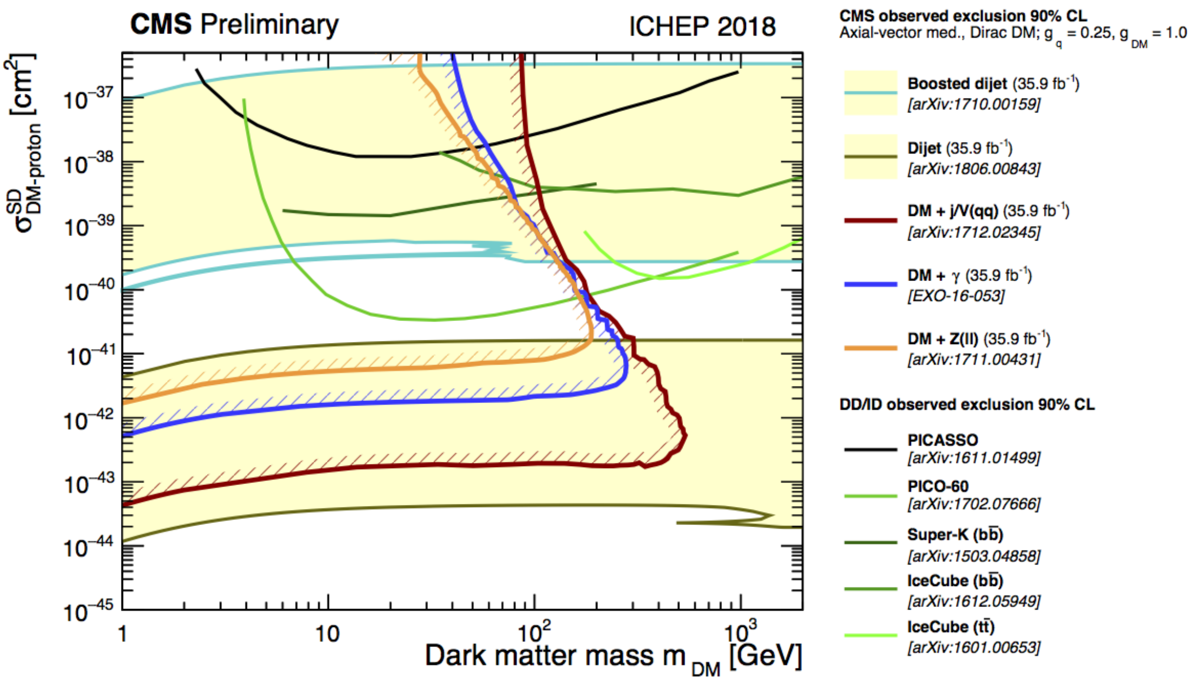

Figure 2.7: Summary plot comparing collider bounds with direct detection bounds for spin-dependent(SD) case in DM mass-SD cross section plane.

Chapter 3

The Experimental Apparatus

3.1 The Large Hadron Collider

The Large Hadron Collider (LHC) is a proton-proton collider designed to search for the Higgs boson and probe new physics at multi TeV scale. It is installed in an underground tunnel of circumference 26.7 Km underneath France and Switzerland. The tunnel was originally built for a previous collider called Large Electron-Positron machine(LEP). Figure 3.1 shows the LHC with the locations of four detectors, CMS, ATLAS, ALICE and LHCb. The main goal of LHC is to search for new physics beyond SM using colliding protons at centre of mass energies upto 14TeV. The LHC has been designed to produce collisions at an interval of 25ns with a design peak luminosity of $L = 10^{34}cm^2s^{-1}$ which would be around a billion interactions every second at CMS and ATLAS the two multipurpose detectors built to collect data from collisions at high luminosities. For the time period during which data was collected for analysis presented in this thesis, collisions occured at $\sqrt{s} = 13TeV$ centre of mass energy.
During its peak performance LHC has about $5{\times}10^{14}$ protons in each beam. The protons are obtained from Hydrogen gas which is ionised with an electric field to separate protons from the electrons. These protons further go through linear accelerator (LINAC2), proton synchrotron booster (PSB), proton synchrotron (PS and super proton synchrotron (SPS). This chain accelerates protons to LHC design energies. The particles are at first accelerated to 750keV and a radio frequency quadrupole focuses them into a segmented beam. Then the LINAC2 accelerates them to 50MeV in microseconds before passing on to PSB which accelerates them to 1.4 GeV in 530ns. The protons are then injected into PS where they are accelerated to 25GeV and divided the protons into bunches with uniform spacing between them. 81 bunch packets are formed with 25ns or 8m spacing between them at design performance. Finally the protons are sent to LHC after being accelerated to 430GeV in 4.3s. These proton bunches are put in appropriate places along the beam

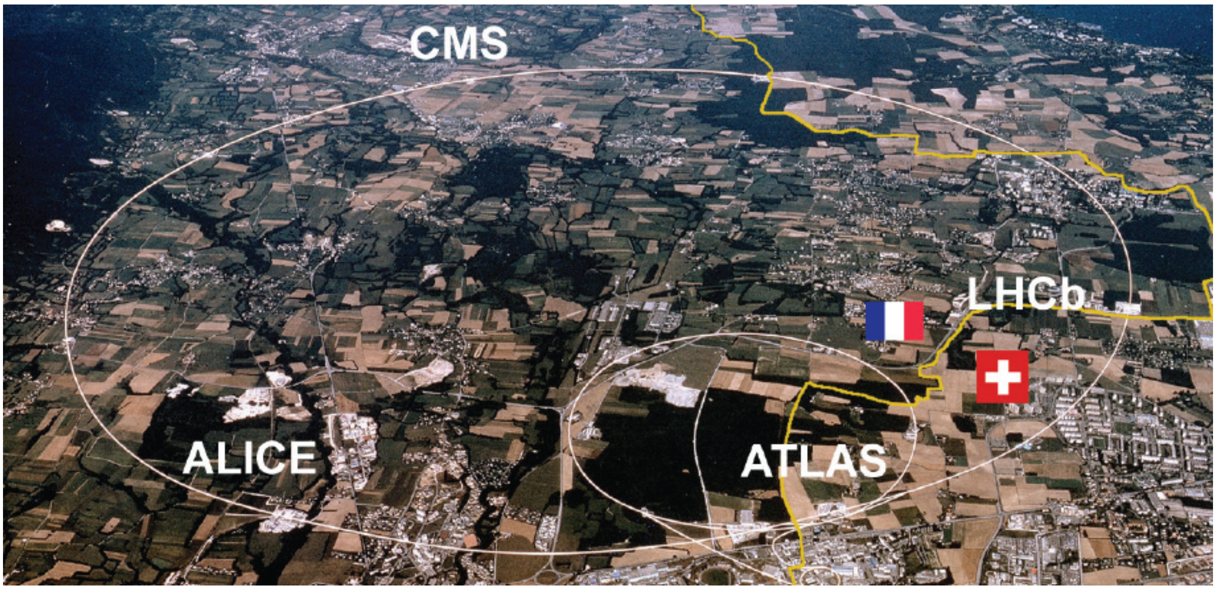

Figure 3.1: An aerial view of the LHC showing four detectors.

line. The longest part of the injection chain is injecting the bunches and then ramping up to high energy which takes about 45 minutes.

3.2 Compact Muon Solenoid

The Compact Muon Solenoid (CMS) detector [12] is one of the two multipurpose detectors located at LHC. It is located 100m below the ground near the Cessy in France. CMS had the following requirements to match LHC physics program goals:

- Very good Muon identification as well as resolution over a broad range of momenta and angle along with good dimuon mass resolution of the order of 1% at 100GeV. The charge of the muon also has to be determined exactly for muons with p_T <1 TeV.
- Very good reconstruction efficiency as well as momentum resolution for charged particles in the inner tracker system. Pixel detectors close to the interaction region to ensure efficient triggering and offline tagging of b-jets and τ's.
- Excellent electromagnetic calorimeter(ECAL) resolution, di-photon and electron resolution of the order of 1% at 100GeV, a wide geometric coverage region, ability to reject π^0 well along with efficient photon and lepton isolation at higher luminosities.
- Good dijet mass and missing transverse energy which requires hadron calorimeters(HCAL) with hermetic coverage and fine lateral segmentation.

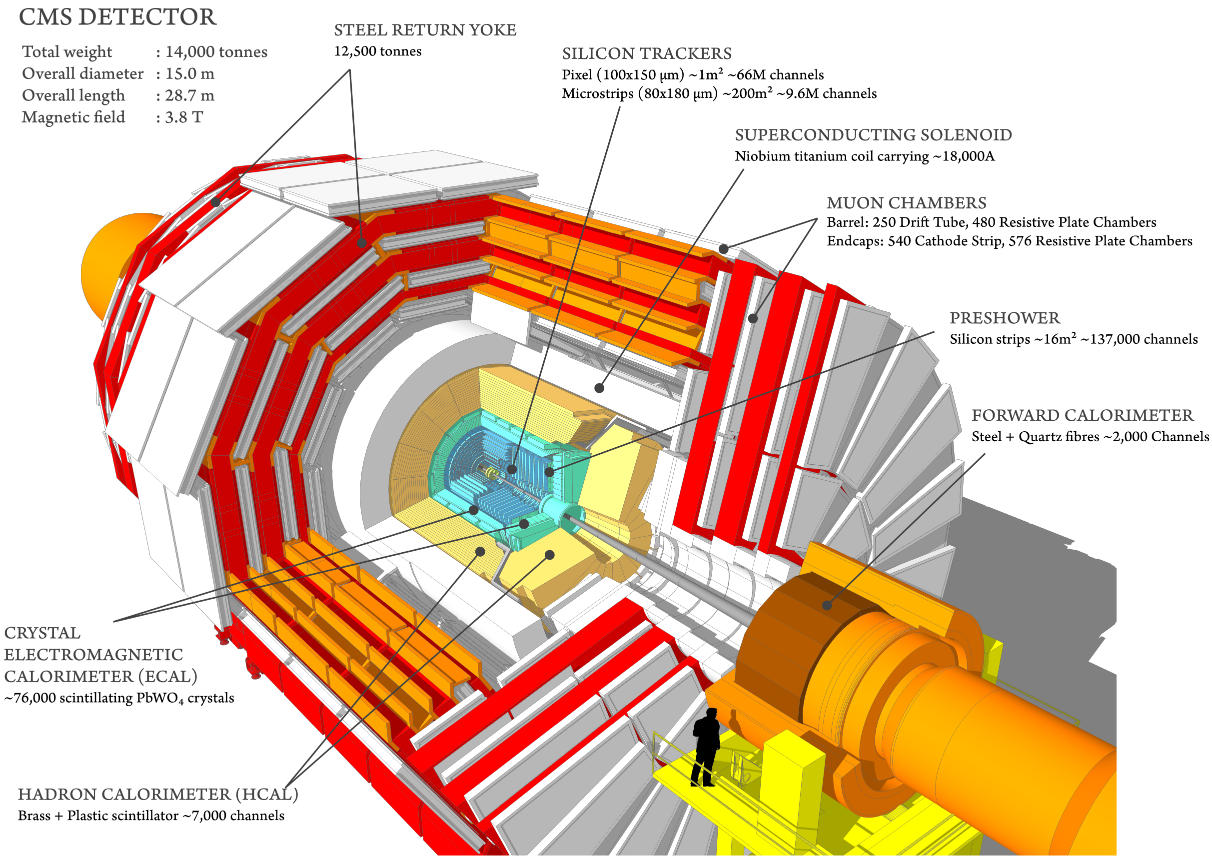

Figure 3.2: Schematic diagram of CMS showing the major components. [13]

CMS was designed to meet all these requirements. The features that distinguish CMS are the solenoid producing a high axial magnetic field, an inner tracking system fully based on silicon and a homogeneous ECAL made of scintillating crystals.

The origin of the coordinate system of CMS is the nominal collision point with the Y-axis pointing upwards vertically and the X-axis pointing radially inwards towards the center of LHC while the Z-axis points to the direction of the beam. The azimuthal angle ϕ is measured in the X-Y plane and begins form the X-axis. The radial distance in this plane is denoted by r while the ploar angle θ is measured from the Z-axis. With this the pseudorapidity is defined as $\eta = -\ln\tan(\theta/2)$. p_T and E_T which are the transverse components of momentum and energy to the beam direction are computed from the X and Y components while the energy imbalance measured in the transverse plane is denoted by E_T^{miss}.

CMS has a diameter of 14.6m and is 21.6m long with a total weight of 12500 tonnes. The components of the detector from inside to outside are the tracker, the ECAL, the HCAL, the solenoidal magnet, muon systems. Figure 3.2 shows the CMS detector and how the subdetectors are placed relative to each other.

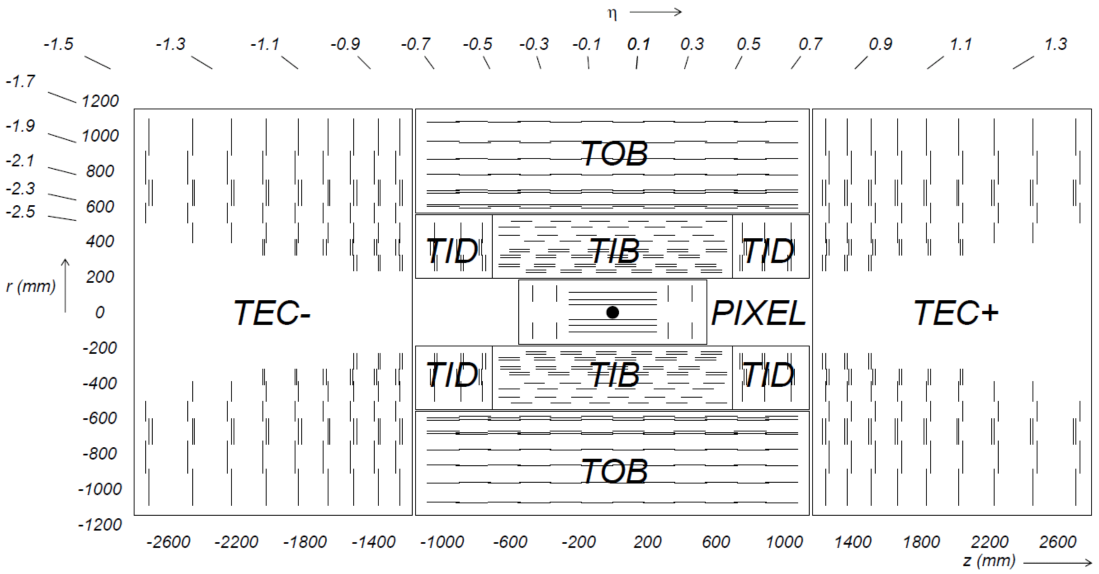

Figure 3.3: Schematic cross-section of the CMS tracker. Each single line represents a detector module while double lines represent back-to-back modules that deliver stereo hits.

3.2.1 Tracking System

Figure 3.3 shows the tracker system. The tracking system is designed to provide efficient and precise measurements of charged particle trajectories coming out of collisions along with precise secondary vertex reconstruction. It consists of silicon p-n junctions and when charged particles cross this junction they generate electron-hole pairs which are collected by the readout electronics. The tracker surrounds the interaction point and has a diameter of 2.5m and a length of 5.8m. The density of tracks decreases away from the interaction point and more procise position measurement and charged particle separation is required near the interaction point. Hence, the tracker system is composed of two parts: a pixel detector providing more precise position information consisting of three barrel layers at radii between 4.4cm and 10.2 cm and a silicon strip tracker composed of 10 barrel layers extending outwards to a radius of 1.1m. Both the systems have endcaps which consist of two discs for the pixel detector and 3+9 discs for silicon strip trackers on either side of the barrel. This extends the acceptance of the tracker upto a pseudorapidity of $|\eta| < 2.5$. The CMS tracker is the largest silicon tracker ever built with about $200m^2$ of active silicon.

3.2.1.1 Pixel Detector

The pixel detector is designed in such a way so as to get highly precise 3D measurements close to the interaction vertex. Its pseudorapidity coverage range is $-2.5 < \eta < 2.5$ which matches the acceptance of the strip tracker. There are three barrel layers(BPix) which are 53 cm long located at mean radii of 4.4, 7.3 and 10.2 cm and two endcap discs(FPix) placed on either side of the interaction point at $|z| = 34.5$ and $|z| = 46.5$ cm, ranging from 6cm to 15cms in radius. BPix contains 48 million pixels covering area of $0.78 m^2$ while FPix contains 18 million pixels covering area of 0.28 m^2. Pixel detector provides three precise points over almost the full η range for each charged particle trajectory. The pixel sizes of 100×150 μm^2 provide a spatial resolution in the range of 15-20μm which is optimum near the interaction vertex with high charged particle flux.

3.2.1.2 Silicon Strip Tracker

The silicon strip tracker occupies the radial region between 20cm and 116cm beyond the pixel detector. Since the particle flux density reduces strips can be used instead of pixels. It has three subsystems. Tracker Inner Barrel and Discs (TIB/TID) are composed of four barrel layers supplemented by three discs on either side extending upto radius 55cm. Using 320μm thick silicon micro-strips sensors where the sensors are parallel to the beam axis in the barrel and radial on the discs, the TIB/TID provides upto four r-ϕ measurements along the trajectory. In TIB, the pitch of the strip is 80μm for layers 1 and 2 and 120μm for layers 3 and 4 which leads to single point resolution of 23μm and 35μm respectively. In TID the mean pitch varies between 100μm and 141μm.

The Tracker Outer Barrel (TOB) surrounds the TIB/TID. With an outer radius of 116cm, it consists of 6 barrel layers of 500μm thick micro-strip sensors with 183μm strip pitches in the first four layers and 122μm in layers 5 and 6. Thus it provides another six r-ϕ measurements with single point resolution of 53μm and 35μm respectively. In Z, the TOB extends between $\pm$118cm.

TEC+ and TEC- (signs indicate the locations along the Z axis) which are the Tracker Endcaps cover the Z range between 124cm $< |Z| <$ 282cm and 22.5cm $< r <$ 113.5cm. TECs have 9 discs each, with upto 7 rings of silicon micro-strip detectors (inner 4 rings wit 320μm thickness and rings 5-7 with 500μm thickness) with radial strips of average pitch between 97μm to 184μm. In total the TEC can make upto 9 ϕ measurements on a passing charged particle. A second micro-strip detector module is mounted back-to-back with a stereo angle of 100 milli-radian to get a measurement of a second coordinate(r in discs and Z in the barrel) for the first two layers of TIB and TOB, the first two rings of TOB and rings 1,2 and 5 of the TEC. This helps in achieving a single point resolution of 230μm and 530μm in TIB and TOB respectively while it varies with pitch in TID and TEC. This layout of the tracker ensures at least 9 hits in the silicon strip tracker in the full eta range $|\eta| < 2.4$ with at least 4 hits providing 2-D information for the track. The silicon strip tracker has in total 9.3 million strips and 198m^2 of active silicon area.

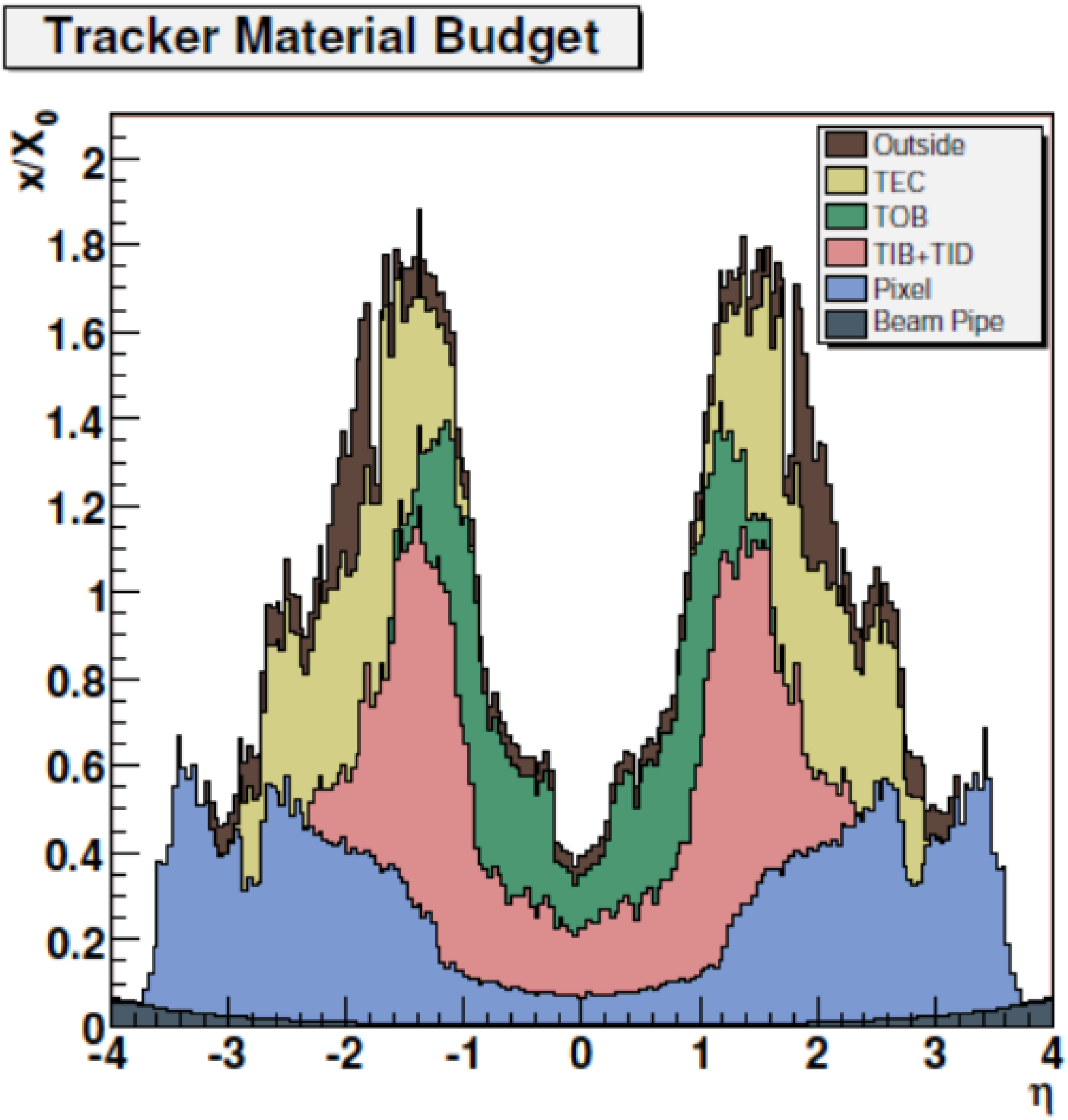

Figure 3.4: Tracker material budget in radiation length units for different sub-detectors. [14]

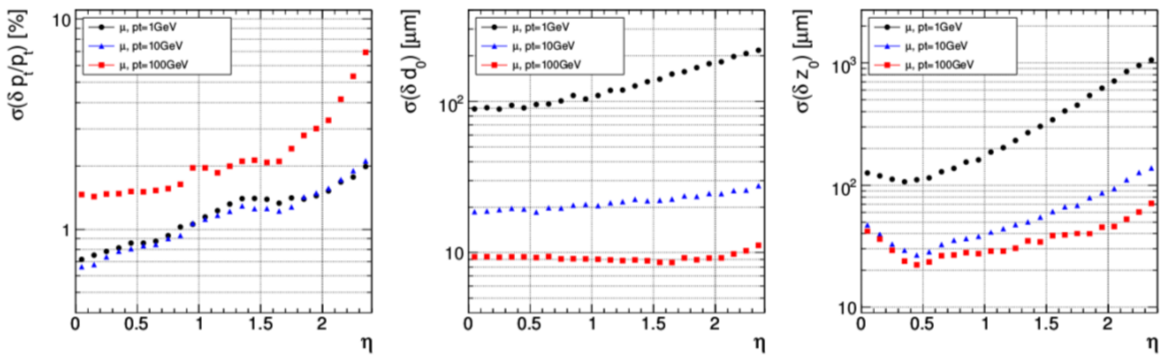

Figure 3.5: Resolution of track parameters obtained for muons of various momenta (1,10,100 GeV): the ransverse momentum (left), the transverse impact parameter (middle) and the longitudinal impact parameter (right).

3.2.1.3 Performance

The total amount of material present before the calorimeter affects the calorimeter system performance. Fig 3.4 shows the material budget of the tracking system broken down to its various components as a function of η. The p_T resolution of the system is shown in fig 3.5 and it shows tat the resolution is around 1-2% for ∼100GeV high p_T tracks. Fig 3.5 also shows the transverse and longitudinal impact parameter resolutions.

3.2.2 Electromagnetic Calorimeter

The CMS Electromagnetic Calorimeter (ECAL) [15] measures the energy of electrons and photons. High energy electrons and photons lose their energies in EM sowers primarily through radiative processes namely pair production for photons and bremstrahlung for electrons. The shower particles further produce scintillation light in the crystals which are collected by photo-detectors which finally give a measure of the energy deposited by the particle.

It is a homogeneous calorimeter made of lead tungstate (PbWO 4) crystals. There are 61200 crystals in the central barrel part while 7324 crystals make the two endcaps on either side. A preshower detector is placed in front of both the endcaps. Avalanche photodiodes (APD) is used as photo-detectors in the barrel and vacuum phototriodes (VPT) is used in the endcaps. The high density of 8.28g/cm^3, short radiation length of 0.89cm and small Moliere radius of 2.2cm ofthe PbWO4 crystals make them an appropriate choice for operation at the LHC resulting in a fine granular and a compact calorimeter. The crystals emit 80% of the light from interactions within 25 ns which makes them fast and are also radiation hard. The blue-green scintillation light emitted by the crystals have a broad

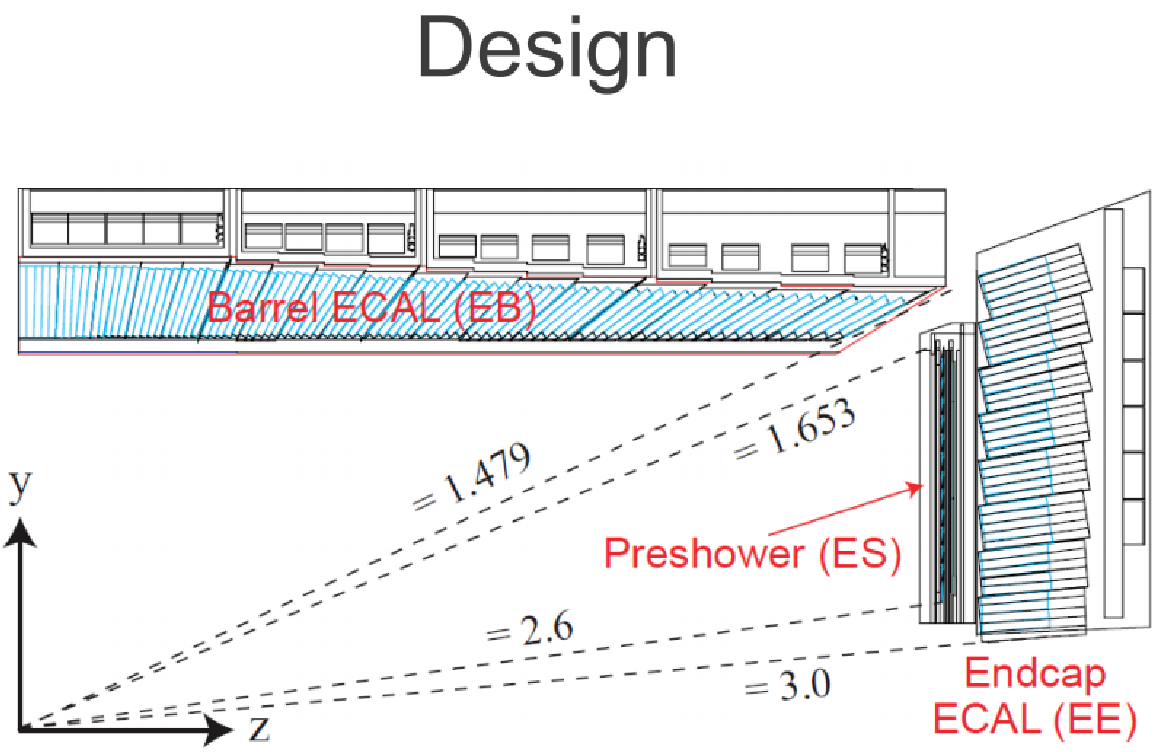

Figure 3.6: η coverage of ECAL

maximum at 420-430 nm. The barrel part called EB covers the pseudorapidity range of $|\eta| < 1.479$. The granularity in the barrel is 360 in ϕ and 85 in either side of η which results in total 61200 crystals. The crystals have a tapered shape and are slightly off-center pointing at an angle of 3 degrees with respect to the nominal interaction point. This is done in order to avoid particle trajectories to line up with cracks. The crystals correspond to a granularity of approximately 0.0174×0.0174 in the $\eta - \phi$ space which corresponds to 2.2×2.2cm^2 at the front face of crystal, and 2.6×2.6cm^2 at the rear face. The crystals have a length of 23cm which corresponds to 25.8 radiation lengths(X_0). The endcaps (EE) provides coverage in the range $1.479 < |\eta| < 3.0$. The interaction point and the endcap are separated by 315.4 cm which takes into account the estimated shift toward the interaction point by 1.6 cm when the 4T magnetic field is applied. In the endcap crystals are grouped into units of 55 crystals (called supercrystals (SC)). Each of the endcaps is divided into 2 halves called Dees. Each of them holds 3662 crystals. The crystals are arranged in a rectangular x y grid with the crystals focusing at a point 1300 mm beyond the interaction point which gives off-pointing angles ranging from 2 to 8 degrees. The rear face cross-section of the crystals is 3.0×3.0cm^2 ,front face is 28.62×28.62mm^2 with a length of 220mm (24.7X_0). The eta layout is shown in figure 3.6. The barrel and endcap are shown in figures 3.7 and 3.8 respectively.

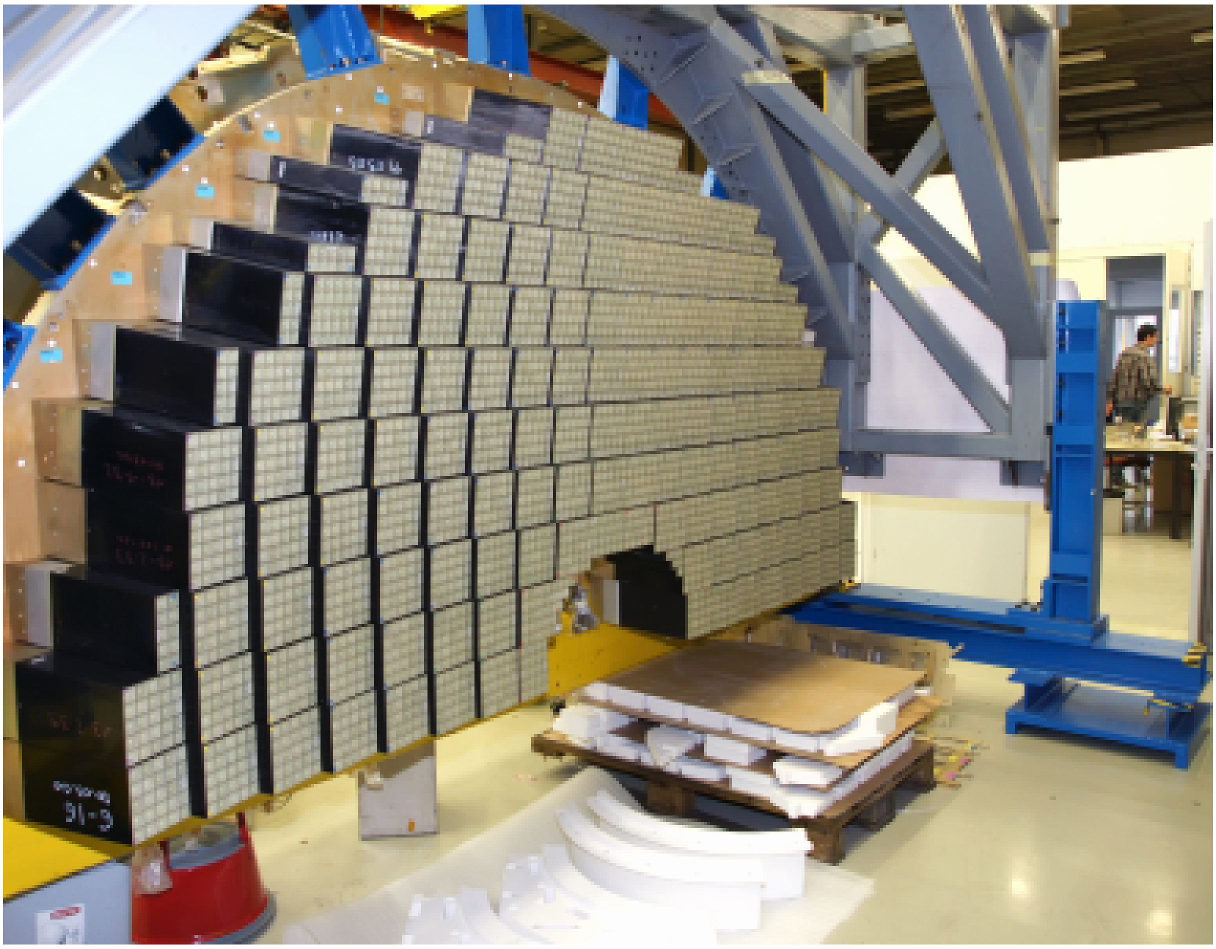

Figure 3.7: Endcap with crystals

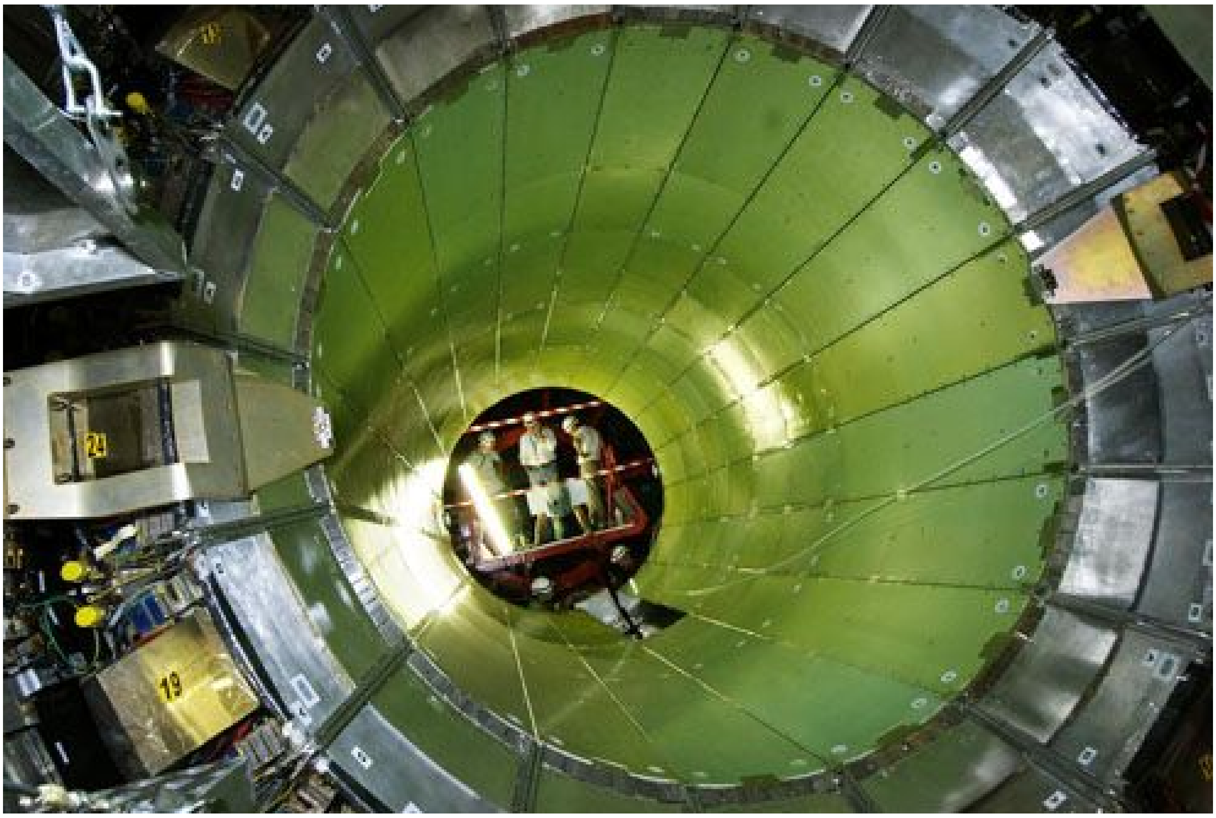

Figure 3.8: ECAL barrel with crystals mounted

The ECAL energy resolution is parametrized as a function of energy as:

$$\frac{\sigma(E)}{E} = \frac{S}{\sqrt{E}} \otimes \frac{N}{E} \otimes C \tag{3.1}$$

where S is the intrinsic stochastic term, N is the noise term and C is the constant term. S,N and C are measured to be $\sim 2.8\%$ (photostatistics), $\sim 12\%$ (electronic noise) and $\sim 0.3\%$ (leakage and miscalibration) from test beams. Fig 3.9 shows the ECAL barrel resolution derived from electron test beams. The resolution is $\sim 1\%$ for energies >20GeV.

3.2.3 Hadron Calorimeter

The Hadronic Calorimeter (HCAL) [17] is a sampling calorimeter which is composed of alter- nating layers of brass or steel absorber and plastic scintillator. It measures energies of hadronic jets and also missing transverse energy due to neutrinos or other new physics sources. Hadrons interact with the nuclei in the dense absorber which produces secondary particles which also in turn interact with the absorber resulting in a cascade of particles known as a hadronic shower. This shower then produces scintillation light and this signals

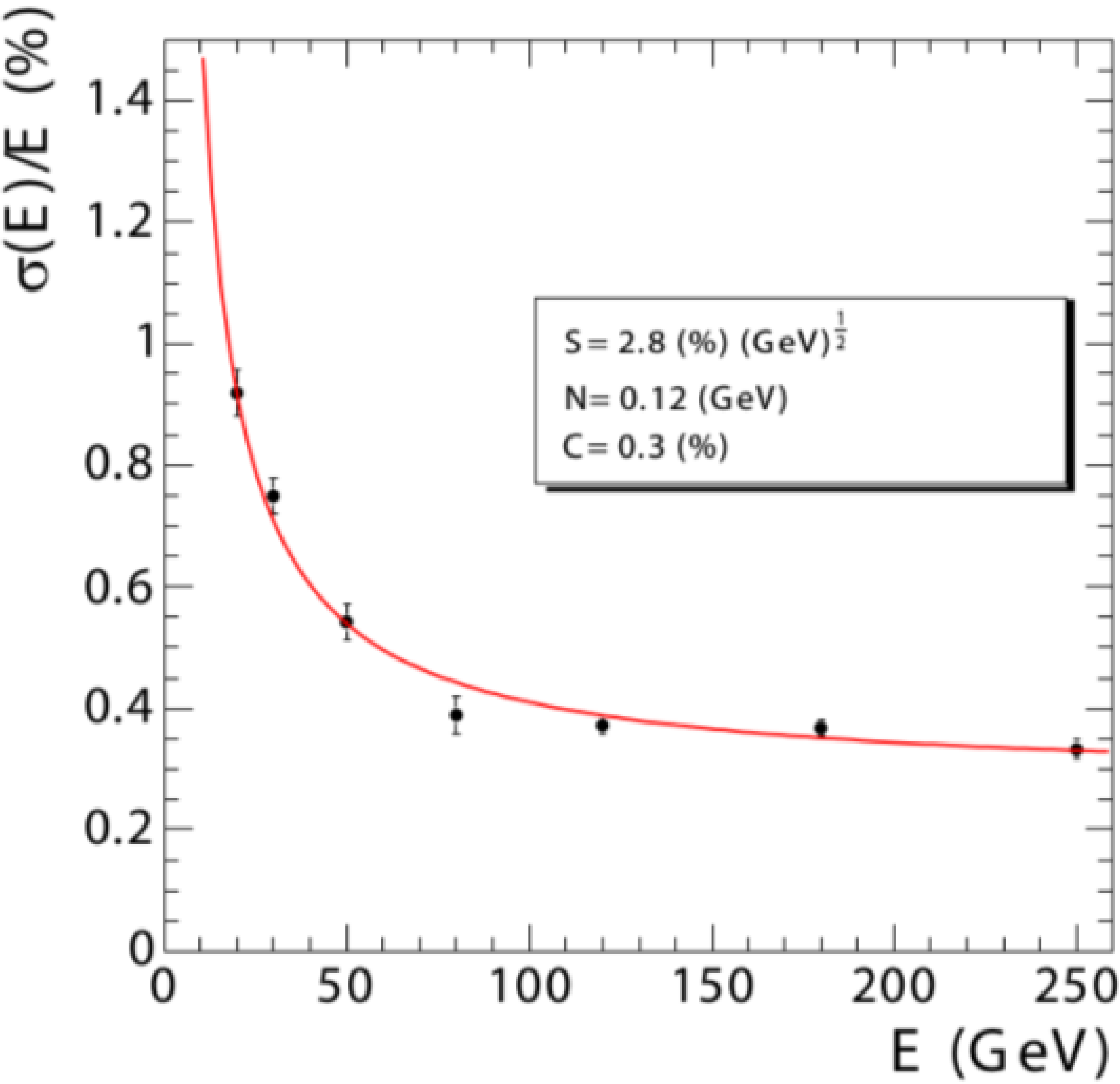

Figure 3.9: ECAL energy resolution as a function of energy. [16]

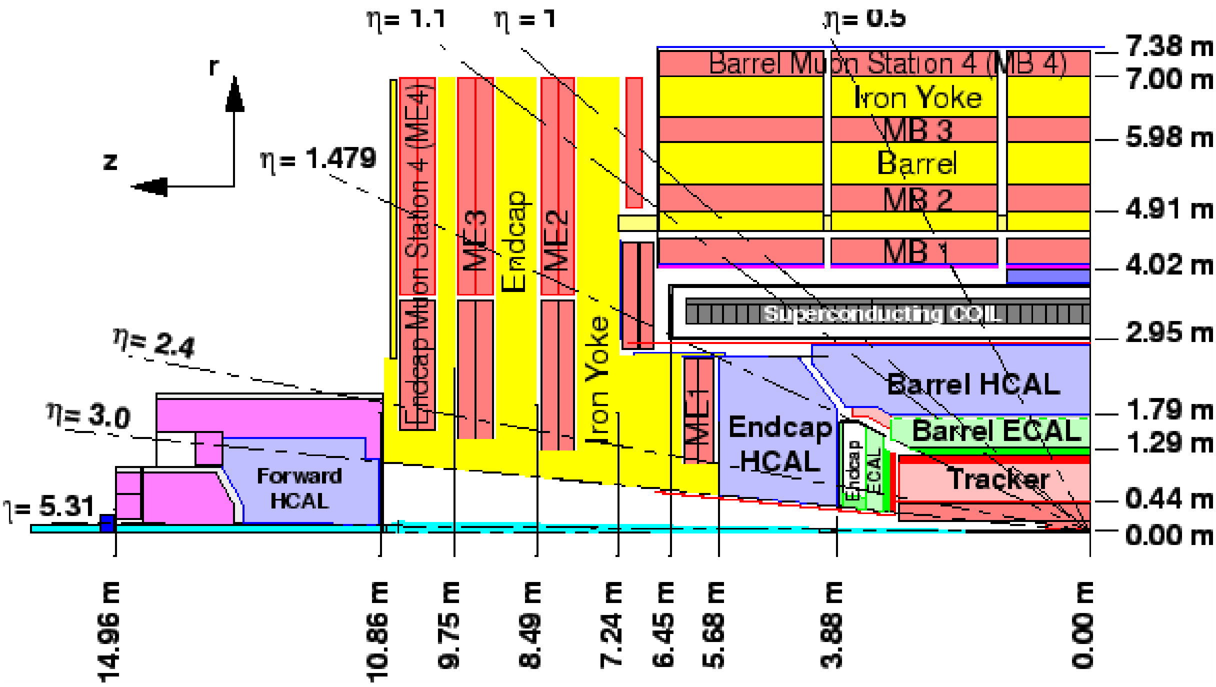

Figure 3.10: HCAL layout

Figure 3.11: ECAL barrel with crystals mounted

which collected in different layers of scintillator are combined together to measure the energy of the hadrons. The absorber is brass and Kuraray SCSN81 is the plastic scintillator which are stacked alternately. The scintillator is chosen to provide long-term stability and radiation hardness while the brass is chosen because of its density, non- magnetic and structural stability properties. Scintillator light is in the blue-violet range which passes through the wavelength-shifting fibers in the scintillator upto hybrid photodiodes (HPD), where the signals are converted into electrical pulses. There are about 70000 scintillator tiles in HCAL , which are sandwiched between the absorber layers made of brass in order to form projective towers to measure hadronic showers energy.

Figure 3.11 shows the sandwich structure and 3.10 shows the layout of HCAL. There are three major components of HCAL: barrel HCAL region (HB $|\eta| < 1.3$), the endcap region (HE $1.3 < |\eta| < 3.0$) and the forward region (HF $3.0 < |\eta| < 5.2$). HB is partitioned into two identical half barrels on either side of the interaction point. Each consists of 18 identical azimuthal wedges each of which covers 20 degrees in ϕ. Each of the wedges is further divided into four azimuthal sections which leads to a granularity of $\Delta\phi = 0.087$. The azimuthal wedges are also segmented into 16 partitions along the zdirection resulting in a granularity of $\Delta\eta = 0.087$. Total thickness of the absorber at $\eta = 0$ is 5.82 interaction lengths(λ_I). The effective thickness of the HB increases as a function of 1/sinθ which results in $10.6\lambda_I$ at $|\eta| = 1.3$. The ECAL crystals in front of HB add an additional $1.1\lambda_I$. In the barrel region, the combined stopping power of EB plus HB is not sufficient to provide containment for hadron showers. Hence, in order to ensure adequate sampling depth for $|\eta| < 1.3$, the hadron calorimeter is extended beyond the solenoid with a segment called the outer hadron calorimeter(HO). The solenoid coil adds an additional absorber equal to 1.4/sinθ interaction lengths in front of the HO and is used to identify late starting showers and also to measure the shower energy deposited after HB. Thus the total depth of the calorimeter system gets extended to a minimum of $11.8\lambda_I$ with the only exception being at the barrel-endcap boundary.

HE is also a sampling calorimeter which is composed of 17 layers. 79 mm thick brass absorber plates are sandwiched with 3.7 mm thick scintillator plates (there is a 9 mm thick Bicron scintillator for the starting later, layer 0). The granularity is 0.087 0.087 in $\delta\phi$ and $\delta\eta$ up to $|\eta| < 1.6$ while it is 0.17 0.17 for $|\eta| > 1.6$. There is overlap of HB and HE for only one trigger tower. HE has a minimum interaction length of about $10\lambda_I$. The HF is situated 11m away from the interaction point but it is very close to the beam axis. It is designed with steel absorbers and quartz scintillating fibers. These materials were chosen because of their radiation-hard properties enabling them to survive the particle

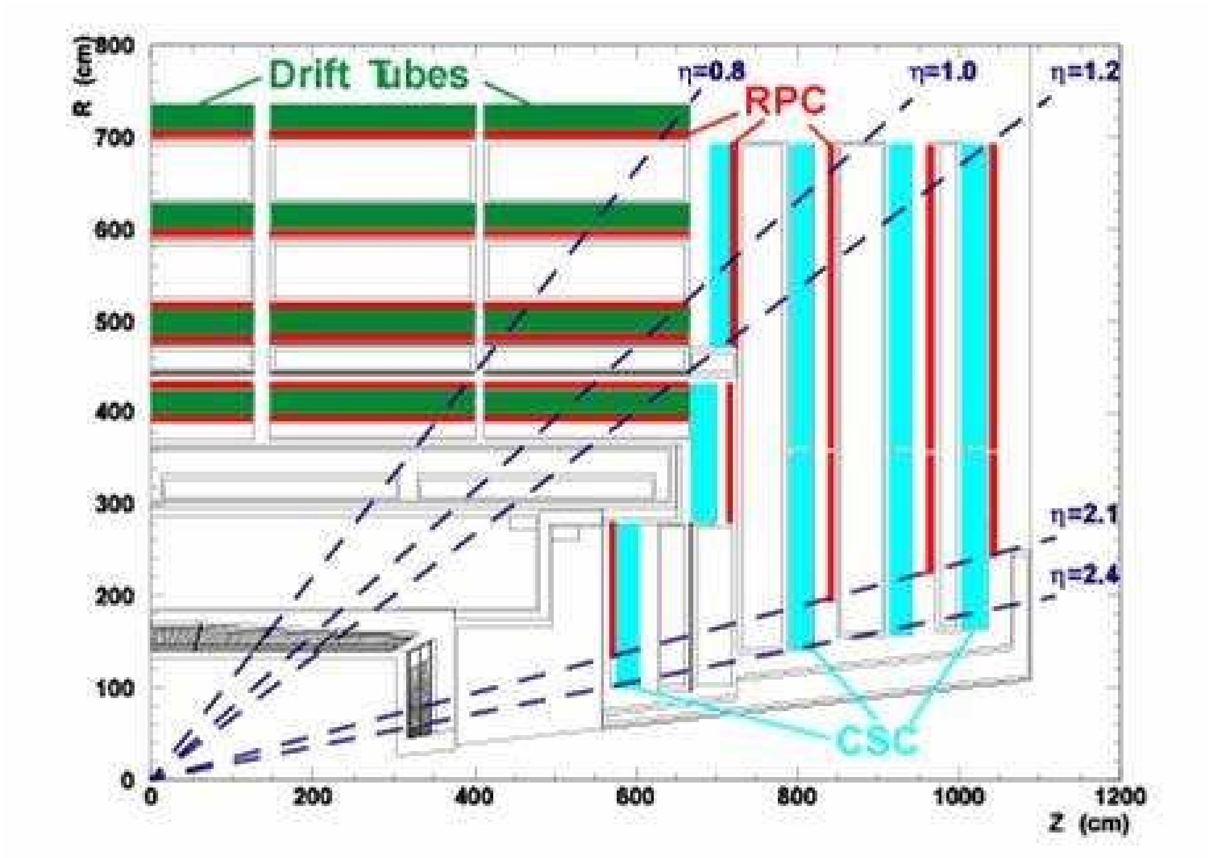

Figure 3.12: Muon systems layour in one quadrant of CMS.

flux at high η, where 8 times more energy than the barrel is deposited. Photomultiplier tubes are used to read the signals in this forward region.
Eac subsystem of HCAL has granularity designed in such a way so that jet energy resolution varies similarly with E_T for each of the subsystems. The energy resolution for single pions are parametrized as :

$$\frac{\sigma(E)}{E} = \frac{S}{\sqrt{E}} \otimes C \tag{3.2}$$

where S is $\sim$ 84.7% (leakage and sampling fluctuations) and C is $\sim$ 7.4% (inhomogenities).

3.2.4 Muon Systems

The design of CMS placed a lot of importance on the muon system which is apparent from the name of the detector. Decay of SM Higgs into ZZ with further decay to muons is an important channel for observing higgs since muons have a clean signature and are less affected by radiative losses than electrons. This along with other SUSY models have high chances of being observed in muon final states which necessitates wide angular coverage for muon detection.
The important functions of the muon system are identification, momentum measurement

and triggering. The high magnetic field and its flux return yoke leads to good momentum resolution and triggering. The muon system is cylindrical in the barrel with two planar endcap sections. The muon chambers are designed to be inexpensive, robust and reliable. There are three types of gaseous detectors, Cathode Strip Chambers (CSC), Resistive Plate Chamber (RPC) and Drift Tubes (DT). These are visible in figure 3.12. Within themselves they cover the interval $|\eta| < 2.4$ with no gaps which make reconstruction of muons with range 10 GeV $< p_T <$ 1 TeV within this pseudorapidity range.

3.2.4.1 Drift Tube System

The DT system covers the range $|\eta| < 1.2$. It is composed of four concentric cylindrical stations surrounding the beam lines. The first three inner cylinders have 60 drift chambers each and the outer cylinder has 70 chambers. There are 172,000 sensitive wires with wire length of 2.4m where the wire length is constrained by the longitudinal segmentation of the iron yoke. The drift cell as a transverse dimension of 21mm with a drift time of 380ns (gas mixture of 80%Ar + 15%CO_2) giving a position resolution of 100μm in r-ϕ plane.

3.2.4.2 Cathode Strip Chamber

The CSC is used to detect muons in the endcap where the magnetic field is non-uniform and there is a large neutron flux. Multi-wire proportional chambers which are made of 6 anode wire planes interspaced between 7 cathode panels. Wires run along azimuthal direction defining the radial coordinate of tracks. The CSC's have a fast response time which is important for triggering, finely segmented providing good spatial resolution and are radiation hard. A muon crosses 3 or 4 CSC's in the range $1.2 < |\eta| < 2.4$. In the barrel-endcap overlap region in the range $0.9 < |\eta| < 1.2$ both the DT in the barrel and CSC in the endcap detect muons.

3.2.4.3 Resistive Plate Chambers

RPC's are gaseous parallel plate detectors that have high spatial resolution as well as high timing resolution comparable to scintillators. RPC's can tag the timings of ionizing events in shorter time than 25ns which is the time between 2 LHC bunch crossings(BX). This allows for a fast RPC based dedicated muon trigger which helps in identifying the BX to which a muon track is associated in spite of the high rate of expected background. The RPC has 2 gaps, called up and down gap. They are operated in avalanche mode and they have common pick-up strips in between them. The sum of the 2 single-gap signals give the total induced signal. This setup enables the single -gaps to operate at lower gas gains with effective detector efficiency higher than single-gap. The RPC's cover the range

$|\eta| < 1.6$ in the endcap.

3.2.5 Trigger System

At its peak luminosity, the LHC is designed to produce ∼40million collisions per second. Most of these collisions produce scattering events and low energy interactions which are less likely to reveal new physics and also processing so much information will take a long time. Thus a trigger system is designed to select probable interesting events while reducing the rate to few hundred events per second before saving the information in computer disks for further analysis. The CMS trigger system has 2 tiers: Level-1(L1) and High Level Trigger (HLT). This reduces event rates from 40MHz to 100kHz. In the L1 system, the digitized signals from the detectors are processed into trigger primitives containing position, direction, BX and quality information. These primitives are built into larger objects to check if the events pass local, regional and global triggers while the rest of event information is held in the pipeline. These thresholds which are set in the trigger menu configuration changes with beam energy and instantaneous luminosity when the prescales are changed (prescale is the fraction of interesting events to be saved). The L1 selection is designed to be done within $\sim 1\mu$s. The front-end electronics stores event information for 3μs which corresponds to information from 128 BX. With this reduced rate the L1 trigger sends information to HLT once every 10μs.

L1 is based on mostly programmable electronics and the HLT is a software system running on commercial computing processors. HLT system which is run by the Data Acquisition(DAQ) system accesses sub-detector information from each event and builds physics objects like jets and photons (with simpler algorithms than what is employed offline since timing is a constraint online) to arrive at complex event level decisions. At HLT level, single event is processed in ∼10s while the data rate is reduced to 100Hz, which is compatible with the budget alloted to be read out and saved in computer disks.

Fig 3.13 shows schematic of the 2 level trigger system in CMS and L1 trigger system.

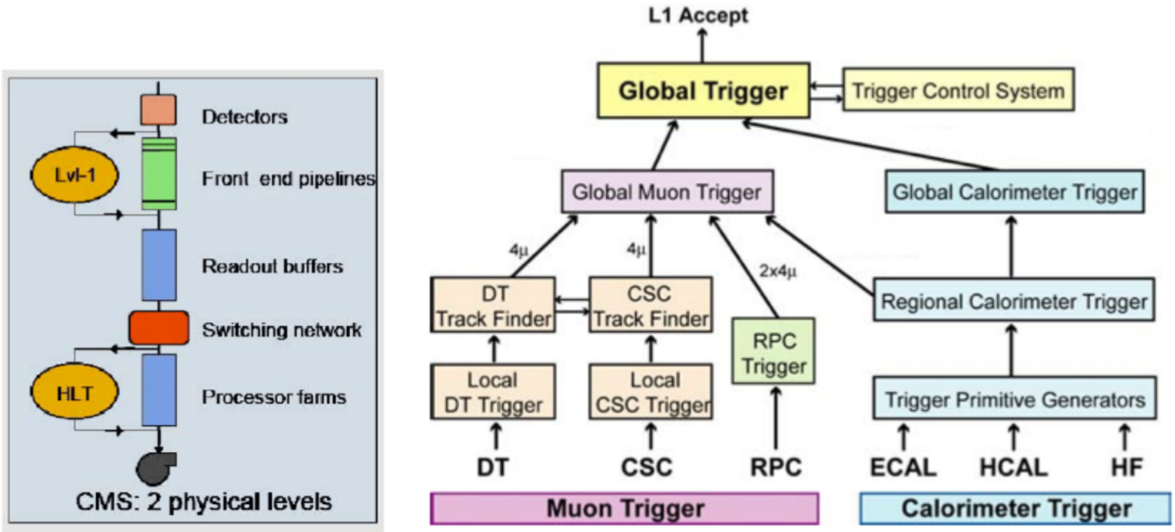

Figure 3.13: Schematic of the 2 level trigger system in CMS (left panel) and L1 trigger system (right panel)

Chapter 4

Event and Object Reconstruction

The event and object reconstruction happens in steps. First the digitized signals from the sub-detectors are converted into objects called "hits" which contain information about energy, timings and the global detector position. Then these hits are combined into more complex objects and particle candidate 4-momenta using various algorithms. A few of the steps are also carried out sometimes in a simplified form at Trigger level to identify interesting events where the full reconstruction is run later offline.
CMS uses an algorithm called Particle Flow(PF) [].

Information from all the subdetectors are combined to uniquely identify all stable particles coming out from each p-p collision. The PF algorithm is successful due to the excellent position resolution of the tracker and energy resolution of the ECAL. The algorithm used for track reconstruction uses an iterative pattern recognition algorithm which has high efficiency in dense environments typical for jets as well as low track misreconstruction rate of less than a percent in most difficult scenarios(low $p_T \sim 100 MeV/c^2$ tracks). A clustering algorithm is used for calorimeter deposits which has been optimized to have high efficiency for particles with low energy as well as providing good separation between nearby deposits. Another linking algorithm associates tracks with calorimeter deposits. PF identifies muons by matching tracks in the tracker as well as in the muon systems while electrons are reconstructed by associating tracks with calorimeter deposits. The remaining particles like charged and neutral hadrons as well as photons are identified by comparing track momentum with calorimeter deposits. The final list of PF particles are given as input to jet algorithm as well calculating missing energy. This chapter briefly discussed an overview of photon reconstruction as well as missing transverse momentum, which are important for the analysis described later in the thesis.

4.1 Photon Reconstruction and Identification

4.1.1 Photon Reconstruction

A Photon mostly deposits all of its energy in the ECAL crystals and photon candidates are reconstructed from these ECAL clusters of energy. There is some spread expected in the energy deposit since the material in front of the ECAL gives rise to conversions along with bremsstrahlung from electrons and positrons and in presence of the strong magnetic field along the beam direction there is a spread of energy in ϕ. As a result the first step in photon reconstruction [18] is to accumulate crystals with energy deposits that come from the same particle by using supercluster algorithm [19] In the barrel region of ECAL, Hybrid superclustering algorithm is used. First it looks for a crystal (called seed crystal) with energy beyond a threshold called (called $E^{min}_{T,seed} > 1GeV$). Then around this seed crystal, an array of 5×1 crystals are added in the $\eta - \phi$ plane in a range of N_{steps} (= 17 ∼0.3 radians) number of crystals in both directions in ϕ if their energies are above a threshold denoted as $E^{min}_{array}(> 0.1GeV)$. These arrays are further grouped into clusters where each of the clusters require a seed array with energy beyond a threshold of $E^{min}_{seed-array}(> 0.35GeV)$. Clusters satisfying this requirement are stored in global supercluster (SC). In the endcap and preshower regions the SC's are constructed in a similar way by the Multi-5 × 5 algorithm which add fixed arrays of 5×5 crystals together (same ref as before). The superclusters thus formed are corrected for losses due to interaction with the material in front of the ECAL and also the shower containment of the SC. Further corrections are added to take into account the η dependent lateral energy leakage due to the 3° offset in ECAL. These corrections are usually obtained using simulated samples and the corrections amount to $\sim 1\%$ of the SC energy.

During Run 2 datataking, an alternative algorithm was also employed. In this method of clustering called mustache clustering, all the crystals contiguous to a seed crystal were combined together to reconstruct clusters only if the energy deposit exceeded two standard deviations beyond the electronic noise. In the EB, a crystal was considered as a seed if $E_{seed} > 230$ MeV and in the EE $E_{seed} > 600$ MeV or $E^{T}_{seed} > 150$ MeV. This method provided significant improvements to energy resolution in Run 2.

The SCs of photon objects are connected to the primary vertex(PV) in an event which enables the calculation of the momentum and trajectory of the photon. The energy assigned to the photon candidate is determined by looking at the energy distribution in the photon object with the help of a variable called R9 which is the ratio of energy deposited in 3×3 matrix of crystals around the seed crystal to the total energy deposited in the SC.

Figure 4.1 shows the distributions of R9. Values of R9< 0.94 indicate broad spread in

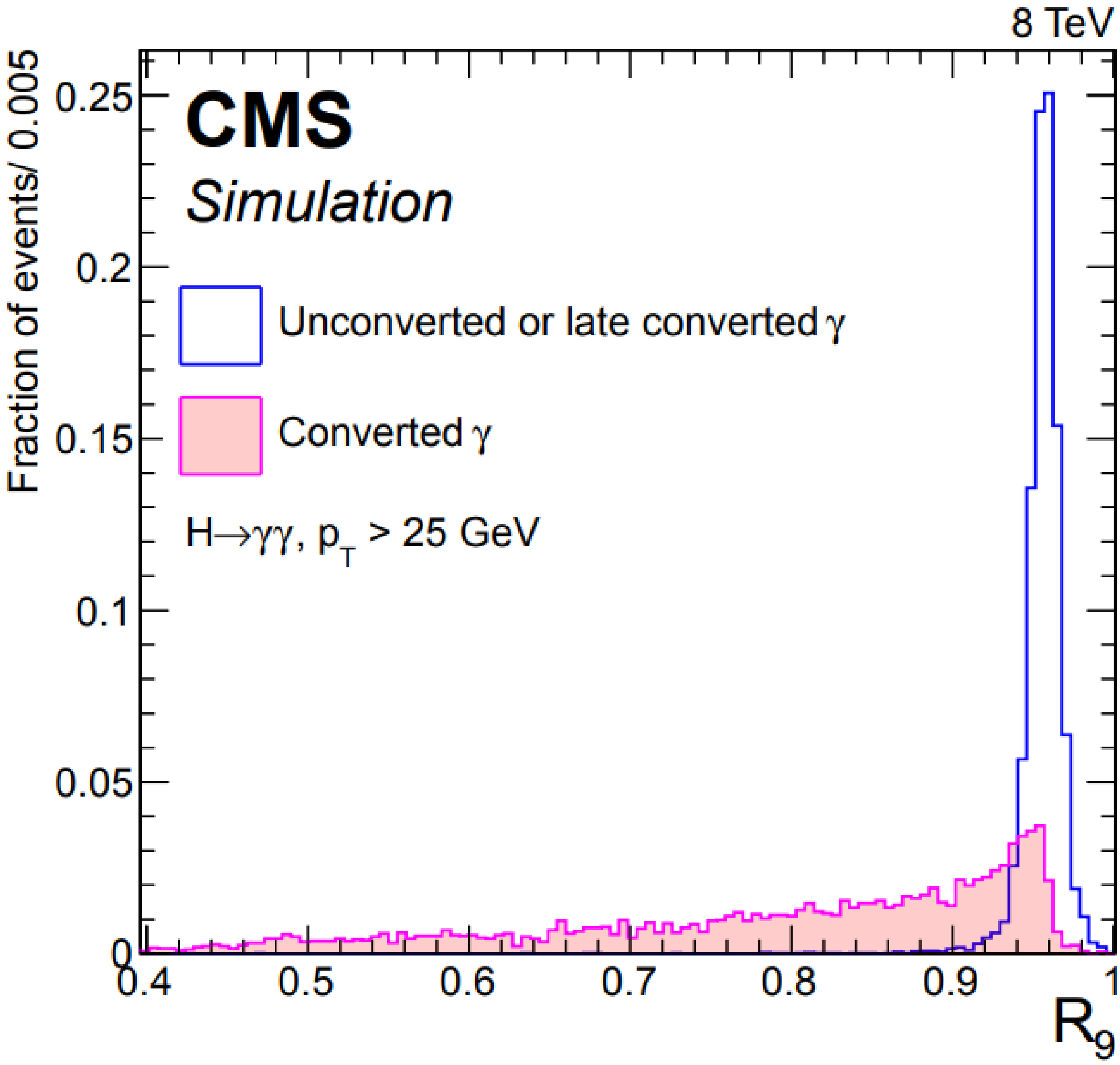

Figure 4.1: Distribution of R9 in barrel. Solid histogram corresponds to photons converting in the tracker while the outlined histogram shows photons which convert late or do not convert at all before reaching the ECAL.

energy due to photons converting before reaching ECAL and in this case the photon object is assigned the SC energy. If R9> 0.94 then that indicates a collimated deposit of energy coming from an unconverted photon and the photon object is assigned the energy of the 5×5 crystals surrounding the seed crystal. The position of the photon object is assigned by calculating the log-energy-weighed average position of the crystals in the clusters used for the determination of energy.

4.1.2 Photon Identification

There are a number of variables related to photon candidates which are defined to distinguish photons from electrons, jets and objects which have similar energy signals in the ECAL as photons. They are briefly described below:

- **Shower Shape variable($\sigma_{i\eta i\eta}$)**:
  The width of the electromagnetic shower along eta in terms of number of crystals in eta is given by $\sigma_{i\eta i\eta}$ which is calculated as follows:

$$\begin{aligned} \sigma^2_{i\eta i\eta} &= \frac{\sum_{i=1}^{5\times5} w_i(\eta_i - \overline{\eta}_{5\times5})^2}{\sum_{i=1}^{5\times5} w_i} \\ where, w_i &= max(0, 4.7 + \ln \frac{E_i}{E_{5\times5}}) \end{aligned} \tag{4.1}$$

  Here the i index runs over all the crystals within the 5×5 ECAL cluster centered on the seed crystal, E_i and η_i are energy and pseudorapidity of the i^{th} crystal inside the cluster, $E_{5\times5}$ is the energy of the full 5×5 cluster and $\overline{\eta}_{5\times5}$ gives the energy weighted mean position of the cluster in η. This variable gives how broadly the shower is spread in η. Since the photon trajectory is unaffected by the magnetic field, this variable should have low values while it should have larger values for π^0.

- **Hadronic over Electromagnetic calorimeter energy ratio (H/E)**: This variable gives the ratio of the energy deposited in the HCAL to that in ECAL within a cone of $\Delta R = 0.15$ ($\Delta R = \sqrt{(\Delta\eta)^2 + (\Delta\phi)^2}$) around the ECAL SC. Photons have a small value for this variable but for jets which have both electromagnetic and hadronic components in their energy this variable has larger values.

- **PF Charged Hadron Isolation** The sum of p_T of all charged hadrons within a cone of $0.3 > \Delta R > 0.02$ around the photon SC is defined as PF Charged Hadron Isolation (I_{CH}). Photons coming from hard scattering have lower values while photons coming from fragmentation and decay processes have other charged particles around them leading to a higher value of I_{CH}.

- **PF Neutral Hadron Isolation** The sum of p_T of all neutral hadrons within a cone of $\Delta R = 0.3$ around the SC is defined as PF Neutral Hadron Isolation (I_{NH}). Prompt photons have lower values of this variable.

- **PF Photon Isolation** The sum of p_T of all photons within a cone of $\Delta R = 0.3$ excluding a strip in η of 0.015 about the SC is defined as PF Photon Isolation (I_{PH}). This variable also has lower values for prompt photons.

The energy deposit in the calorimeter also has added contribution from overlapping p-p interactions called pile-up(PU). PU contribution in the isolation region is estimated as $\rho\times$EA where ρ is defined as the median of the transverse energy density per unit area in an event and EA is defined as the effective area of the isolation region which is weighted by a factor which takes into account the η dependence of transverse energy density coming from PU. To reduce PU dependency from the isolation variables, the PU contribution calculated using ρ is subtracted from charged hadron,neutral hadron and photon isolations. There are three sets of selection criteria for the variables which have been described above. They are termed "loose","medium" and "tight". The loose set of selections have high($\sim$ 90%) signal efficiency with low background rejection as well whereas the tight selection has ($\sim$ 70%) signal efficiency but with much higher background rejection. The loose leads to more statistics but introduces more background and tight criteria does the opposite. The medium set of selection sits in between these two with signal efficiency of $\sim$ 80% which is the usual prescription recommended by CMS for generic measurements.

4.2 Missing Transverse Momentum

The modulus of the vector which balances the $\vec{p_T}$ sum of all other objects in the event is defined as missing transverse momentum (MET) p_T^{miss}. There are many ways to reconstruct MET and for this analysis MET is calculated by PF algorithm. PF reconstructs all the visible particles in an event and constructs MET from their transverse momentum [20]. While p_T^{miss} is calculated with good accuracy the same is not true for missing longitudinal energy with inherent uncertainty coming from the uncertainty in the net longitudinal energy of the quarks in the proton bunches. The $\sum \vec{p_T}$ reconstruction in an event which leads to p_T^{miss} calculation is tested with MinBias and QCD multijet events which are expected to have balanced momentum in the plane transverse to the beam axis and minimal p_T^{miss}. Properly reconstructing events that have balanced transverse momentum is essential for fine tuning the noise cleaning of calorimeters. This enables removal of anomalous signals due to ECAL and HCAL electronics.

A wide range of effects lead to underestimation or overestimation of p_T^{miss} like nonlinear response of calorimeters, energy thresholds of various subdetectors and inefficiencies. As a result many corrections are applied to the p_T^{miss} measurement. The most important correction called Type-1 correction is applied to p_T^{miss} to modify the jet energies in events having p_T above a threshold. There are special filters which have been developed to filter events with not reliable p_T^{miss} which are discussed below.

- Track failure filter: This filter rejects events where calorimeter deposit do not have expected matching tracks
- Tracking POG filter: This filters events where tracks are not reconstructed because the reconstruction algorithm aborted due to CPU time limitations.
- ECAL dead cell trigger primitive filter: This filter rejects events where the transverse energy of trigger primitive at masked crystal cells are greater than 63.75 GeV
- HCAL LAser Filter: This filter rejects events where there is an overlap between HCAL laser firing and LHC bunch crossing.
- HBHE Noise Filter: This filter removes events with noisy HPD's (hybrid photo diodes used in converting scintillation light)
- CSC filter: This filter rejects events where a secondary particle shower has been produced due to collisions of the beam with residual gas in the beam pipes.

Chapter 5

Search for Dark Matter and Large Extra Dimensions in Monophoton Final State

5.1 Introduction

As discussed earlier, final state with a high-energy photon and large missing momentum is an important probe into new physics phenomena, such as production of dark matter (DM) particles [21] or gravitons under models with large extra dimensions [22]. This analysis searches for new physics in events with such a monophoton signature, in proton-proton collision data at $\sqrt{s} = 13\text{TeV}$, corresponding to $36fb^{-1}$ collected by the CMS experiment during 2016.

There is a similar search [23] with ATLAS detector using $39.6fb^{-1}$ collision data at $\sqrt{s} = 13\text{TeV}$ collected in 2016 which found no evidence of new physics. Previous search [24] at the CMS experiment with $12.9fb^{-1}$ data (a part of data taken during 2016) set model-dependent cross section upper limits for dark matter and ADD graviton production. For the ADD model depending on the number of extra dimensions, $M_D > 2.31 \sim 2.49\text{TeV}$ is excluded. For simplified dark matter production models with an s-channel mediator, mediator masses of up to 700 GeV have been excluded for low-mass dark matter.

5.2 Data Sets

5.2.1 Data sample

All events in the signal and background region were selected from SinglePhoton dataset corresponding to 35.9 fb^{-1} of data. For trigger efficiency measurements, JetHT dataset was used. Events which were certified to be good for all physics analyses by each of the sub-detector sub-groups were considered for event selection.

5.2.2 Monte Carlo samples

Simulated signal and background samples were generated using Monte Carlo (MC) event generators. These samples were used to optimize the event selection, evaluate efficiencies and systematic uncertainties, and compute expected yields.

The samples generated were : $Z(\to \nu\nu) + \gamma$,$Z(\to \ell\ell) + \gamma$, $W(\to \ell\nu) + \gamma$, $W(\to \mu\nu)$, $W(\to \tau\nu)$, $\gamma +$ jets, $t\bar{t} + \gamma$, t $+ \gamma$, WW, WZ and ZZ. Except for $t\bar{t} + \gamma$ and t $+ \gamma$, all other samples were generated at leading order (LO) in QCD. The parton distribution function (PDFs) used to produce these LO samples was NNPDF3.0 [25] with strong coupling constant value $\alpha_s = 0.130$ whereas for the next-to-leading-order (NLO) samples, the NNPDF3.1 next-to-next-to-leading-order (NNLO) PDF set with $\alpha_s = 0.118$ was used. For the $Z + \gamma$, $W + \gamma$,$\gamma +$ jets, $t\bar{t} + \gamma$ and t $+ \gamma$ samples, extra colored partons were generated together with the primary process to simulate the kinematics of high-energy events better. The primary hard interaction was simulated using MadGraph5_aMC@NLO version 2.2.2. Parton showering and hadronization were provided by PYTHIA 8.212 with the underlying-event tune CUETP8M1.

When considering the DM signal process, MadGraph5_aMC@NLO version 2.2.2 was used to produce the samples at NLO with $E_{\mathrm{T}}^{\gamma} > 130$ GeV and $|\eta^{\gamma}| < 2.5$. Samples were generated with varying m_{DM} and M_{med}. For ADD model, samples were generated using Pythia8, with $E_{\mathrm{T}}^{\gamma} > 130$. Samples were created for different number of extra dimensions and M_D.

For all processes, the detector response was simulated using a detailed description of the CMS detector, based on the GEANT4 package [26]. Minimum bias events were superimposed on the simulated events to emulate the additional pp interactions per bunch crossing (pile-up). These samples are re-weighted to represent the pile-up distribution as measured in the data. The reconstructed vertex with the largest value of summed physics-object p_T^2 was taken to be the primary pp interaction vertex. The physics objects were the jets, clustered using the jet finding algorithm with the tracks assigned to the vertex as inputs, and the associated missing transverse momentum, taken as the negative vector sum of the p_T of those jets.

The background simulated processes can mimic the $\gamma + p_T^{miss}$ final state in the following ways:

- $Z(\rightarrow \nu\nu) + \gamma$ has real p_T^{miss} and a real photon in the final state and is the irreducible background.
- $W(\rightarrow \ell\nu) + \gamma$ in which the charged lepton is lost or misreconstructed as a photon.
- Inclusive $W(\rightarrow \ell\nu)$ production where the lepton fakes a photon.
- $Z(\rightarrow \ell\ell) + \gamma$ in which both leptons are lost or misreconstructed.
- $t\bar{t} + \gamma$ and $\mathrm{t} + \gamma$ where one or two top quarks decay leptonically, and the charged lepton is lost or misreconstructed.
- Other $\gamma + X$ events in which the p_T^{miss} is mismeasured.

5.3 Event selection and object definition

5.3.1 Analysis strategy

This analysis looks for an excess of events with large p_T^{miss} from what is expected from standard model prediction. The selections for the signal and control regions are discussed below.

Events were collected with a single-photon trigger ($HLT\_Photon165\_HE10\_v*$) which requires minimum one photon candidate with $p_T > 165$ GeV. The candidate's H/E (fraction of energy deposited in Hadron calorimeter over that deposited in electromagnetic calorimeter) was required to be < 0.1 to get rid of jets. The thresholds for both H/E and p_T were loose since the photon energy reconstructed at the HLT is less precise than what is obtained from offline reconstruction. The trigger was found to be 99% efficient for events passing the selections.

Photon candidates were selected on the basis of their calorimetric information and isolation which discriminate photons from electromagnetic showers from hadrons. To distinguish from electron, a lack of a matching track in the tracker is required. Calorimetric requirements included $\sigma_{i\eta i\eta}$ (measure of width of EM shower in η) < 0.0102 and H/E $<$ 0.05. $\sigma_{i\eta i\eta}$ is usually larger in showers coming from hadronic activity. The scalar sums of the transverse momenta of charged hadrons, neutral hadrons, and photons within a cone of $\Delta\mathrm{R} = \sqrt{(\Delta\eta)^2 + (\Delta\phi)^2} < 0.3$ around the photon candidate are required to below certain values chosen to give 80% signal efficiency. The PF candidates not overlapping with

the candidate EM shower are included in the isolation calculation. The PF candidates are ideally required to come from the same interaction vertex as the photon candidate, but ambiguity arises since the photons have no tracks associated with them. Due to this, the maximum charged-hadron isolation value over all vertex hypotheses (called worst isolation) is used which also takes cares of conversions in the detector material in front of the ECAL.
ECAL clusters formed from processes other than pp collisions can also be misidentified as photons. Anomalous energy deposits in the ECAL include spikes, which come from particle inteaction in ECAL photodetectors and bremsstrahlung photons from muons travelling along the beam have non-negligible contribution. Spikes are removed by requiring more than one ECAL crystal in the candidate photon cluster and to remove beam halo the photon cluster timing is required to be within ± 3 ns from the collision time. The shower shape also used to discriminate from these backgrounds.

The selections used to define the signal and control regions are summarized below.

5.3.2 Event selection for signal region

Candidate events in the signal region were selected by the following requirements.

- Events passing the HLT_Photon165_HE10_v* trigger
- At least one high-E_T photon candidate with $p_T > 175$GeV
- $p_T^{miss} > 170$GeV
- Separation of $p_T^{miss}$and the photon candidate in the azimuthal angle by more than 0.5 radians ($\Delta\phi(\gamma, p_T^{miss}) > 0.5$ to take care of photon energy mismeasurement giving rise to p_T^{miss})
- No electron or muon with p_T >10 GeV.
- No jet within 0.5 radians in the azimuthal angle from the p_T^{miss}direction ($\min \Delta\phi(\vec{p_T}^{\text{jet}}, \vec{p_T}^{miss}) >$ 0.5 to take care of jet energy mismeasurement giving rise to p_T^{miss})
- $p_T^{\gamma}/p_T^{miss}< 1.4$ to reject $\gamma +$ jets background
- Pass anomalous event filters ("MET filters")

The control regions are selected to gave orthogonal properties of the signal region which are used for further background estimations. The orthogonality ensures that there is no bias from the signal region in the estimations.

5.3.3 Event selection for control regions

5.3.3.1 Single-Muon control region

The single muon control region is obtained by selecting events having the same selection as signal region but with the following differences.

- Events must have exactly one muon, passing tight ID requirements with $p_T >$ 30GeV.
- Instead of requiring $p_T^{miss}>$ 170 GeV, we define Recoil (U) : Vector sum of $p_T^{miss}$and lepton p_T, which is then required to be greater than 170 GeV
- Transverse mass (lepton + p_T^{miss}) must be less than 160 GeV

5.3.3.2 Single-Electron control region

Similarly, the single electron control region is obtained by using the same selection as signal region with the following differences.

- Events must have exactly one electron, passing tight ID requirements with $p_T >$ 30GeV.
- Instead of requiring $p_T^{miss}>$ 170 GeV, we define Recoil (U) : Vector sum of $p_T^{miss}$and lepton pT, which is then required to be greater than 170 GeV
- p_T^{miss}in the event must be larger than 50 GeV to suppress QCD background
- Transverse mass (lepton + p_T^{miss}) must be less than 160 GeV

5.3.3.3 Double-Muon control region

The double muon control region is obtained using the same selection as signal region with the following differences.

- Events must have exactly two loose muons with opposite charge
- At least one of the muons passes the "tight ID" ("tight ID" corresponds to very high background rejection rate) requirements with $p_T >$ 30GeV
- The invariant mass of the 2 muons between 60 and 120 GeV
- Instead of requiring $p_T^{miss}>$ 170 GeV, we define Recoil (U) : Vector sum of p_T^{miss}, leading and sub-leading lepton pT, which is then required to be greater than 170 GeV

5.3.3.4 Double-Electron control region

The double electron control region is obtained using the same selection as signal region with the following differences.

- Events must have exactly two loose electrons with opposite charge
- At least one of the electrons passes the tight ID requirements with $p_T > 30\text{GeV}$
- The invariant mass of the 2 electrons between 60 and 120 GeV
- Recoil (U) is required to be greater than 170 GeV

5.4 Trigger Efficiency

The efficiency of the main single-photon trigger HLT_Photon165_HE10_v* is measured in data. The only requirement in this trigger is at least one photon with $E_T > 165\text{GeV}$ and $H/E < 0.1$ in the event. The photon objects are reconstructed around L1 seeds, which are L1 trigger objects firing either the SingleEG40 or the SingleJet200 L1 triggers.

The HLT trigger efficiency is biased due to the presence of additional HE10 (hadronic over electromagnetic calorimeter deposit ratio less than 10%) and NoHE (no cut on hadronic over electromagnetic calorimeter deposit ratio) cut in the triggers used in the numerator of trigger efficiency. Also to check the effect of L1 efficiency, the absolute unprescaled (”unprescaled” means every event selected by the event is stored whereas prescaled triggers store selected events at a fixed ”prescale” rate) single photon trigger efficiency was measured as a function of E_{T}^{γ} using the JetHT dataset which utilizes orthogonal criteria to the single photon trigger requirements.

To measure the efficiency, events were selected which passed prescaled triggers with lower E_T thresholds, namely HLT_Jet60* and HLT_Jet80* and HLT_Jet140*. Selection requirements of the analysis were applied on the events firing these triggers, and the rate at which such events also fired the main analysis trigger were computed. The corresponding trigger efficiency is shown in Figure5.1. We see that the single photon trigger is not fully efficient at high photon E_T (a known issue due to L1 Egamma seed not fully efficient at high pt). This loss in efficiency at high photon pt was corrected by applying a correction to MC.

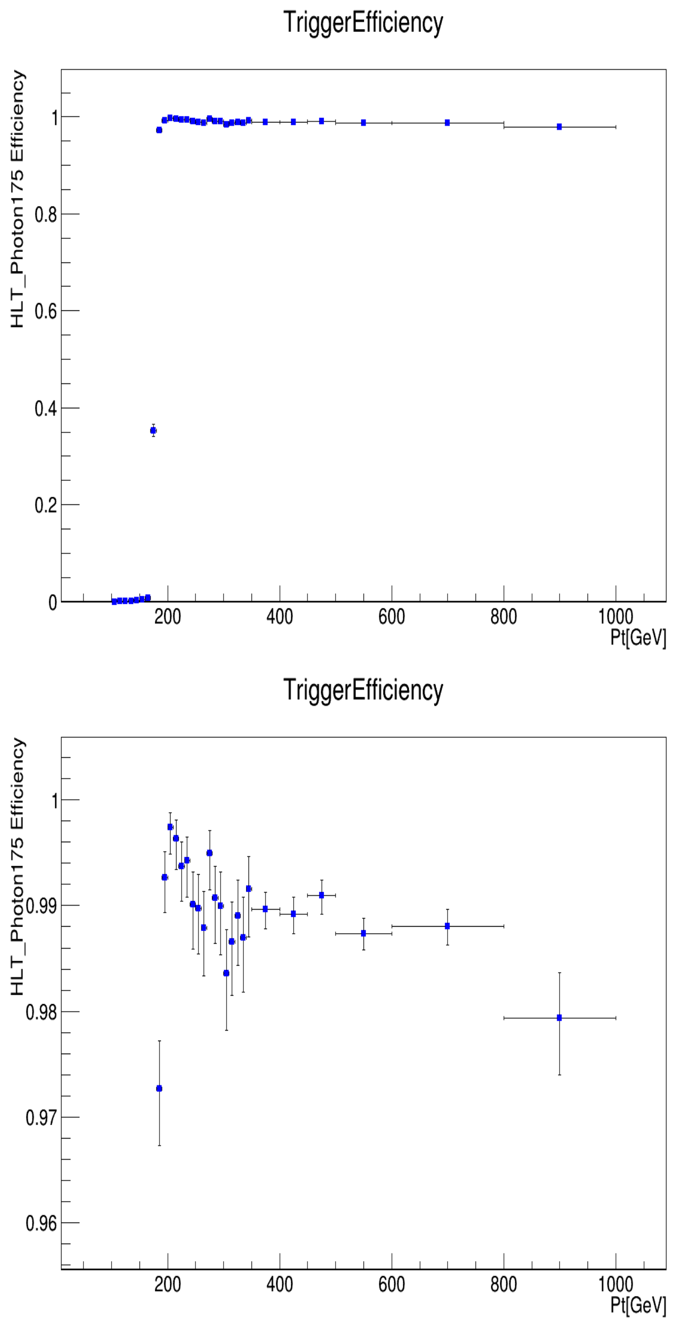

Figure 5.1: Absolute trigger efficiency for Single photon trigger as a function of photon p_T(left) and a zoomed version in (right).

5.5 Background estimation

5.5.1 Overview

There are multiple distinct sources of SM background to this analysis. The most significant is the production of a Z boson in association with a high-energy photon where the Z boson decays into a neutrino-antineutrino pair $(Z(\nu\nu) + \gamma)$ which is known as the irreducible backround. The second leading background contribution comes from the production of a W boson in association with a high-energy photon ($W \rightarrow l\nu\gamma$). These events become a background when the W boson decays leptonically and emits a neutrino or an antineutrino together with a charged lepton. Such events are usually rejected by electron and muon vetoes but hadronic tau events and events where the leptons are out of the reconstruction acceptance along with the imperfect efficiencies of vetoes give rise to this background. Together they comprise 70% of the total background with 50% coming from the $Z(\nu\nu) + \gamma$ process. These two background sources are estimated using simultaneous fits to the signal and control regions.

We also consider $Z(l\bar{l})+\gamma$, $t\bar{t}+\gamma$, $t+\gamma$, and $W \rightarrow \mu\nu$ with a strong collinear radiation from the muon. These processes, collectively denoted as minor SM backgrounds, can contribute in the signal region if the leptons go out of acceptance or are not captured by the veto. MC simulations are also used to predict their contribution.

Other important backgrounds appear when the candidate photon object is a misidentified electron (Section 5.5.4) or electromagnetic shower caused by hadrons (Section 5.5.5) are misidentified as candidate photons. Electron misidentification happens mostly from W boson production ($W \rightarrow e\nu$), whereas hadron misidentification can be due to multiple sources such as $Z(\rightarrow \nu\nu)$ + jets and QCD multijet with large mismeasured jet energy. Although these processes are rare but the above processes have high cross sections. Since object misidentification rates depend on subtle details of the detector, the MC simulation cannot be expected to model it reliably. Therefore, data-driven techniques are employed to estimate the contributions from these background events.

Jet energy mismeasurement can also make $\gamma +$ jets events appear to have large p_T^{miss}. However, $p_T^{miss}$is typically aligned with the photon or one of the jets in such cases, and therefore the requirements of $\Delta\phi(\gamma, p_T^{miss}) > 2$ and $\min \Delta\phi(\vec{p_T}^{\text{jet}}, \vec{p_T}^{miss}) > 0.5$ reduces this background very effectively. The residual of this background is estimated with MC simulation.

Finally, (apparent) large energy deposits in ECAL from non-collision processes can mimic $\gamma + p_T^{miss}$ events and therefore need to be controlled. Known sources of such background include bremsstrahlung of beam halo or cosmic ray muons and ECAL "spikes". These processes are described in detail in Section 5.5.6.

5.5.2 $Z + \gamma$ and $W + \gamma$

5.5.2.1 Higher-order corrections

The $Z(\nu\nu) + \gamma$ and $W(l\nu) + \gamma$ background contributions are modeled using MC simulations. Samples generated at LO in QCD by MADGRAPH5 with up to two additional

Table 5.1: NNLO / LO correction factors for $Z(\nu\nu)+\gamma$ and $W(l\nu)+\gamma$ samples.

p_{T}^{γ} range (GeV)	$Z(\nu\nu)+\gamma$	$W(l\nu)+\gamma$
$[175, 190]$	1.44	1.40
$[190, 250]$	1.41	1.37
$[250, 400]$	1.35	1.31
$[400, 700]$	1.29	1.26
$[700, \mathrm{inf}]$	1.15	1.15

partons and a generator-level requirement of $p_{\mathrm{T}}^{\gamma} > 130\mathrm{GeV}$ were used for this. Studies using privately generated aMC@NLO sample with high p_{T}^{γ} threshold confirmed that the predicted kinematic distributions would not change drastically by using the NLO sample.

To approximate the QCD higher-order effects, $Z(\nu\nu)+\gamma$ and $W(l\nu)+\gamma$ events were re-weighted in E_{T}^{γ} distribution by the factors given in Tab. 5.1. These factors are the ratios of QCD NNLO differential cross sections calculated by Grazzini et al. [27] to the LO cross sections given in the samples produced by CMS.

Additionally, factors to account for higher-order electroweak corrections were also applied as a function of E_{T}^{γ}. Out of various electroweak higher-order effects, ones that can give sizable ($\gg \mathcal{O}(\alpha)$) corrections to the cross section are Sudakov suppression at high boson $\mathrm{p_T}$and also the addition of photon-induced scattering processes [28, 29]. The correction factors shown in Figure 5.2 were applied, which are combinations of Sudakov suppression factors and photon-induced enhancements, and are provided by the authors of Ref. [29] on top of the NNLO QCD correction.

The differential cross section after the full higher-order corrections is therefore denoted as

$$d\sigma^{\text{NNLO QCD+NLO EW}} = d\sigma^{\text{LO}} k^{\text{NNLO QCD}} (1 + \kappa^{\text{EW Sudakov}} + \kappa^{\text{EW}q\gamma}),$$

where $k^{\text{NNLO QCD}} = d\sigma^{\text{NNLO QCD}} / d\sigma^{\text{LO}}$, and the two κ terms are the Sudakov suppression and photon-induced enhancement components of the electroweak correction, respectively.

Theoretical uncertainties on the electroweak corrections are not well understood to date. We estimate the magnitude of the uncertainty on $\kappa^{\text{EW Sudakov}}$ and $\kappa^{\text{EW}q\gamma}$ to be $(\kappa^{\text{EW Sudakov}})^2$ and $\kappa^{\text{EW}q\gamma}$, ie, square of the correction for Sudakov suppression and the 100% of the correction itself for the photon-induced enhancement. The choice of using the square of $\kappa^{\text{EW Sudakov}}$ is motivated by the fact that fully resummed leading-log Sudakov suppression is an exponential of $\kappa^{\text{EW Sudakov}}$.

For the Sudakov suppression, which is the dominant term in the electroweak correction, we further consider two types of systematic variations, inspired by ref. [31], which provides a prescription for electroweak correction uncertainties for V+jets processes. In this paper, electroweak correction as a function of the boson $\mathrm{p_T}$ is varied in overall scale and in slope.

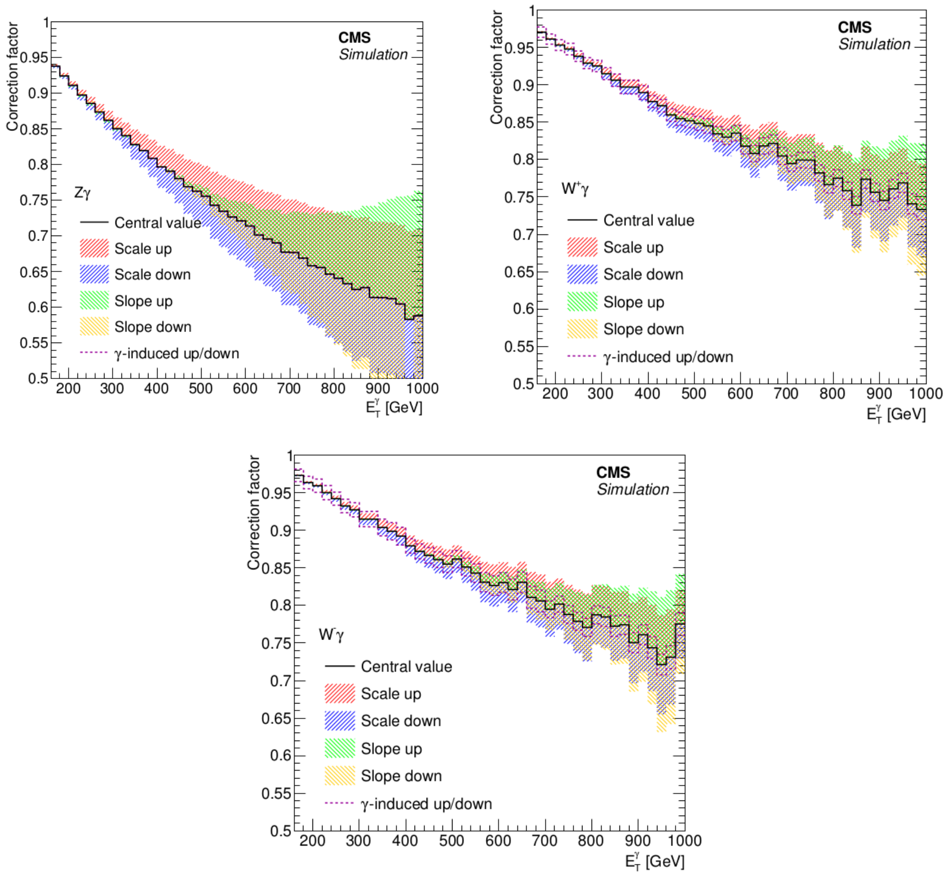

Figure 5.2: Electroweak NLO cross section corrections as a function of photon $\mathrm{p_T}$for $Z+\gamma$, $W^+ + \gamma$, and $W^- + \gamma$ processes, overlaid with uncertainty bands [30].

The slope variation is realized by selecting a point in the boson p_T spectrum and letting the shift in correction cross over at the point (see Figure 5.3). Following this prescription, we let the Sudakov suppression vary in overall scale and in slope, where we choose our crossover point for the slope variation to be at $E_T^\gamma = 590$GeV.

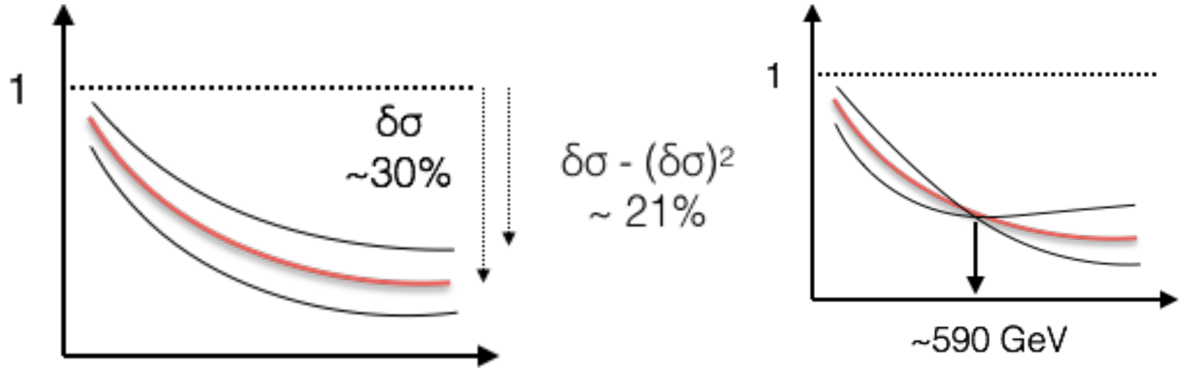

Figure 5.3: Electroweak correction variation scheme to cover the scale (left) and shape (right) uncertainties.

5.5.3 Estimation

The background estimation method exploits the cancellation of both experimental and theoretical uncertainities in the ratios of photon p_T distributions of V+γ processes which are called "transfer factors". The transfer factor between Z($\rightarrow \nu\bar{\nu}$) + γ and Z($\rightarrow l\bar{l}$) + γ processes is denoted by $R^{Z\gamma}_{ll\gamma}$ and in this ratio uncertainities related to jet energy resolution, photon energy calibration and higher order QCD effects are significantly reduced compared to the case when these effects are considered for the individual processes. The effects that do not largely cancel out are due to lepton identification efficiency and limited sample size. $R^{Z\gamma}_{ll\gamma}$ is the ratio of Z($\rightarrow \nu\bar{\nu}$) + γ yield in the combined signal region to the Z($\rightarrow l\bar{l}$)+γ yield in the relevant control region. For the dimuon and the dielectron control region are expressed as $R^{Z\gamma}_{\mu\mu\gamma}$ and $R^{Z\gamma}_{ee\gamma}$. Using the transfer factor, the estimated event yield in each bin of the dilepton control region $T_{ll\gamma}$ is given by:

$$T_{ll\gamma} = \frac{N^{Z\gamma}}{R^{Z\gamma}_{ll\gamma}} + b_{ll\gamma} \tag{5.1}$$

where $N^{Z\gamma}$ is the number of Z($\rightarrow \nu\bar{\nu}$) + γ events in the combined signal regions and $b_{ll\gamma}$ is the predicted contribution from other background sources in the control region.
Similar technique is used for estimating the W($\rightarrow$ $l\nu$) + γ background. The charged lepton from these processes either passes or fails the identification criteria and in the ratio of theses processes the non-negligible uncertainities are those from lepton identification

fficiency and MC sample size. The transfer factor is denoted by $R_{l\gamma}^{W\gamma}$ andit is the ratio of the estimated W($\rightarrow l\nu$) + γ yield in the combined signal region to the estimated W($\rightarrow l\nu$) + γ yield in the relevant control region. For the mono-electron and mono-muon control regions, they are denoted as $R_{e\gamma}^{W\gamma}$ and $R_{\mu\gamma}^{W\gamma}$.
The Z($\rightarrow \nu\bar{\nu}$) + γ and W($\rightarrow l\nu$) + γ yields in the signal regions are further constrained by an additional transfer factor denoted as $f_{W\gamma}^{Z\gamma}$. In this ratio, all experimental uncertainities related to data to simulatio corrections cancel out and the main uncertainities arise from higher order theoretical corrections.
Using hese transfer factors the event yields in each bin of single-lepton control region is given by:

$$T_{l\gamma} = \frac{N^{Z\gamma}}{R_{l\gamma}^{W\gamma} f_{W\gamma}^{Z\gamma}} + b_{l\gamma} \tag{5.2}$$

where $b_{l\gamma}$ gives the predicted contribution in the single-lepton control regions from other background sources. The transfer factors are discussed further in the results section.

5.5.4 Electron misidentification

An electron can be misidentified as a photon in cases when the track seeds associated in the pixel detector to the supercluster in ECAL for the electorn are missing due to errors in the reconstruction step. A single W boson decaying to an electron and a neutrino is a high-rate production process, and if the electron is misidentified, it mimics the photon plus p_T^{miss}signature .

This misidentification rate is proportional to the inefficiency $1 - \epsilon_e^{\text{pixel}}$ of the pixel seeding, defined with the electrons passing the photon identification criteria described in Sec. **??** except the pixel-seed veto. This partial identification is henceforth denoted as $e\gamma$ ID. Under the assumption that the kinematic and other properties of the electron plus p_T^{miss}events are mostly unaffected by the electron misidentification, the electron misidentification background can be modeled by taking a proxy sample with well-identified electrons and scaling this sample by $R_e = (1 - \epsilon_e^{pixel})/\epsilon_e^{pixel}$.

This scaling factor is estimated by exploiting the Z boson decay into an e^+e^- pair. In this method known as the "tag and probe" (TnP), first a high-quality electron object (tag) is identified in a single electron data sample, and then an accompanying electron is sought for in the set of electromagnetic objects (probes) in the event. The probes are required to pass the $e\gamma$ ID. The area under the Z boson mass peak in the invariant mass distribution of the TnP system is then measured by once applying the pixel-seed veto requirement on the probe and once inverting the veto. Denoting the two areas $N^{e\gamma}$ and N^{ee}, respectively, the ratio $N^{e\gamma}/N^{ee}$ is equal to R_e up to minor systematic corrections.

This TnP measurement is performed on a subset of the single photon triggered events where there the tag is an electron object passing the "tight" identification criteria in addition to the triggering photon (probe). All possible tag-probe combinations are considered where the tag objects can also be probes and the probe objects tags. The two combinations are considered independently to avoid the bias caused by preferring one object over another to use as the probe.

The TnP invariant mass distributions are then fit to extract $N^{e\gamma}$ and N^{ee}. The fit model is composed of two templates, where one template describes a pure $Z \to ee$ process shape and the other describes the background contributions to the overall shape. The backgrounds to the ee fit include $W +$ jets, diboson, and $t\bar{t}$ productions, which are all negligible and estimated to contribute by less than 1%. The backgrounds to the $e\gamma$ fit on the other hand mainly consist of processes with actual electron and photon in the final state, such as $W\gamma$ and $Z \to ee$ with a hard radiation off one of the electrons.

The $Z \to ee$ decay template is given by an analytic shape of Breit-Wigner distribution convoluted with the Crystal Ball function. The mass and width parameters of Breit-Wigner distribution are fixed to values following the PDG. Crystal Ball parameters are allowed to vary freely in the fit. The background template is given by an analytic shape of sigmoid multiplied with exponential function.

Figure 5.4 shows the 6 fits performed on ee and $e\gamma$ in bins of probe p_T, from which the R_e factor used for the estimation of the electron misidentification background is derived. The R_e factor is computed as the ratio of the integral of the signal template function between 81 GeVand 101 GeV.

Systematic uncertainties for this method are from the TnP fit and those related to the applicability of the R_e factor. The fit uncertainty includes statistical uncertainty and the potential mismodeling of the $Z \to ee$ shape and background shapes.

The statistical uncertainty of the fits are estimated by generating toy data from the nominal fit result with the same number of entries as the fit target distribution. The invariant mass distribution of the toy data is then fit with the same model with the parameters unconstrained. This procedure is repeated 100 times to obtain a distribution of the $Z \to ee$ event yields, and its standard deviation is taken as the statistical uncertainty of the fit. Relative statistical uncertainty on the R_e factor is 12-14% depending on the probe p_T bin.

To estimate the effect from potential mismodeling in the fits, alternative fits varying the background and signal templates are performed. In the alternative-background fit, the background model is a polynomial of order 2. In the alternative-signal fit, no Crystal Ball convolution is performed to the signal template and instead template from the Z(ee) MC sample is used. The average shift of the fit result from the nominal value is then taken as the uncertainty. The relative uncertainty on the R_e factor varies from 2 to 3%

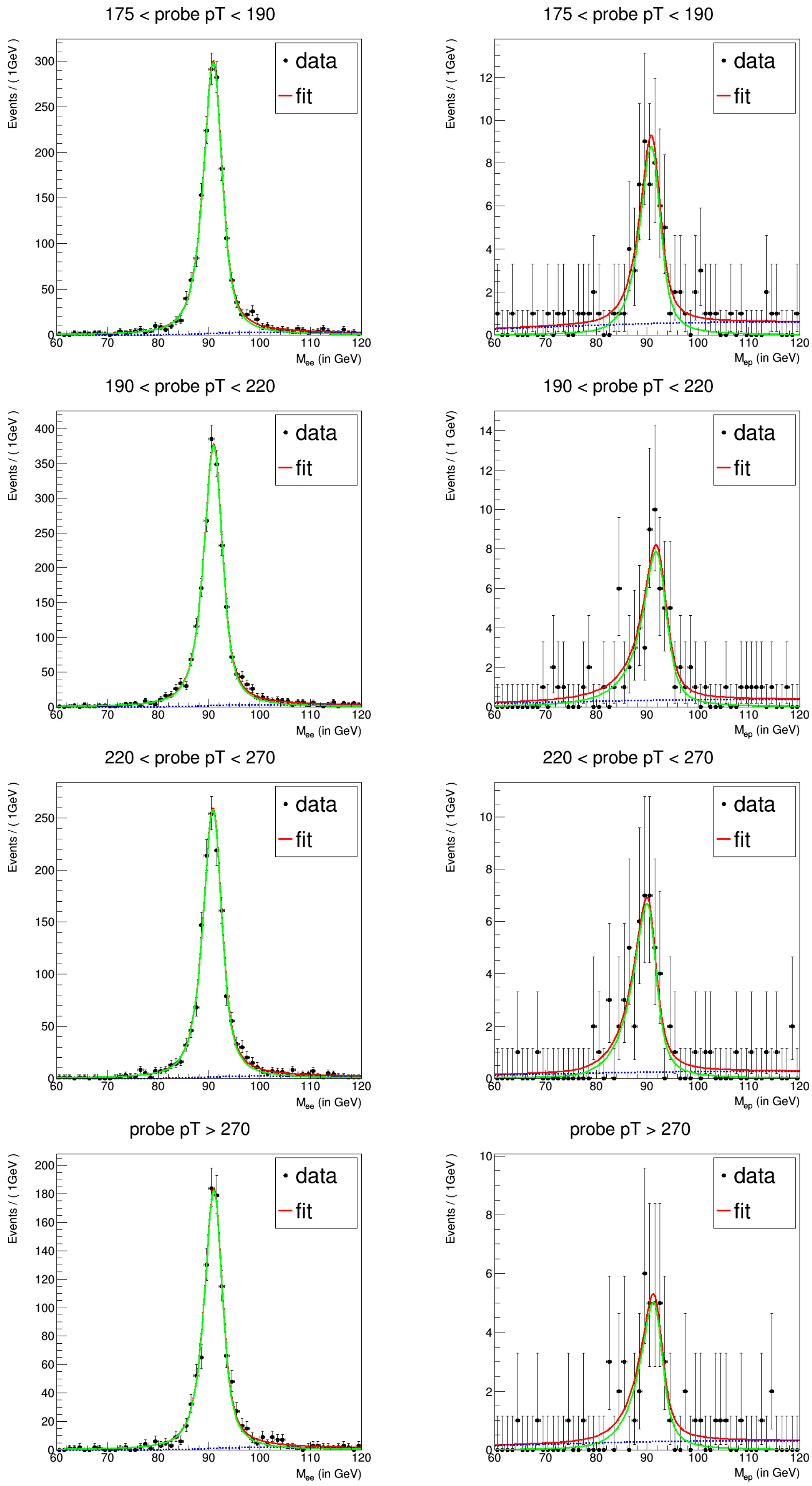

Figure 5.4: Fits to the mass distributions for ee(left) and $e\gamma$(right) selections, in bins of probe p_T : $175 < p_T < 190\text{GeV}, 190 < p_T < 220\text{GeV}, 220 < p_T > 270\text{GeV} and p_T > 270$. The red solid line represents the full fit model, and the blue dashed line its background component.

Table 5.2: Relative Statistical and systematic uncertainty on R_e as a function of probe p_T.

Probe p_T (GeV)	R_e	Statistical (%)	Systematic (%)
$[175, 190]$	0.032	12.3	4.4
$[190, 220]$	0.027	11.1	8.2
$[220, 270]$	0.031	12.2	3.6
$[270, inf]$	0.034	14.9	12.6

depending on the probe p_T bin.

The summary of statistical and systematic uncertainties on R_e are given in Table 5.2, where the systematic uncertainty is dominated by the modeling of the signal model. A proxy sample of events rich in electrons which otherwise pass the signal candidate criteria are scaled with this rate to get the contribution from fake electrons in the signal region.

Figure 5.5 shows the derived R_e factor as a function of E_{T}^{γ}.

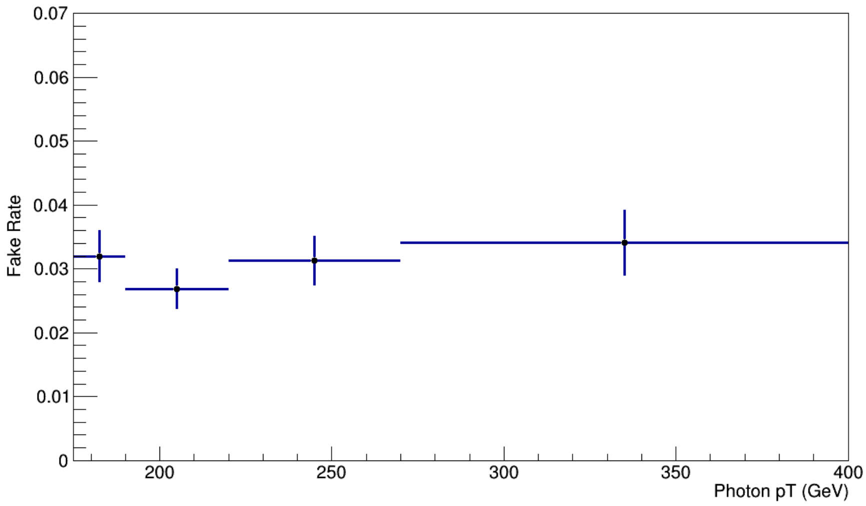

Figure 5.5: Electron to photon fake rate.

5.5.5 Hadron misidentification

Any analysis which involves photons in the final state is always subject to *fake* photons from QCD multi-jet events. These fakes appear when one of the high E_T jets fragments into an isolated π^0 or η which becomes sufficiently collimated to appear as a single electromagnetic shower in the ECAL.

The fraction of jets from QCD processes that are likely to pass the photon isolation selection requirements is small, but the overall production rate for these fake photons

Table 5.3: Requirements for reconstructed photon objects passing the numerator selections. In the QCD background sideband, the $I_{\mathrm{CH}}^{\mathrm{max}}$ requirement is changed to $8 < I_{\mathrm{CH}}^{\mathrm{max}} <$ 14GeV.

Category	Selection	
fiducial	p_T^{γ}	> 175 GeV
	$\lvert\eta^{\gamma}\rvert$	< 1.4442
photon ID	I_{NH}	$< 2.792 + 0.0112 p_T^{\gamma} + 0.000028 (p_T^{\gamma})^2$
	I_{γ}	$< 2.176 + 0.0043 p_T^{\gamma}$
	$I_{\mathrm{CH}}^{\mathrm{max}}$	$< 1.146*$
	H/E	< 0.0260
	hasPixelSeed	False
non-collision veto	$\sigma_{i\eta i\eta}$	> 0.001
	$\sigma_{i\phi i\phi}$	> 0.001
	E^{MIP}	< 4.9 GeV
	$\lvert t_seed\rvert$	< 3 ns

coming from QCD is large since the cross section for QCD production is large. But this background is very difficult to simulate using MC techniques since the occurrence rate is low and there is large uncertainty related to parton fragmentation. Hence, a data-driven approach is used which is described below.
A sample of fake photons are selected using a selection similar to that used for candidate events and a fake ratio is applied to obtain a normalized estimate of the jet faking photon background. The ratio is defined as the number of data events estimated as coming from jets but passing the photon selection criteria used in candidate selection, over the number of data events containing a jet that can give rise to a fake photon object but fail loose photon selection criteria.

Events are selected from a control sample with $p_T^{miss} < 30$ GeV, which is dominated by QCD multi-jet events and well separated from the signal region. The numerator of the fake ratio is the number of *fake* photon events in data that contain a reconstructed photon object satisfying the the medium photon ID criteria used in candidate selection. The denominator is the number of events in data that contain a reconstructed photon object failing loose photon ID criteria, but still passing a very loose selection. For both the numerator and denominator the photon ID criteria includes selections to mitigate the effects of non-collision backgrounds and beam halo effects. Events in both the numerator and denominator are required to pass the same triggers and the same set of p_T^{miss}filters. The photon selection requirements are summarized in Tables 5.3 and 5.4.

The control sample in which the fake ratio is measured has a considerable fraction of *real* isolated photons from inclusive QCD direct photon production processes. This contribution is estimated and the numerator of the raw fake ratio is corrected to reflect

Table 5.4: Requirements for reconstructed photon objects passing the denominator selections. Events must fail at least one of the loose photon ID requirements but pass a very loose photon ID selection. Each of the bounds for the very loose selection is 5 times the corresponding bound in the loose selection, or one-fifth the photon p_T, whichever is smaller.

Category		Pass all
fiducial	p_T^γ	> 175 GeV
	$\lvert\eta^\gamma\rvert$	< 1.4442
photon ID	I_{NH}	$< \mathrm{Min}(0.2p_T^\gamma, 5 \times [10.910 + 0.0148p_T^\gamma + 0.000028(p_T^\gamma)^2])$
	I_γ	$< \mathrm{Min}(0.2p_T^\gamma, 5 \times [3.630 + 0.0053p_T^\gamma])$
	$I_{\mathrm{CH}}^{\mathrm{max}}$	$< \mathrm{Min}(0.2p_T^\gamma, 5 \times 3.32)$
	H/E	< 0.05
	hasPixelSeed	False
non-collision veto	$\sigma_{i\eta i\eta}$	> 0.001
	$\sigma_{i\phi i\phi}$	> 0.001
	E^{MIP}	< 4.9 GeV
	t_seed	< 3 ns
		Fail exactly one
photon ID	I_{NH}	$< 10.910 + 0.0148p_T^\gamma + 0.000028(p_T^\gamma)^2$
	I_γ	$< 3.630 + 0.0053p_T^\gamma$
	$I_{\mathrm{CH}}^{\mathrm{max}}$	< 3.32

only the *fake* component. Photon $\sigma_{i\eta i\eta}$ templates were used, one for real and one for fakes, to determine the fraction of true photons using the fraction fitting facility in $ROOFIT$. The real photon templates came from $\gamma+$jets Monte Carlo, with events chosen according to the the numerator selection. The fake templates are taken from data by choosing events within a side-band of $I_{\mathrm{CH}}^{\mathrm{max}}$ defined as $8 < I_{\mathrm{CH}}^{\mathrm{max}} < 14$GeV. This QCD side band is chosen such that the real photon contamination in the fake template is small. The side band template is further refined by subtracting the expected distribution of real photon events estimated using $\gamma + jet$ Monte Carlo, where events are selected according to the same QCD side band criteria, but with the additional restriction that the reconstructed photon in the event matches a generated final state photon within $\Delta R < 0.1$.

Figures 5.6, 5.7, and **??** show the results of the template fitting in various p_T^γ bins. The estimated fake fractions are calculated within $\sigma_{i\eta i\eta} < 0.0104$ in oreder to match the photon candidate selection criteria.

Figure 5.8 shows the final (corrected) QCD fake ratio. The jet faking photon estimate in the signal and control regions are made by first selecting events using identical criteria as for candidate events, but replacing the photon selection criteria with those for photons from the denominator sample. The number of events selected in each p_T^γ bin is then

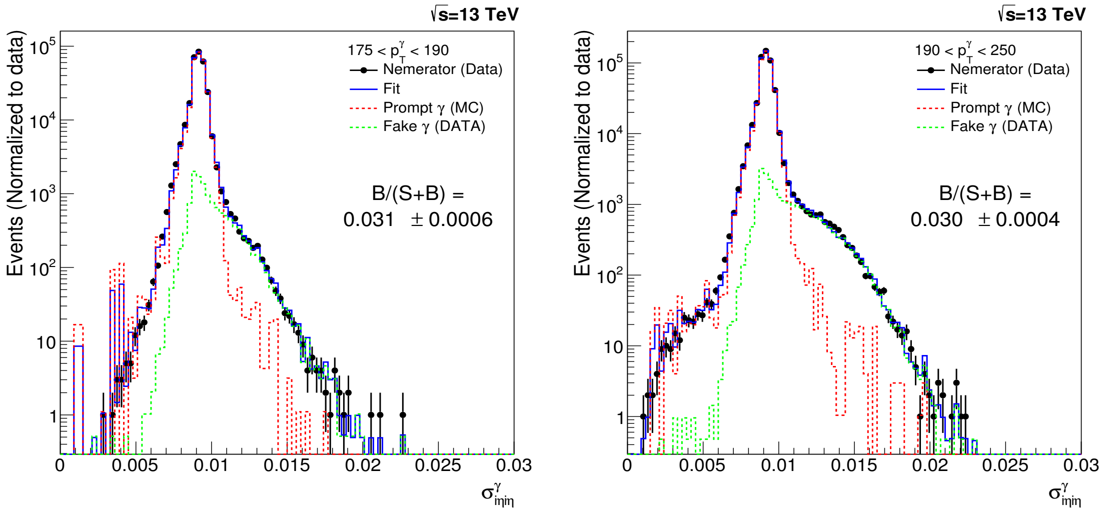

(a) p_T Bin 175-190 (b) p_T Bin 190-250

Figure 5.6: Distributions of photon $\sigma_{i\eta i\eta}$ in data, and fits to real and fake photon components, in p_T^γ bins 175-190 GeV and 190-250 GeV.

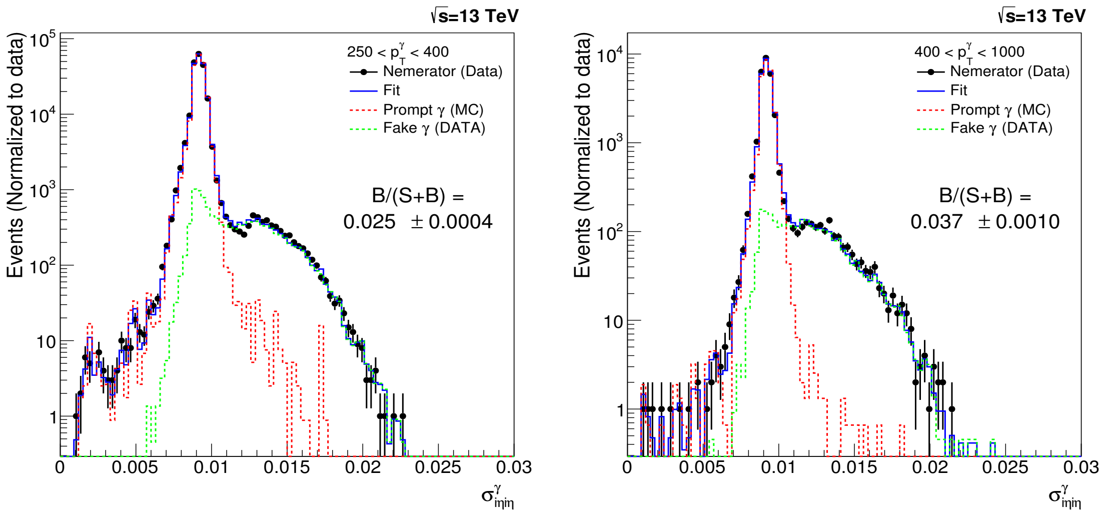

(a) p_T Bin 250-400 (b) p_T Bin 400-1000

Figure 5.7: Distributions of photon $\sigma_{i\eta i\eta}$ in data, and fits to real and fake photon components, in p_T^γ bins 250-400 GeV and 400-1000 GeV.

multiplied by the fake ratio in the appropriate p_T^γ bin to obtain the final jet faking photon distribution as a function of p_T^γ.

The error on the QCD fake ratio is calculated by taking the largest of the shifts in each p_T^γ bin arising from the following sources:

- Varying the upper boundary of the QCD sideband by 2 GeV above or below 14 GeV, to become 12 GeV and 16 GeV, respectively.

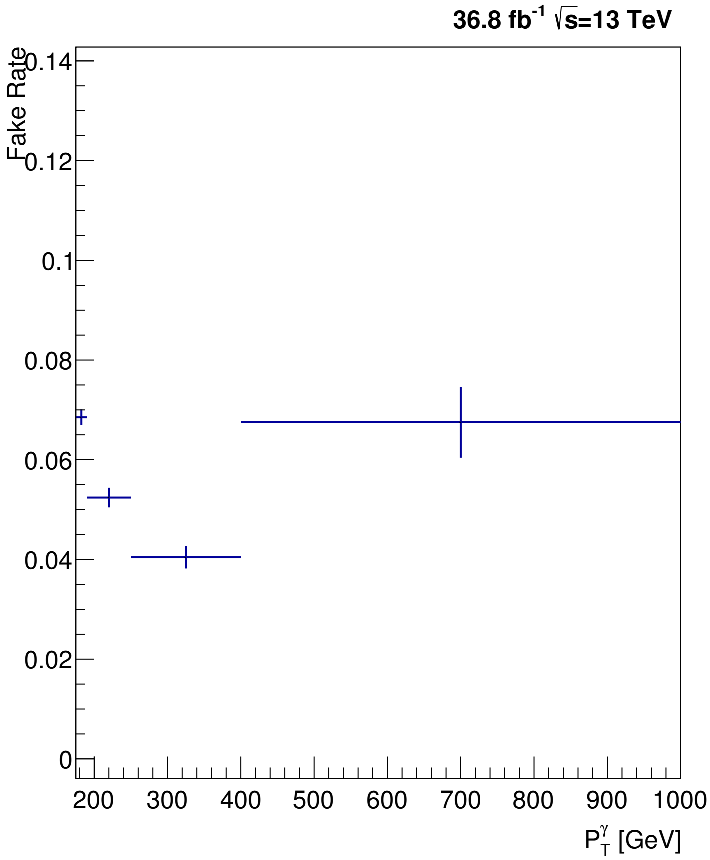

Figure 5.8: The QCD fake ratio as a function of p_T^γ.

- Varying the MET cut for the control region selection by multiplying and dividing 30 GeV by 5/6, to become 25 GeV and 36 GeV, respectively.
- Changing the bin width of the $\sigma_{i\eta i\eta}$ templates to 0.5 and 2.0 times the nominal bin width.
- Shifting the $\sigma_{i\eta i\eta}$ templates left and right within the uncertainties of a scale factor that corrects the $\sigma_{i\eta i\eta}$ distribution in MC to match that of data.
- Varying the numerator and denominator up and down by their statistical error, added in quadrature with the error assigned to the numerator template fit.

Each type of variation shifts the fake ratio by a similar amount, up to roughly 2 percent in each bin of p_T^{γ}, though the statistical plus template fit variation dominates the last bin with a 10 percent shift arising from the relatively low statistics in that bin.

5.5.6 Non-collision background

5.5.6.1 Composition

Non-collision background arise from multiple sources. These events appear as an isolated high-pT photon with very little other activity in the event because coincidence with hard scatterings is rare, and hence give rise to large p_T^{miss}pointing away from the photon candidate. The known sources are:

- Beam halo
  Bremsstrahlung by the beam halo muon (a muon travelling along the beam produced from beam interaction with residual gasses and beam pipe) in or near the ECAL volume will generate an actual physical EM shower in the ECAL crystals. Such energy deposit is rarely expected to be large, but it is found that their occurance during the 2016 run was substantial.

- Anomalous signals from ECAL barrel (Spikes)
  A large signal pulse can be generated in the ECAL barrel avalanche photodiode (APD) when neutrons interact at its photocathode. These pulses are commonly called ECAL spikes and can mimic signal from a real scintillation event thus appearing as up to several TeV of energy deposit mimicking an event with only a high $\mathrm{p_T}$ photon and a large p_T^{miss}.

5.5.6.2 Beam halo background estimation

Beam halo photon candidates have several characteristic features that are exploited to estimate their contribution in the signal region and reject them.

- Energy deposition distribution
  A beam halo muon usually gives hits in the endcap muon system that are coincident with the ECAL hits. The ECAL hits form a "trail" of low-energy clusters along the muon trajectory. There is a beam halo filter, which is also a part of the "MET filters" described in Sec. 5.3.2 which is triggered by these signatures.

- Azimuthal angle
  Beam halo muons are observed to arrive at CMS anisotropically in ϕ with most of observed around $\phi \sim 0, \pi$, ie, in the horizontal plane.

- ECAL hit time
  Tthe clock offset of ECAL readout channels are tuned to register EM showers from prompt collision at $t \sim 0$, but the EM showers caused by a beam halo muon produces ECAL hits with slightly earlier (more negative) t.

The first property is utilized in the analysis to construct a beam halo control sample by inverting one or more of the identification requirements. With this control sample, the number of beam halo background events and their distributions are estimated through a direct fit to the observed data during the signal extraction process, described in Sec. 5.6.

Figure 5.9 shows the ϕ distribution of the halo showers which are obtained from the single photon data set after requiring $E_{\mathrm{T}}^{\gamma} > 175\mathrm{GeV}$ and $p_T^{miss} > 170\mathrm{GeV}$. The halo showers are defined as photon objects that fail the MIP total energy cut in events where beam halo MET filter is applied. The distribution folded in ϕ to make the peaking behavior prominent.

ECAL hit time distribution of the beam halo is also utilized in the study of ECAL spike background described below.

5.5.6.3 ECAL barrel spikes background estimation

Neutrons and other hadronic particles (collectively refered to as neutral hadrons) interact with the photocathode material of the ECAL avalanche photo diodes (APD). Nuclear fission at the APD surface then causes a large electron avalanche, which is mistaken as a large photon deposit in the ECAL crystal. Evidences supporting this hypothesis is documented in Ref. [33].

The ECAL hits due to spikes have distinct features. The ratio of reconstructed energy deposit between the ECAL channel with the spike and the surrounding channels is large

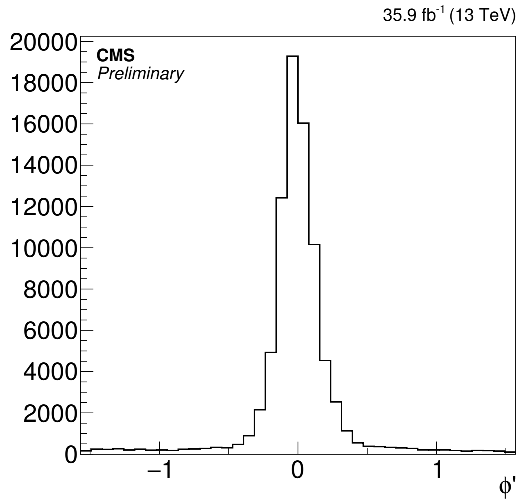

Figure 5.9: Folded ϕ' distribution of the halo sample [32].

since spikes affect a single APD (or a pair of neighboring APDs causing double spikes). When a cluster is formed around a crystal with a spike, this feature leads to a very small value of the shower shape variable such as $\sigma_{i\eta i\eta}$ and $\sigma_{i\phi i\phi}$. For spikes there is also a high probability of the reconstructed pulse peak time to be out of the prompt time window of ± 3 ns. This feature originates from the pulse shape of spikes that are different from pulses due to scintillation light in the crystals. Since the spike pulse is the response of the ECAL multi-gain preamplifier to a delta function input, compared to the response to scintillation light it has a shorter rise time and faster decay . This faster rise time of the pulse is interpreted in the reconstruction as an earlier (negative time) signal. Additionally, since spikes can be caused by slow neutrons that bounce in the detector for some time before hitting the APD photocathode, spike signal can also appear with random timing.

There are rare cases where two neighboring APDs exhibit anomalous signal called the double spikes which is less well understood but still causes shower shapes narrower than those of physical EM shower and also the sharp pulses. No distinctions between single and double spikes are made in the analysis.

Most of the ECAL spikes are filtered out by utilizing the features above.

In spite of many levels of spike cleaning, some spike-seeded clusters can still appear as a photon candidate in the signal region of this analysis. Such clusters do not have shower shape as narrow as a typical spike cluster since these spikes are likely to occurr in a real energy deposit in ECAL, such as those due to pileup jets, and have the reconstructed seed time within the prompt window. We estimate these spikes called embedded spikes.

Figure 5.10 shows the timing distribution of barrel photon objects with $\mathrm{p_T} > 175\mathrm{GeV}$ and $\sigma_{i\eta i\eta} < 0.0104$ in events with $p_T^{miss} > 170\mathrm{GeV}$. The photon objects are obtained from a special reconstruction sample, where no spike cleaning based on $\tau_{d}enseandc$seedis applied during offline clustering.

The distribution is fit with three templates: halo, and spikes, and prompt. The halo template is formed by photons with MIP total energy > 4.9GeV. The spike template comes by requiring the shower shape variables ($\sigma_{i\eta i\eta}$ or $\sigma_{i\phi i\phi}$) to have unphysically small values, ie, < 0.001. The prompt template, representing the timing distribution of EM objects emerging from the p-p collisions, comes from Z candidate events in where the photon candidates are required to have a pixel seed match. The three templates and their cross checks are shown in Fig. 5.11.

Due to the modified selection criteria for ECAL hits, the special reconstruction sample has a different event description from the standard reconstruction sample and the prompt and halo yields obtained from the three-component template fit do not correspond to the actual yields in the standard reconstruction signal region. Instead the in-time component of the spike contribution in this fit gives an estimate of the spike contribution in the signal region.

To estimate the systematic uncertainty in the method, the alternative spike templates are formed by varying the shower shape variables ($\sigma_{i\eta i\eta}$ or $\sigma_{i\phi i\phi}$) from < 0.001 to < 0.002 in steps of 0.0001.

5.6 Signal extraction

Potential signal contribution is extracted from the data by simultaneously fitting the E_{T}^{γ} distributions in the signal region and various control regions. Uncertainties on various quantities are represented by nuisance parameters in the fit. Predictions for $Z(\nu\nu) + \gamma$, $W(l\nu) + \gamma$, and the beam halo backgrounds are varied in the fit.

Free parameters of the fit are the yield of $Z(\nu\nu)+\gamma$ background in each bin of the signal region and the overall normalization of the beam halo background. Bin-by-bin yields of $W(l\nu) + \gamma$ and $Z(l\bar{l}) + \gamma$ samples in all regions are related to the yield of $Z(\nu\nu) + \gamma$ through the MC prediction, with their ratios (”transfer factors”) allowed to shift within the theoretical uncertainties. To constrain the beam halo normalization, the signal region is split into two parts by $|\phi|$. Parts $|\phi| < 0.5$ and $|\phi| > 0.5$ are respectively called the horizontal and vertical signal regions.

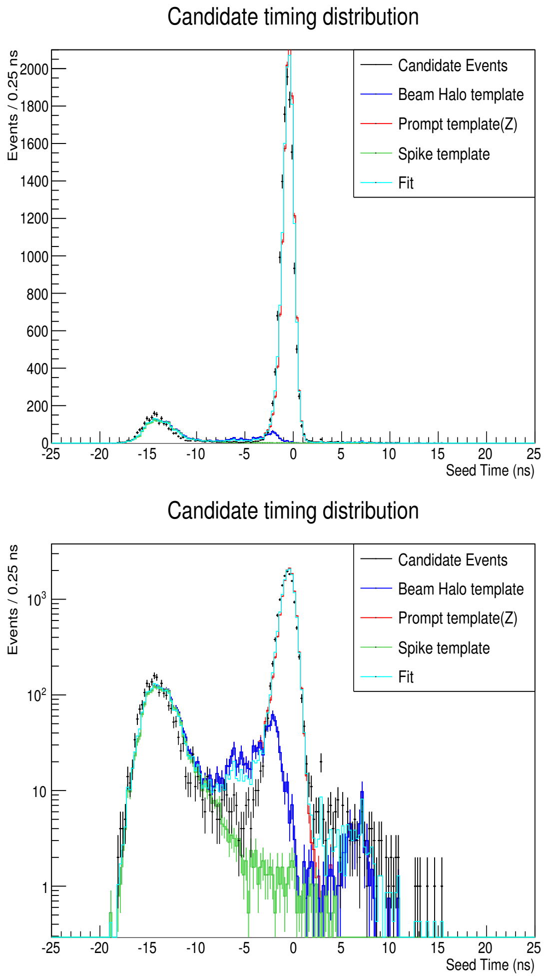

Figure 5.10: Timing distribution of candidate-like photons in events with $p_T^{miss} > 170\text{GeV}$ obtained by full re-reconstruction of 2016 data in log and linear scale. The three templates used in the fit are in Fig. 5.11.

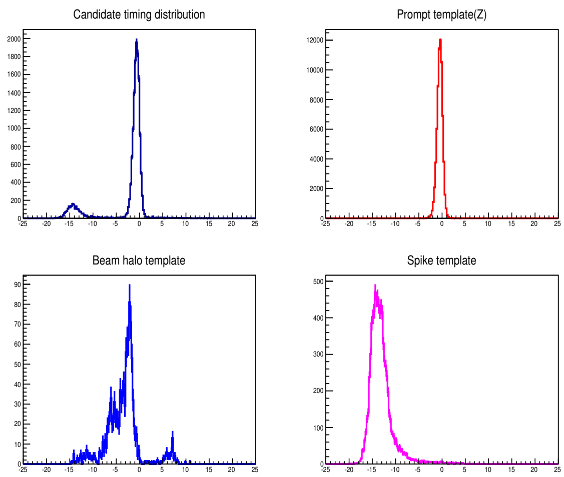

Figure 5.11: Timing distribution templates for halo, prompt, and spike candidates.

The likelihood that is maximized in the fit is

$$\begin{aligned}\mathcal{L} = \prod_i \Bigg[& \prod_{K=\text{horiz.,vert.}} \mathcal{P}\left(d_{K,i} \middle| \left(1 + f^{W\gamma}_{Z\gamma,i}(\theta)\right) C_K N^{Z\gamma}_i + h n^{\text{halo}}_{K,i}(\theta) + b_{K,i}(\theta)\right) \\ & \cdot \prod_{K=e\gamma,\mu\gamma} \mathcal{P}\left(d_{K,i} | R^{W\gamma}_{K,i}(\theta) f^{W\gamma}_{Z\gamma,i}(\theta) N^{Z\gamma}_i + b_{K,i}(\theta)\right) \\ & \cdot \prod_{K=ee\gamma,\mu\mu\gamma} \mathcal{P}\left(d_{K,i} | R^{Z\gamma}_{K,i}(\theta) N^{Z\gamma}_i + b_{K,i}(\theta)\right)\Bigg] \\ \cdot & \prod_j \mathcal{N}(\theta_j),\end{aligned} \tag{5.3}$$

where the symbols represent

- i: E_{T}^{γ} bin index
- $\mathcal{P}$: Poisson distribution
- $\mathcal{N}$: Normal distribution
- $d_{K,i}$: observed number of events in bin i of region K
- $N^{Z\gamma}_i$: yield of $Z(\nu\nu) + \gamma$ sample in bin i of the combined signal region
- h: normalization of the beam halo background
- $n^{\text{halo}}_{K,i}$: unit-normalized beam halo prediction in bin i of the signal region K
- $C_{\text{horiz.}} = 1/\pi$, $C_{\text{vert.}} = (\pi - 1)/\pi$: constants
- $R^{V\gamma}_{K,i}(V \in W, Z)$: MC prediction of the ratio of yields in bin i between the $W(l\nu)+\gamma$ ($Z(l\bar{l}) + \gamma$) sample in the $\ell\gamma$ ($\ell\ell\gamma$) control region K and the combined signal region
- $f^{W\gamma}_{Z\gamma,i}$: MC-predicted ratio of yields from $W(l\nu) + \gamma$ background and $Z(\nu\nu) + \gamma$ background in the signal region
- $b_{X,i}$: predicted contribution from other background sources in the region X
- θ_j: nuisance parameters corresponding to uncertainty j.

Each nuisance parameter shifts the respective quantities in the likelihood multiplicatively as $\exp(\theta_j/\Theta_j)$, where $\Theta^j_{K,i}$ is the estimated size of uncertainty represented by the parameter θ_j in bin i of region K. Most of the nuisance parameters affect multiple E_{T}^{γ} bins and multiple regions.

Table 5.5 summarizes the nuisance parameters and how they are correlated across the bins and regions.

Table 5.5: Nuisance parameters in the fit. In the table, S indicates that there is a single nuisance parameter that controls the values of the given factor for all E_{T}^{γ} bins and all regions. In contrast, B indicates that the variation is bin-by-bin, ie, there is a nuisance parameter for each bin of each region affected by the uncertainty.

Nuisance parameter	$R^{W\gamma}$	$R^{Z\gamma}$	$f_{Z\gamma}^{W\gamma}$	n^{halo}	b
$V\gamma$ EW NLO uncertainty	-	-	S	-	-
$V\gamma$ PDF uncertainty	-	-	S	-	-
$V\gamma$ μ_R and μ_F uncertainty	-	-	S	-	-
Beam halo shape uncertainties	-	-	-	S	-
Object ID efficiency uncertainties	-	-	-	-	S
Electron and hadron misID rate uncertainties	-	-	-	-	S
Energy scale uncertainties	-	-	-	-	S
$\int \mathcal{L}dt$ uncertainties	-	-	-	-	S
Minor SM PDF uncertainty	-	-	-	-	S
Minor SM μ_R and μ_F uncertainty	-	-	-	-	S
Spike estimate uncertainties	-	-	-	-	S
MC and control sample statistical uncertainties	B	B	B	B	B

5.7 Results

5.7.1 Pre and post-fit distributions

Figures 5.12, Figure 5.13 and Figure 5.14 show the transfer factors connecting the signal and control regions. These factors are assigned log-normal probability distributions around their nominal value, with the uncertainties translated to the width of the distributions. There are 3 systematic uncertainties which are considered on the $f_{W\gamma}^{Z\gamma}$ transfer factor ie. PDF, factoziation/renormalization scale and NLO EWK unceratinty. PDF and μ_R and μ_F uncertainty are considered as fully correlated amongst W and Z and across all the bins, whreas the EW NLO uncertainty is considered as un-corelated amongst W and Z.

For increasing p_T^{γ} the Z in Z$(\rightarrow l\bar{l}) + \gamma$ events emerge with lower rapidity. As a result the charged leptons coming out of it are more likely to fall with inner tracker acceptance which in turn increases the dilepton selection efficiency. Z$(\rightarrow \nu\bar{\nu}) + \gamma$ event selection efficiency on the other hand remains unaffected. This causes a distinctive drop in $R_{ll\gamma}^{Z\gamma}$ with increasing p_T^{γ} as shown in Figure 5.13. Similar arguements can explain the drop in $R_{l\gamma}^{W\gamma}$.

The ratio $f_{W\gamma}^{Z\gamma}$ on the other hand rises (rather than falls) with increasing p_T^{γ} since W$(\rightarrow l\nu) + \gamma$ events have a lower (rather than higher) signal region selection efficiency if the charged lepton falls within the tracker acceptance.

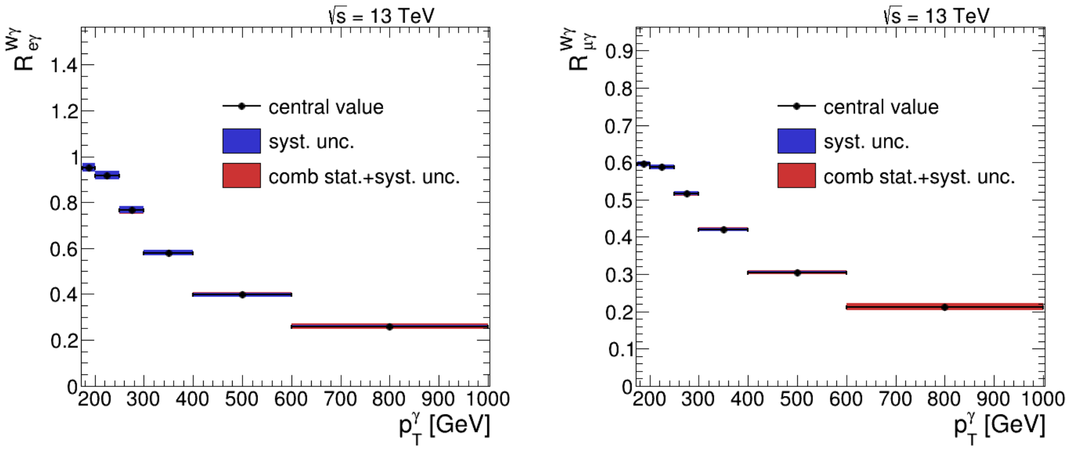

Figure 5.12: Transfer factors $R^{W\gamma}_{e\gamma}$ (left) and $R^{W\gamma}_{\mu\gamma}$ (right).

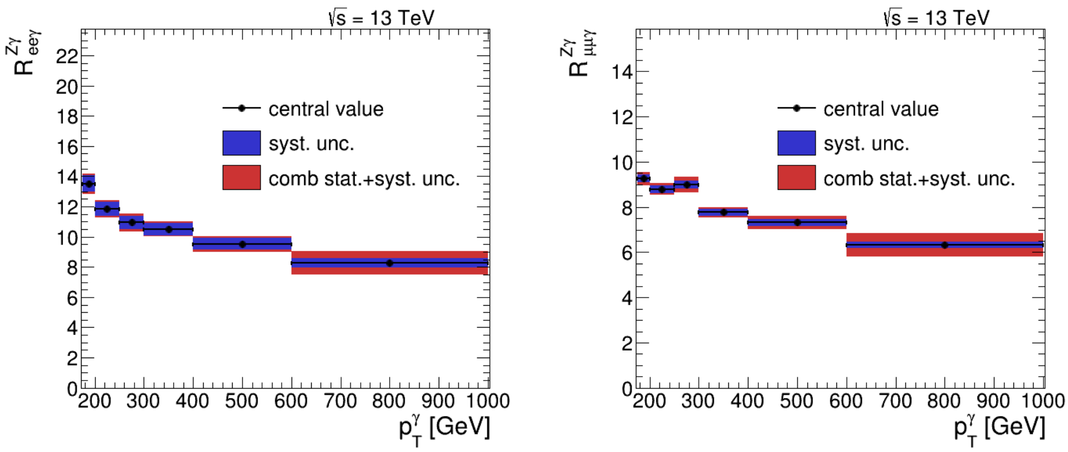

Figure 5.13: Transfer factors $R^{Z\gamma}_{ee\gamma}$ (left) and $R^{Z\gamma}_{\mu\mu\gamma}$ (right).

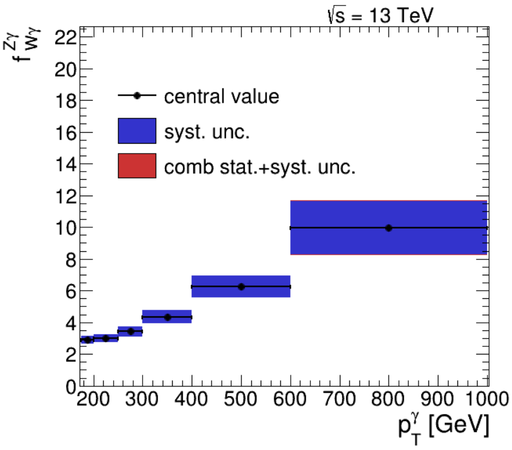

Figure 5.14: Transfer factor $f^{Z\gamma}_{W\gamma}$.

Figure 5.15 shows the pre-fit and post-fit plots in the CR's.

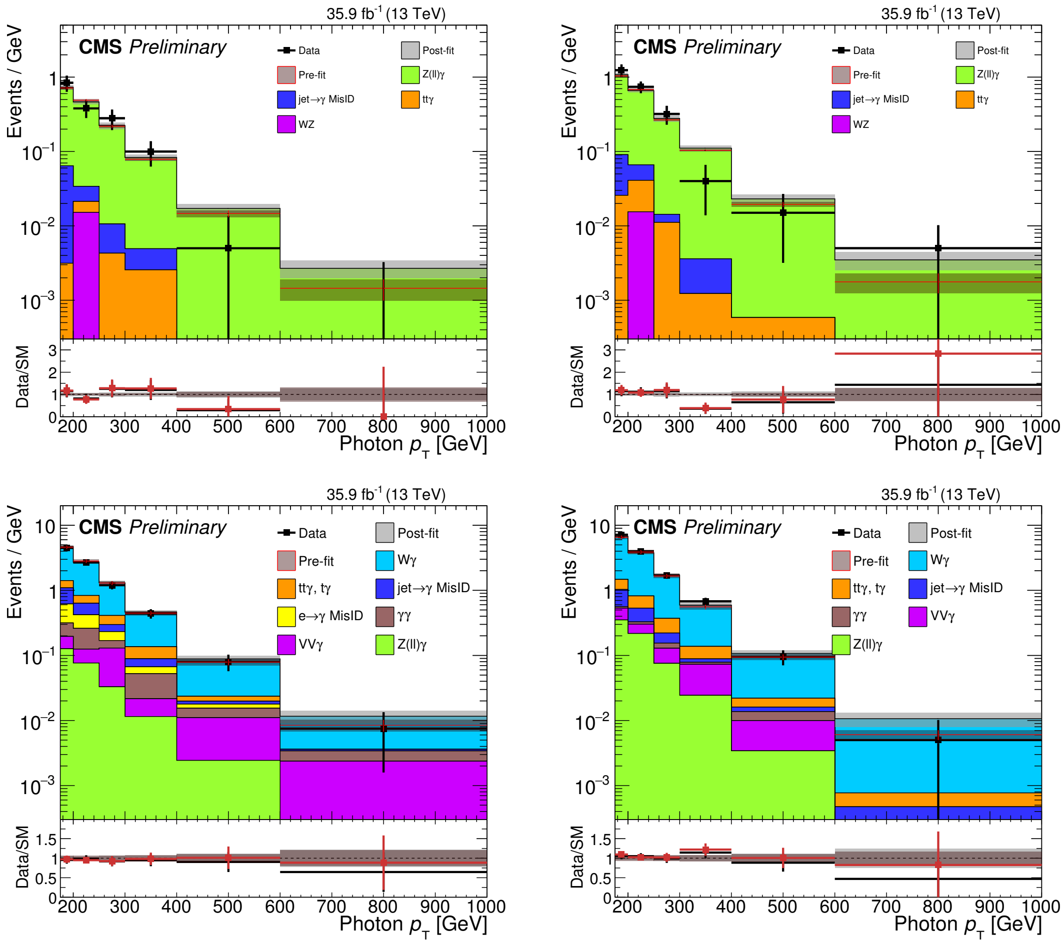

Figure 5.15: E_{T}^{γ} post-fit in the 4 control regions with $ee\gamma$ (top left), $\mu\mu\gamma$ (top right), $e\gamma$ (bottom left), $\mu\gamma$ (bottom right) .

Figure 5.16 shows the pre and post-fit background distributions in the signal region in low and high phi regions separately.

5.7.1.1 Limits

The likelihood in Equation 5.3 can be used to construct the test statistic based on one-sided profile likelihood ratio to calculate the CL_s value [34]. The hypothetical signal strength $\mu = \sigma/\sigma_{\mathrm{theory}}$ at which $\mathrm{CL}_s = 0.05$ is the 95% confidence level upper limit on the signal strength, denoted as μ_{95}.

Figure 5.17 shows μ_{95} for the vector and axial-vector mediator scenarios, in the M_{med}–m_{DM} plane using the NLO DM samples. The solid red (lighter) curves are the expected contours of $\mu_{95} = 1$ (exclusion contour). The region with $\mu_{95} < 1$ is excluded under nominal σ_{theory} hypotheses. The uncertainty in the expected upper limit includes the

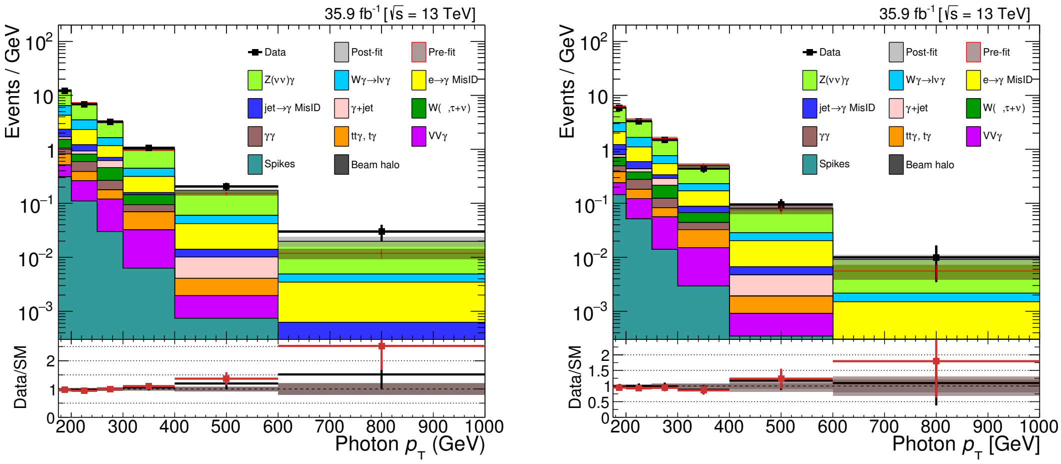

Figure 5.16: E_T^γ post-fit in the high phi (left) and low phi(right) signal region.

experimental uncertainties. For the simplified DM leading order models considered, mediator masses of up to 950GeVare excluded for small m_{DM} values.

Figure 5.18 shows the upper limit and the theoretically calculated ADD graviton production cross section for $n = 3$ extra dimensions, as a function of M_D. Lower limits on $M_D$for various values of n extra dimensions are summarized in Table 5.6, and in Fig. 5.19 are compared to CMS results. Because the graviton production cross section scales as E^n/M_D^{n+2} [2], where E is the typical energy of the hard scattering, M_D can be an increasing or decreasing function of n for a fixed cross section value, approaching E as $n \to \infty$. Values of M_D up to 2.90TeVfor $n = 6$ are excluded by the current analysis.

Table 5.6: The 95% CL observed and expected lower limits on M_D as a function of n, the number of ADD extra dimensions.

n	Obs. limit (TeV)	Exp. limit (TeV)
3	2.85	3.32
4	2.86	3.29
5	2.88	3.28
6	2.90	3.28

5.8 Summary

Final states with a high transverse momentum photon and large missing transverse momentum produced in proton-proton collisions at $\sqrt{s}$ =13 TeV have been analyzed to look for new physics with a dataset corresponding to $35.9fb^{-1}$ of integrated luminosity. There

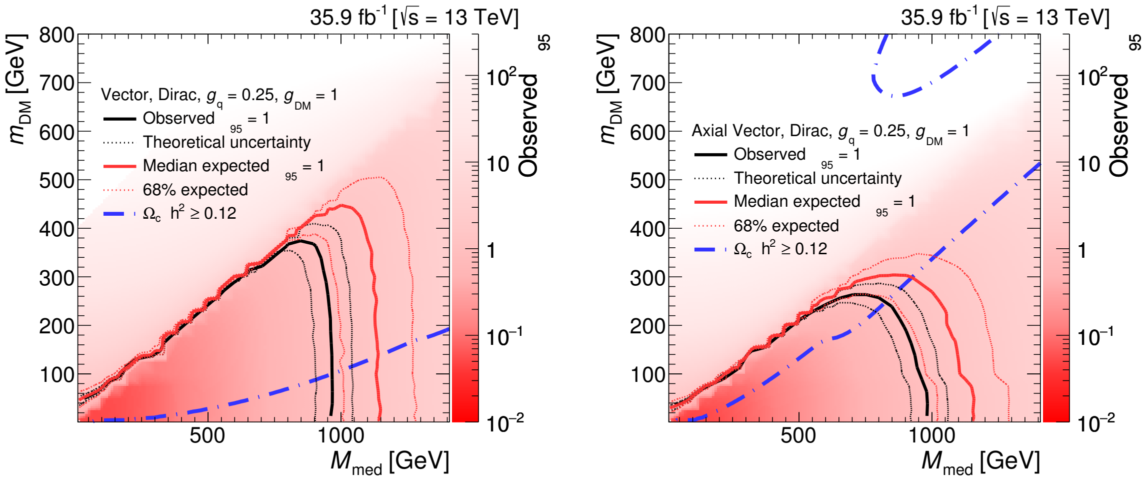

Figure 5.17: The ratio of 95% CL cross section upper limits to theoretical cross section (μ_{95}), for DM simplified models with vector (left) and axial-vector (right) mediators, assuming $g_q = 0.25$ and $g_{DM} = 1$. Expected $\mu_{95} = 1$ contours are overlaid. The region below the observed contour is excluded. The blue dashed lines correspond to where the DM simplified model parameters match the relic density observed by the Planck experiment.

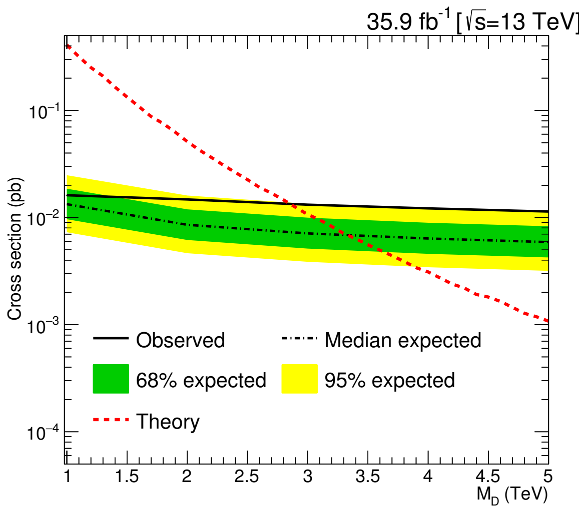

Figure 5.18: The 95% CL upper limits on the ADD graviton production cross section, as a function of M_D for $n = 3$ extra dimensions.

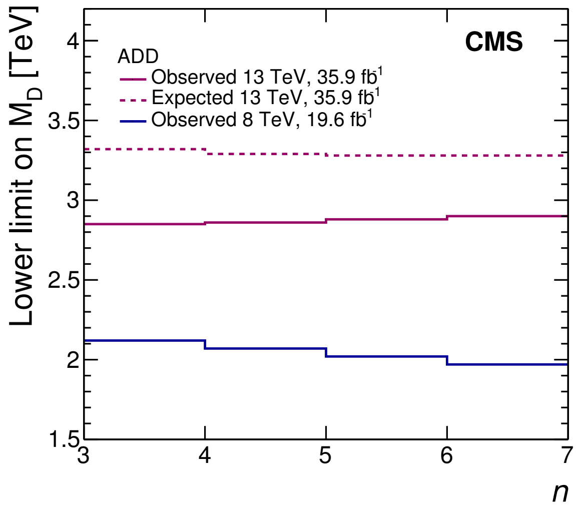

Figure 5.19: Lower limit on M_D as a function of n, the number of ADD extra dimensions.

was no observation of any deviation from Standard Model expectations. For DM simplified models the observed (expected) lower limit on the mediator mass is 950 (1150) GeV for dark matter mass around 1 GeV. For ADD model of large extra dimensions, for number of extra dimensions between 3 and 6, effective Planck scale $M_D$up to 2.85 to 2.90 TeV are excluded. There has been an inprovement in the sensitivity of this analysis (stronger upper limits on the expected cross section) by around 70% compared to previous CMS results [35] by employing the simultaneous fit to multiple signal and control regions and also using a larger datasize.

Chapter 6

Simulation study to distinguish prompt photon from π^0 and beam halo in a granular calorimeter using deep networks

6.1 Introduction

The ability to distinguish prompt photons (photons coming from hard scattering) from photons coming from neutral meson (π^0, η) decays or other anomalous sources like bremsstrahlung photon coming from beam halo muon is critical as discussed in section 5. Present available techniques use a combination of shower shape variables which try to capture the difference in spatial pattern between them. Supervised learning algorithms for classification like Artificial Neural Network (ANN) or boosted decision trees (BDTs) with the shower shape variables as input have had some success([36] [37]). With the emergence of new image recognition networks it is possible to use them for our problem and it is motivated by instances of image network use in High Energy Physics in neutrino classification, jet classification etc.

In the following analysis Convolutional Neural Network (CNN) is used where the machine learns to construct many high level variables with just the energy deposit per crystal information of an electromagnetic calorimeter. Each of the filters in the CNN represents such a high level variable. Thus a CNN extracts maximum amount of information from the raw output of the electromagnetic calorimeter, which leads to better performance in discriminating between classes. The data is the set of images directly from the detector and the CNN is run on it without providing any high level physics information. Performance of CNN is compared with a Multi Layer Perceptron (MLP) with physics variables (representative of shower shape) to evaluate the ability of the deep learning algorithms to identify features from the data without much human intervention.

6.2 Object Identification

The three types of objects which are of interest in this analysis have already been discussed in sections 3 5. Here the energy deposit pattern of these objects have been shown which form the input images and also give an idea of their distinct spatial ebergy deposit characteristics.

The typical map energy deposit of different classes of photons are shown in Fig.6.1

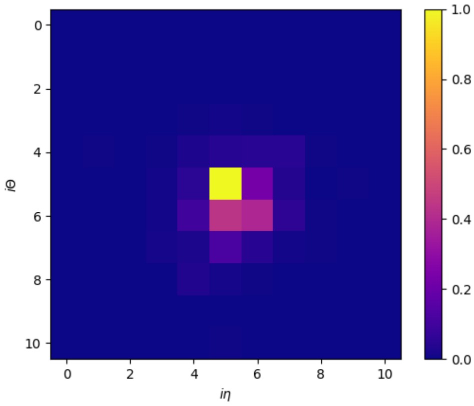

(a) (a)

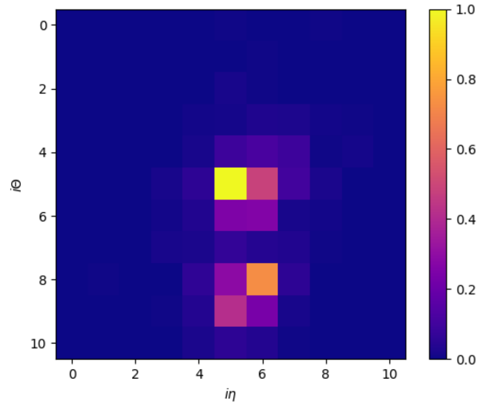

(b) (b)

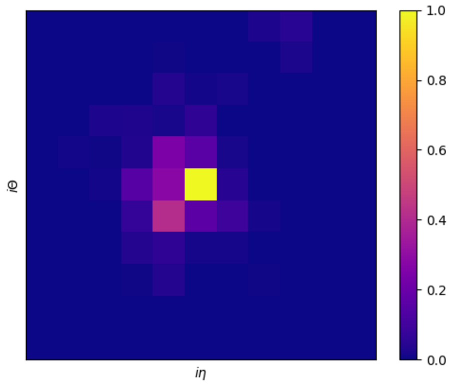

(c) (c)

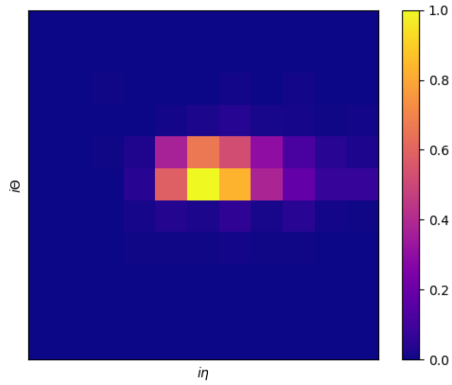

(d) (d)

Figure 6.1: Image representation of the energy deposit pattern in the Ecal of (a) a prompt photon, (b) a converted photon, (c) a π^0, (d) a beam halo photon , normalized with the energy of the seed crystal in η, ϕ coordinates. The colors represent the relative magnitude of energy deposited in a crystal.

The energy deposits of prompt photons, and photons from π^0 and beamhalo in the ECAL Figure 6.2.

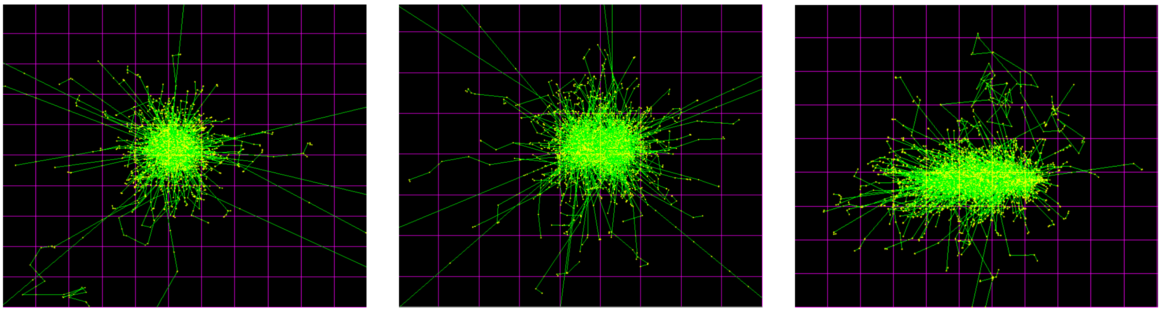

(a) (a) (b) (b) (c) (c)

Figure 6.2: Showers from a 10 GeV (a) prompt photon, (b) π^0 and (c) beam halo photon. Photons were shot perpendicular to the surface of the calorimeter For (a) and (b) and photon was shot from the side for (c).

6.3 Simulation

A model detector has been constructed [38] using `GEANT4` [39] resembling CMS (according to technical design report (TDR) [40]) comprising of calorimeter and tracker. The calorimeter which includes just the barrel region ($-1.479 < \eta < 1.479$) is made of parameterized volumes of part of a sphere which is arranged as an array of $PbWO_4$ crystals placed in a cylindrical arrangement. Each of the volumes has 0.0174 coverage in η, 1deg coverage in azimuthal angle (ϕ) and 22 cm radial length. The crystals have dimensions 2.2 cm $\times$ 2.3 cm in the front face and vary between 2.4 cm $\times$ 2.4 cm to 2.6 cm $\times$ 2.7 cm in the back face. All of the values are within 5% of the ECAL crystal sizes mentioned in the TDR. The tracker has been implemented in a very simplified way as 13 concentric cylinders of varying thickness of silicon. The first three layers have a thickness of 285μm. Then there are four layers of 320 μm thickness and six more layers which are 500 μm Si thick. In order to have a material budget similar to that of the CMS tracker in $-0.8 \leq \eta \leq 0.8$ additional material has been added . There is an uniform 4T magnetic field along the positive Z-axis. Figure 6.3 shows a cross-sectional view of the geometry.
The simulation also includes a tag which filters out photons converting anywhere inside the tracking volume. For simulating physics process the standard physics list FTFP-BERT has been used [41] to keep the simulation as close to the general purpose detectors like CMS and ATLAS as possible . These processes include pair production, bremsstrahlung and photo-electric effect for photons along with Compton scattering for e^-. The particles are assumed to deposit their entire energy at a point if they cannot travel a distance of 1

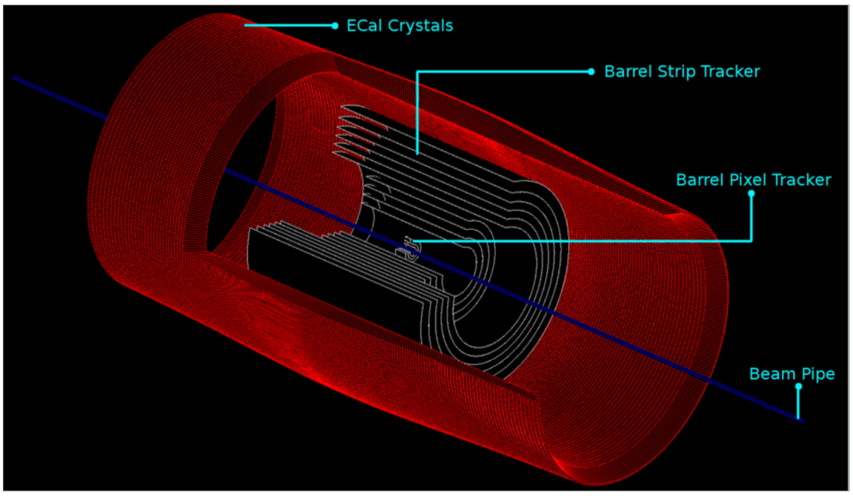

Figure 6.3: The detector simulated in `GEANT4`.

mm further from the point.

6.4 Analysis and Results

The information from the ECAL has been represented as a 2D image in the $\eta \times \phi$ space as n×n matrix of cells around a local maximum in energy deposit (which is called seed crystal). The value of n is 11 or 25 depending on the problem described in the following sections. The cells represent calorimeter crystals and the values of the cells represent the energy contained in them. The values are normalized to the seed crystal energy. For each of the classification problems, three different network analyses have been performed:

- The shower shape variables constructed out of cell values are inputs to an MLP or DNN.
- The normalized cell values are inputs to an MLP or DNN.
- n×n matrix of normalized cell energies are inputs to a CNN.

The shape variables are constructed from intuition which utilizes the knowledge about the narrow lateral shower profile of an electromagnetic shower. They are designed after the standard shower shapes variables used in the CMS ECAL [42, 43] and other prior studies.

6.4.1 Network Architecture and Ranking

For implementing the networks used in the analysis the package `Keras` [44], with `Tensorflow` [45] as backend has been used. The different networks used are listed below:

Convolutional Neural Network (CNN): The CNN has been constructed with two convolutional layers with filters of size 3×3 and stride 1×1. The activation function called rectified linear unit (RELU) [46] acts on the outputs. L2 regularization is applied on the weights of these layers. This is followed by maxpooling layer of pool window size 2×2. It is followed by a fully connected layer with 64 nodes, with dropout regularization [**?**] of 30%. There is a final fully connected layer with the softmax activation function which gives a binary output. The CNN structure is shown in Figure 6.4.

Multi Layer Perceptron (MLP): For the photon-beam halo separation problem, a MLP is used which has one hidden layer with 32 nodes with RELU activation, followed by an output layer of 2 nodes with softmax activation. This simple network is seen to give optimal classification. Figure 6.5 shows the network architecture, where only one hidden layer is considered.

Deep Neural Network (DNN): For photon-π^0 separation problem, a MLP with two hidden layers is used since the problem is more difficult and a deeper network is found to perform better. The first layer has 64 nodes, the second layer has 32 nodes, both with RELU activation. This is followed by a dropout of 30%. The output layer has 2 nodes with softmax activation. The MLP used is shown in Figure 6.5. The loss function used is cross-entropy with the ADADELTA optimizer [47].
To evaluate the performance of each classifier Receiver Operating Characteristics (ROC) curve with signal efficiency vs. background rejection have been plotted. The area under the curve (AUC) of the ROC has also been used as a measure of the quality of the classification.

6.4.2 Datasets

Dataset for this study comprises of 51,000 images each of the signal (prompt photons) and background (non-prompt photons) classes. Images of dimensions 11×11 have been used for prompt photon - beam halo separation. For prompt photon - π^0 separation, images of dimensions 25×25 have been used to efficiently capture the conversion of photons. Out of the entire sample set, 80% has been used for training and 20% for testing. 30% of the training set has been used for validation. When the loss on the validation step did not decrease by a significant amount after a certain number of epochs training was stopped .

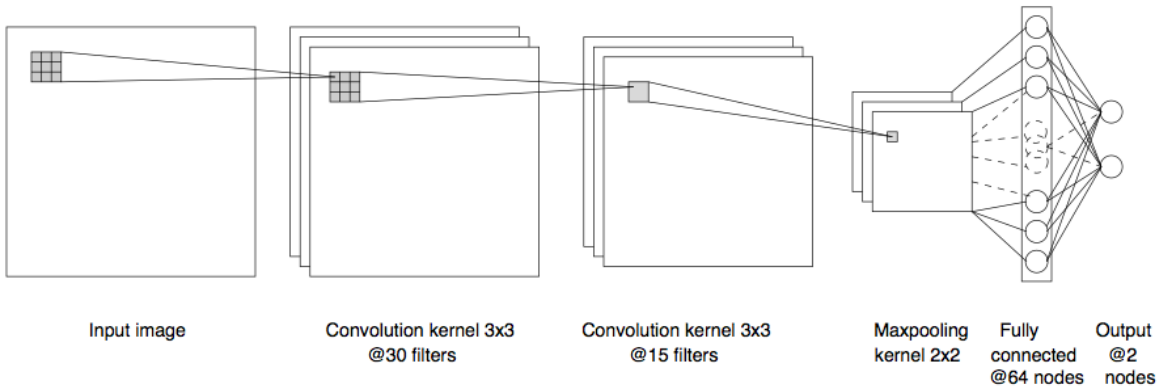

Figure 6.4: The CNN architecture. The input image size is 11×11 for beam halo rejection and 25×25 for π^0 rejection.

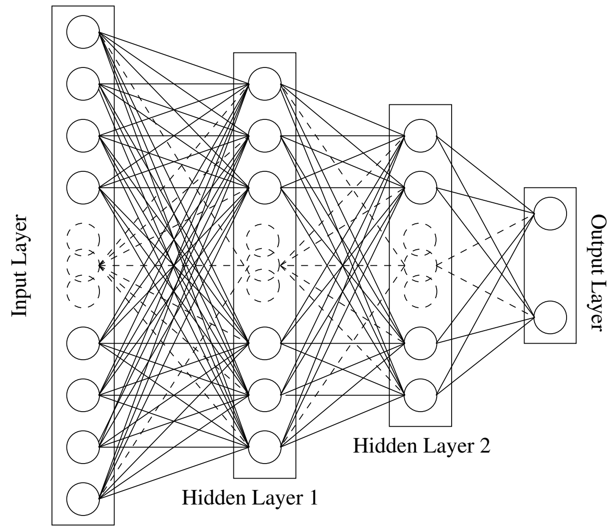

Figure 6.5: The network for π^0 separation (DNN) has two hidden layers with 64 and 32 nodes respectively with RELU activation. For the beam halo separation with MLP , the network has only one hidden layer of 64 nodes with RELU activation. The output layer is always acted on by softmax activation.

6.4.3 Beam halo - prompt photon separation

The setup mentioned above was used to generate samples of 10 GeV prompt photons and beam halo photons. These samples were first analyzed using shower shape variables which are sensitive to the differences in energy spread in the $\eta \times \phi$ space shown in Fig 6.1. These variables are:

$$s_9/s_{25}, \qquad \sigma_{i\eta i\eta}, \qquad \sigma_{i\phi i\phi}$$

where s_9/s_{25} is the ratio of energy deposited in a 3×3 matrix of crystals centered on the seed crystal to the total energy deposited in the 5×5 matrix around the seed crystal and

$$\sigma^2_{i\eta i\eta} = \frac{\Sigma_{i=1}^{5\times5} w_i (i\eta_i - i\eta_{seed})^2}{\Sigma_{i=1}^{5\times5} w_i}, \qquad w_i = \max\left(0, 4.7 + \ln\frac{E_i}{E_{5\times5}}\right) \tag{6.1}$$

where E_i and $i\eta_i$ are the energy and η index of the i^{th} crystal within the 5×5 cluster and $i\eta_{seed}$ is the η index of the seed crystal [42]. For ϕ we have,

$$\sigma^2_{i\phi i\phi} = \frac{\Sigma_{i=1}^{5\times5} w_i (i\phi_i - i\phi_{seed})^2}{\Sigma_{i=1}^{5\times5} w_i}, \qquad w_i = \max\left(0, 4.7 + \ln\frac{E_i}{E_{5\times5}}\right) \tag{6.2}$$

Since the beam halo photons having an elongated spread in η whereas the prompt photons have a more circular spread in $\eta \times \phi$ space, the variables chosen above are aimed to distinguish between the two classes by utilizing this difference in spatial pattern of energy deposition. The distributions for these variables are shown in Fig 6.6 for the two different samples. Both of the σ^2 variables are seen to have more separation power than the s_9/s_{25} variable. A combination of these three variables is expected to have better separation power. As a result these three shower shape variables are fed to an MLP which results in a background (beam halo photon) rejection rate to be around 71% for 99% signal efficiency shown in Table 6.1. It is noted that such low background rejection rate does not enable us to perform any useful analysis.

Table 6.1: Results for beam halo - prompt photon separation problem

Method	Number of parameters	Background rejection for 99% signal efficiency (%)	ROC AUC
CNN with image	13,199	99.96	0.9997
MLP with image	18,732	99.89	0.9990
MLP with 3 variables	206	71.31	0.9748

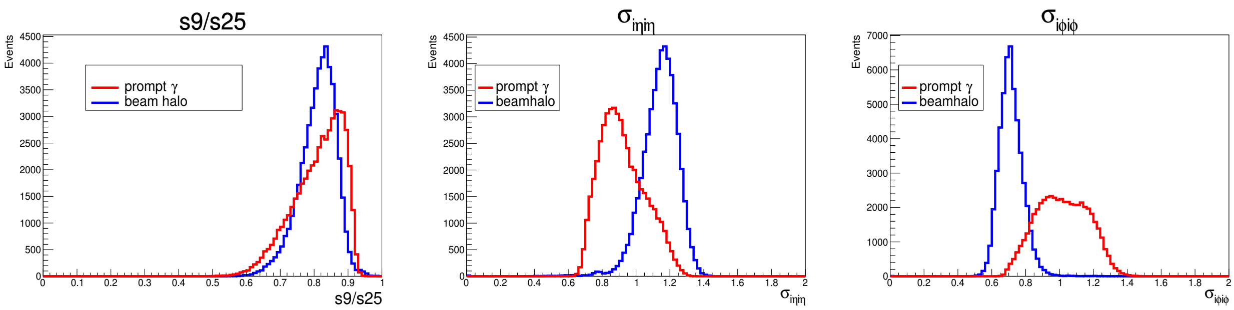

(a) (a) (b) (b) (c) (c)

Figure 6.6: Distribution of the shower shape variables for 10 GeV prompt photons and beam halo photons: (a) s9/s25, (b) $\sigma_{i\eta i\eta}$, and (c) $\sigma_{i\phi i\phi}$.

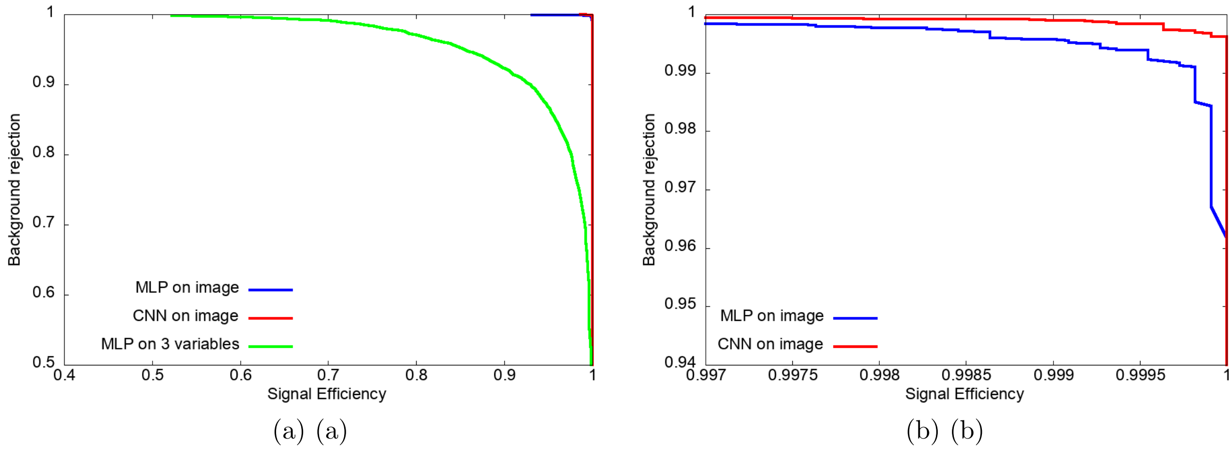

Figure 6.7: (a) ROCs for all methods which are used in separating prompt photons from beam halo photons, (b) A zoomed-in view of the ROCs which demonstrates that the CNN performs better than the MLP.

If a larger 11×11 image centered around the seed crystal is used in the MLP, the number of free parameters grow from around 200 to above 18000 compared to when just three representative shower shape variables constructed from 5×5 image are used . This however leads to a remarkable improvement in the background rejection rate from 71% to 99.89% and the method becomes a likely candidate for realistic analysis. Further, if a CNN of the same image size sample is used, the number of parameter reduces to about two thirds while the background rejection rate improves to 99.96% i.e the false positive rate reduces from 0.11% to 0.04% when CNN is used instead of MLP. Table 6.1 shows comparison of the networks. The corresponding ROCs are shown in Figure 6.7.

6.4.4 π^0- prompt photon separation

The sample of prompt photons has about 38% chance of getting converted into e^+e^- pairs leading to a different spatial pattern signature (Fig 6.1). The π^0 sample on the other hand has two photons, and the probability of at least on of them converting is about 61%. Keeping these additional differences in mind, the samples have been grouped into the following different sets:

- Set A $\rightarrow$ distinguish between converted and unconverted photons vs. converted and unconverted π^0's
- Set B $\rightarrow$ distinguish between unconverted photons vs. converted and unconverted π^0's
- Set C $\rightarrow$ distinguish between unconverted photons vs. unconverted π^0's

The CNN and the DNN have been both tested on these 25×25 images, and it is evident from the ROCs in Fig 6.9 that the CNN performs better than the DNN.

The following set of shower shape variables centered around the maximum energy seed crystal in a 5×5 cluster serves as the input to the DNN:

$$s_1/s_{25}, s_4/s_{25}, s_9/s_{25}, s_{16}/s_{25}, s_{nmax}, \sigma_{i\eta i\eta}, \sigma_{i\phi i\phi}, \sigma^2_{i\eta i\phi}, r_9$$

Table 6.2: Results for $\pi^0 - \gamma$ separation problem

Method	Number of parameters	Background rejection for 90.0% signal efficiency (%)	ROC AUC
DNN with 9 variables for set A	2,876	46.8	0.8196
DNN with image set A	433,460	73.4	0.8825
CNN with image set A	100,559	76.4	0.9030
CNN with image set B	100,559	92.5	0.9567
CNN with image set C	100,559	97.7	0.9848

Along with variables which have been already defined in section **??** others are: s_1 which is the energy of the seed crystal, s_4 which is the maximum energy deposited within a 2×2 matrix containing the seed crystal, s_{16} which is the maximum energy deposited within a 4×4 matrix containing the seed crystal, s_{nmax} which is E_i/E_{seed} where E_i is the energy of the crystal adjacent to the seed crystal having the next highest energy and E_{seed} is the energy of the seed crystal, r_9 which is the ratio of s$_9$ with the energy in the 25×25 matrix centered around the seed crystal, and

$$\sigma^2_{i\eta i\phi} = \frac{\Sigma_{i=1}^{5\times5} w_i(i\eta_i - i\eta_{seed})(i\phi_i - i\phi_{seed})}{\Sigma_{i=1}^{5\times5} w_i}, \qquad w_i = \max\left(0, 4.7 + \ln\frac{E_i}{E_{5\times5}}\right) \tag{6.3}$$

The distributions of each of these different variables for photons and π^0's of set A are shown in Figure 6.8.

The above variables however do not have much distinguishing power which can be seen from the ROCs in Figure 6.9 as well as from Table 6.2 where the DNN trained with these variables perform the worst at 46.8% background rejection. A much better background rejection of 73.4% comes from the DNN trained on the images , but that comes at a higher computational cost where 150x more parameters are used. The CNN fed with the images gives a marginal (3%) increase in background rejection but it also uses about a quarter of the number of parameters. We get the best signal and background separation for Set C, where prompt photon and photons from π^0 are both unconverted leading to a much purer sample it is noted that this is with just the calorimeter information. With tracker

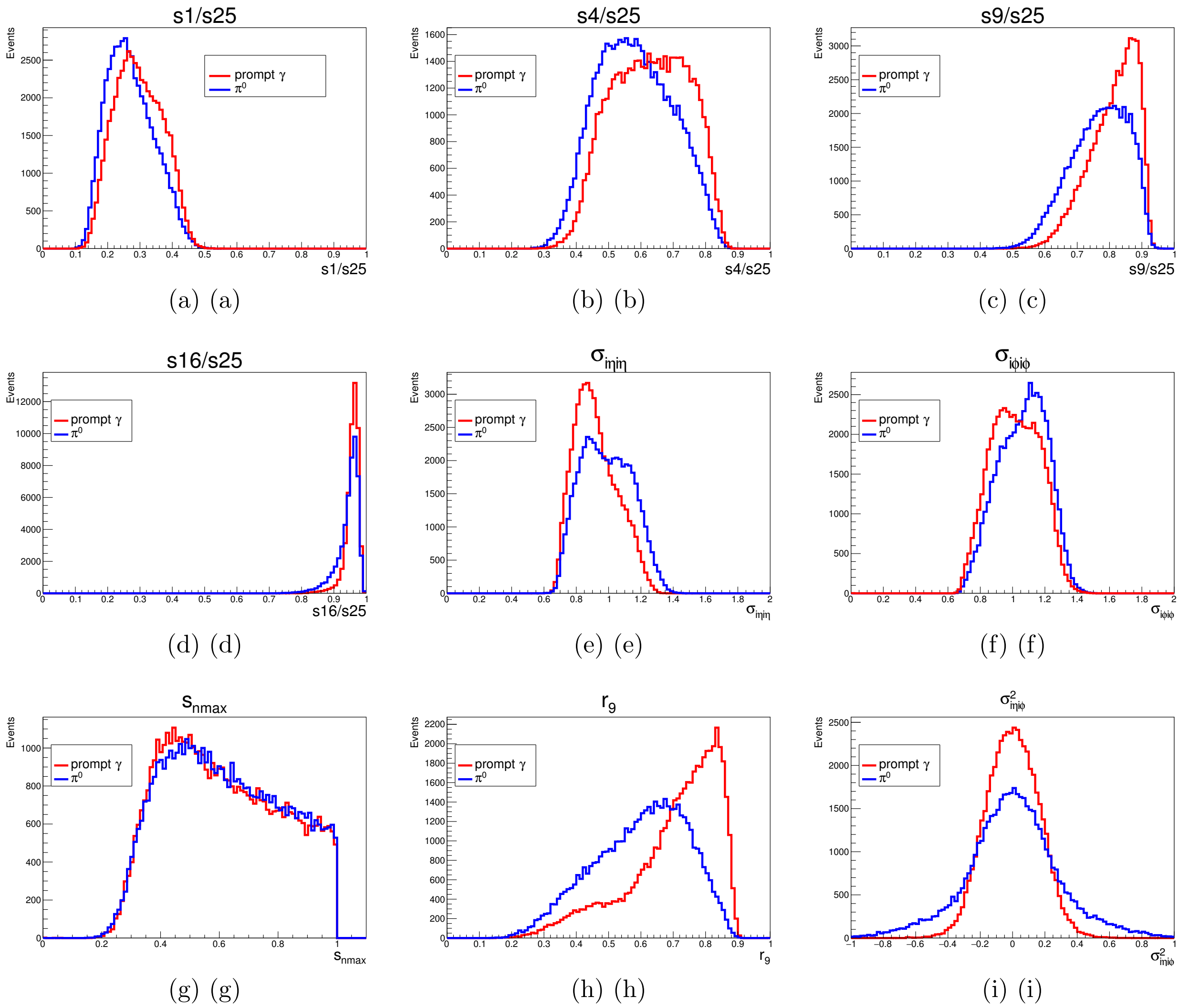

Figure 6.8: Distribution of the shower shape variables of prompt photons and π^0's corresponding to set A:
(a) $s1/s25$, (b) $s4/s25$, (c) $s9/s25$, (d) $s16/s25$, (e) $\sigma_{i\eta i\eta}$, (f) $\sigma_{i\phi i\phi}$, (g) s_{nmax}, (h) r_9, and (i) $\sigma^2_{i\eta i\phi}$.

information used in addition for both Set A and B, much better background rejection numbers are expected for them. Table 6.2 lists the background rejection, signal efficiency and the area under the curve of the ROCs.

6.5 Conclusion

This study utilizes deep learning techniques for separating prompt photons from neutral pions and beam halo. Varius types of networks have been compared with simulation data generated from an approximated CMS detector geometry consisting of a tracker and a calorimeter.

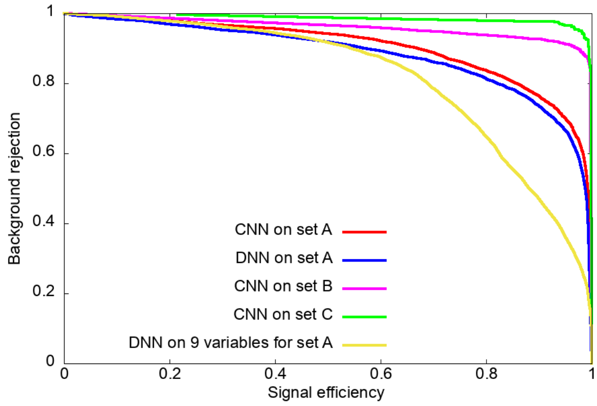

Figure 6.9: ROCs for all the methods used for the separation of π^0s and prompt photons.

For the problem of separating photons from beam halo the maximum background rejection of 99.96% for 99.00% signal efficiency comes from CNN based on image. For the problem of separating neutral pions from prompt photons the maximum background rejection of 97.7% for 90.0% signal efficiency comes from CNN based on image. For both of the cases ROC AUCs clearly indicate that the CNN outperforms the MLP or DNN with the same input image and also the MLP or DNN using topological variables.

For the beam halo separation problem since the spatial pattern of the prompt photon and beam halo photon are very distinct, a simple one layered MLP is found to be sufficient to do a classification with high accuracy. The $\pi^0 - \gamma$ classification on the other hand poses a more difficult problem since the energy deposition patterns of the π^0 decay photons and a prompt photon are very similar. The CNN in any case is found to give a good performance on unconverted photons vs. unconverted π^0's. These techniques of trying to classify physics objects using neural networks based on images are generic and can be applied to any calorimeter.

Chapter 7

Calibration of the Hadron Calorimeter With Isolated Charged Hadrons

7.1 Methodology

The CMS Hadron Calorimeter (HCAL) has a non-linear energy response for the hadrons and this effect becomes more prominent at lower energies. The HCAL energy is set with 50 GeV hadrons since in this region the calorimeter response is a slowly changing function of energy. The isolated charged hadrons provide an important tool in the areas which are covered by the tracking system. The tracking system enables the measurement of momentum of the charged particles with high precision which can be associated to their corresponding energy deposit in the calorimeter.

Signal and isolation regions are defined by constructing cones around the track direction. Signal is measured from HCAL cells within a cone of radius (R_{Cone}) 35.0 cm which on average contains more than 99% of the energy deposited by a 50 GeV hadron. In order to ensure that the particles have not interacted before reaching the calorimeter, MIP-like signal in the preceding ECAL is required. The response of the calorimeter is defined as a ratio :

$$\frac{E_{HCAL}}{p_{Track} - E_{ECAL}} \tag{7.1}$$

where E_{HCAL} is the energy measured in the HCAL cluster within R_{Cone} around the impact point at HCAL, p_{Track} is the momentum of the track measured in the tracker and E_{ECAL} is the energy deposited in a cone of radius 14 cm around the impact point in the ECAL. The most probable value (MPV) of the response is obtained using Gaussian fits to the distribution of the response. Isolation conditions are imposed to ensure least contamination from unrelated energy depositions. Charge particle isolation is implemented by propagating charged particle tracks to the calorimeter surface in a cone around the impact point and rejecting candidates for whom there are additional tracks above a certain threshold in that cone.

7.2 Data Sources

For this method, there are two sources of data:

- Dedicated High Level Triggers separately for barrel and endcap calorimeters are used to pre select events.
- A filter is applied on four primary data sets like JetHT, DoubleEG, SingleElectron and HLT Physics to select events.

The HLT is seeded by a single jet Level 1 trigger followed by selection modules which ensure the selection of

- well isolated track using only charge isolation
- MIP signal in the ECAL
- Well measured momentum above 20 GeV.

Prescale factors both at the L1 and HLT level are set such that data taking bandwidth is not saturated and also timing constraints of HLT are maintained. The 2 trigger paths are named HLT IsoTrackHB and HLT IsoTrackHE and they provide a rate of $\sim 5Hz$. The offline filter employs soft isolation so that a variety of analysis can be performed with the resulting data. Around $2-3\%$ of the data pass tight isolation criteria. From the combined output of the 4 data streams $\sim$ 6000 tracks are expected from 1 fb^{-1} of data with about 500 tracks in the range of 40–60 GeV.

7.3 Event Selection

Selections for the events pre-selected by the HLT as well as the filter have been discussed above. Particles with the momentum range of 40–60 GeV are selected and the transverse momentum p_T is required to be greater than 7 GeV. Further important selections are discussed below.

7.3.1 Primary vertex and track reconstruction quality

Events are selected where there is at least one well reconstructed primary vertex close to the nominal interaction point within $\Delta r \equiv \sqrt{x^2 + y^2} < 2$ cm and $\Delta z < 15$ cm. Tracks are required to be of "high purity" and also required to be associated with a primary vertex. Track selection criteria are:

- The track has to be within 200 μm from the event vertex both in transverse and longitudinal direction.
- χ^2 of the track fit has to be less than 5.
- Minimum number of layers crossed by the track is 8.

Since it is important to ensure that the tracks do not interact before reaching the calorimeter, the number of missing hits in inner and outer hit pattern of reconstructed hits are considered and tracks with missing hits are rejected.

7.3.2 Requirement of MIP in the ECAL

Since the ECAL corresponds to about one nuclear interaction length more than half of the hadrons undergo inelastic interactions in the ECAL. These hadrons are not used for calibration. MIP condition is ensured by requiring the energy measured in the ECAL in a cone of radius 14 cm around the impact point of track to be less than 1 GeV. This also removes neutral particles which can have overlapping signals with the candidate track in HCAL.

7.3.3 Charged particle isolation

To ensure the isolation of the selected cluster candidate associated with the selected track, a strong requirement is needed on the isolation from the neighbouring charged particles. But a strong isolation criteria also leads to lower selection efficiency in the endcap for high pileup (PU) conditions and hence the isolation conditions are loosened and a technique for PU correction is developed.

7.3.3.1 Tight Charge Isolation

Tight isolation requires that no track of any quality having hits in more than 4 layers of the tracker along with $p > p_{cut}$ (= 2 GeV) is within a radius of 64 cm around the impact point of the isolated track. Fig7.1 shows the efficiency of the strong isolation cut for single pion sample with and without PU. For PU samples, the efficiency starts decreasing from

$|i\eta| = 10$. Fig 7.2 shows the MPV of the response as a function of $i\eta$ of the selected track. MPV of response is obtained from a Gaussian fit to the response distribution.

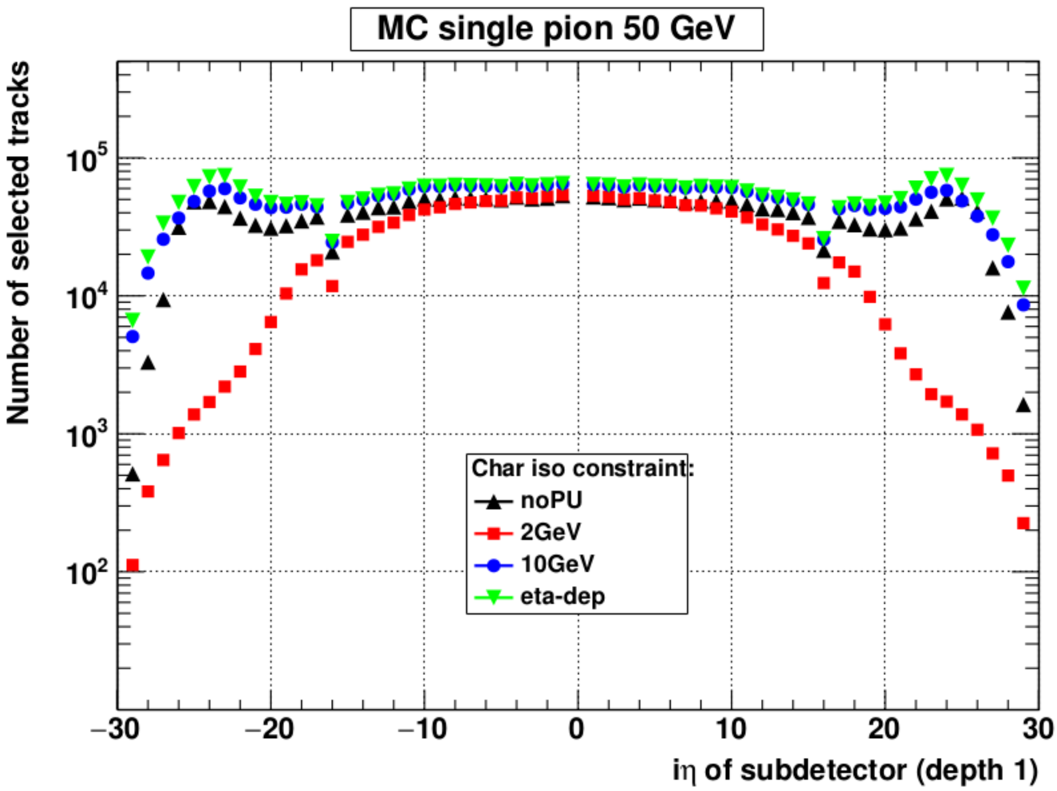

Figure 7.1: Number of selected isolated tracks for each subdetector at depth 1 from MC samples of single pions. Black triangles correspond to the sample with no PU while the other three are the effects of isolation cuts on PU sample.

7.3.3.2 Loose Charge Isolation

Very few events are selected in the endcap regions when the tight isolation criteria is applied. Instead one can use looser constraint on p_{cut} or a η dependent criteria:

$$p_{cut} = 8 * exp(\frac{|i\eta| * log(2.5)}{18}) \tag{7.2}$$

The looser criteria helps to increase the number of tracks selected for calibration as seen in Fig7.1 for $p_{cut} = 10$ GeV as well as the η dependent cut. The criterion with $p_{cut} = 10$ GeV is used since both the criteria give similar efficiency. When using loose selection, the pileup contribution results in overestimation of the response as shown in Fig7.2. Compensation is achieved by correcting the measured energy using a parametrization as described in later sections.

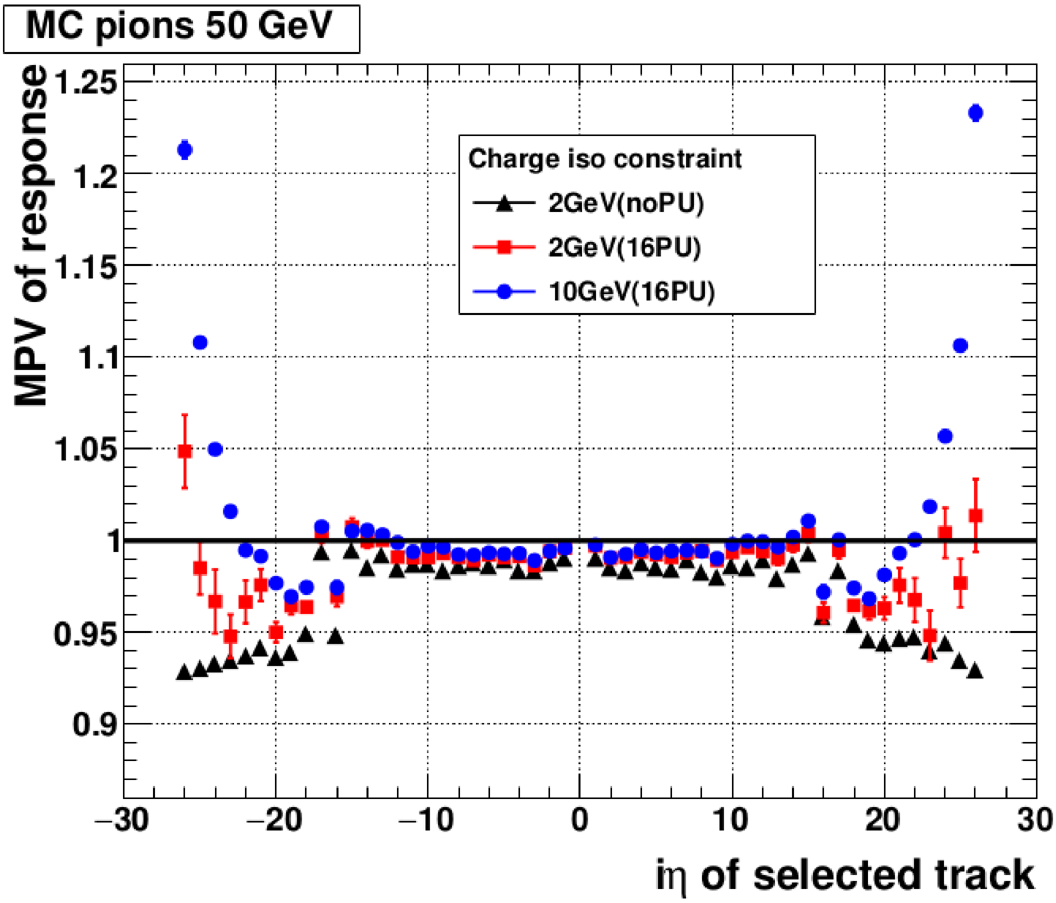

Figure 7.2: Most Probable Value of the response distribution as function of the $i\eta$ of incoming track for different isolation constraints.

7.4 Response distributions

The selected isolated tracks are divided according to $i\eta$ of the impact point of the track on the HCAL surface. The MPV's of their distribution are plotted. Fig 7.3 shows the distributions as a function of $i\eta$. The plot on the left shows the distribution with tracks selected by the HLT while the plot on the right shows the plot for the events selected by the filter. It can be seen from the figure that the mean ratio is consistent with 1 over almost the entire $i\eta$ region with some deviation from 1 in the endcap region.

7.5 Pileup Correction Method

The contamination in the energy of hadrons due to PU varies both with time as well as location in $\eta - \phi$ space. For different PU levels there can be large or no PU contribution to the pion energy. To overcome these variations energy deposit near the signal cone is considered within some annulus beyond the cone. The annulus is bounded with the radii

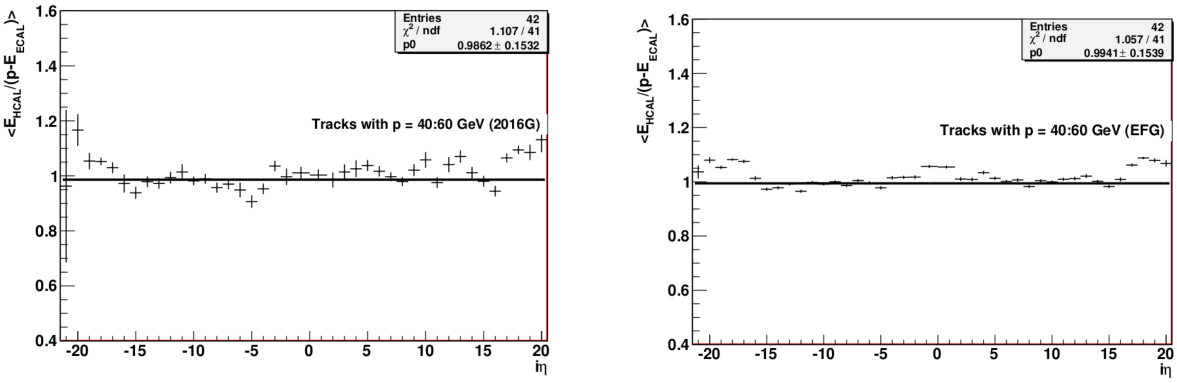

(a) (b)

Figure 7.3: Distribution of MPV as a function of iη for (a) events selected by HLT and (b) events selected by the filter.

R_{cone} + 10 cm and R_{cone} + 30 cm where R_{cone} = 35 cm. This allows disregarding the shower fragments outside the basic cone and focus on the PU correction. The outer radius is 65 cm which is similar to that used in charge isolation selection for the isolated track. The following formula is used to correct for the PU in an event-by-event basis:

$$E_{corr} = E * (1 + a1 * \frac{E}{p} * (\frac{\Delta}{p} + a2 * (\frac{\Delta}{p})^2)) \quad (7.3)$$

where E is the energy in the signal cone, p is the track momentum and Δ is the energy deposit in the annulus around the main cone discussed above. Values for $a1$ and $a2$ are extracted by using the dependence of the response on the ratio $\frac{\Delta}{p}$. Values of ($a1$,$a2$) are (-0.35,-0.65) for $|i\eta| < 25$. The region near the boundary of tracker coverage is more complicated and the values are (-0.35,-0.30) for $|i\eta| = 25$ and (-0.45,-0.10) for $|i\eta| > 25$ are adjusted by hand.
Fig7.4 shows the MPV distribution of the response function. Event-by-event PU correction in the way discussed above on loose isolation gives similar response to that of no-PU single pion samples.

7.6 Calibration Method

In order to calibrate a region of HCAL channels, for each event the energy response of the isolated cluster is calculated as the sum of hits in the cone around the impact point of the track with contributions from the MIP energy in ECAL and is compared to the momentum measured in the tracker. The aim of this calibration is to obtain correction factors c_i (i is the index of each sub-detector) for each of the HCAL sub-detectors which makes the MPV of response closer to 1.

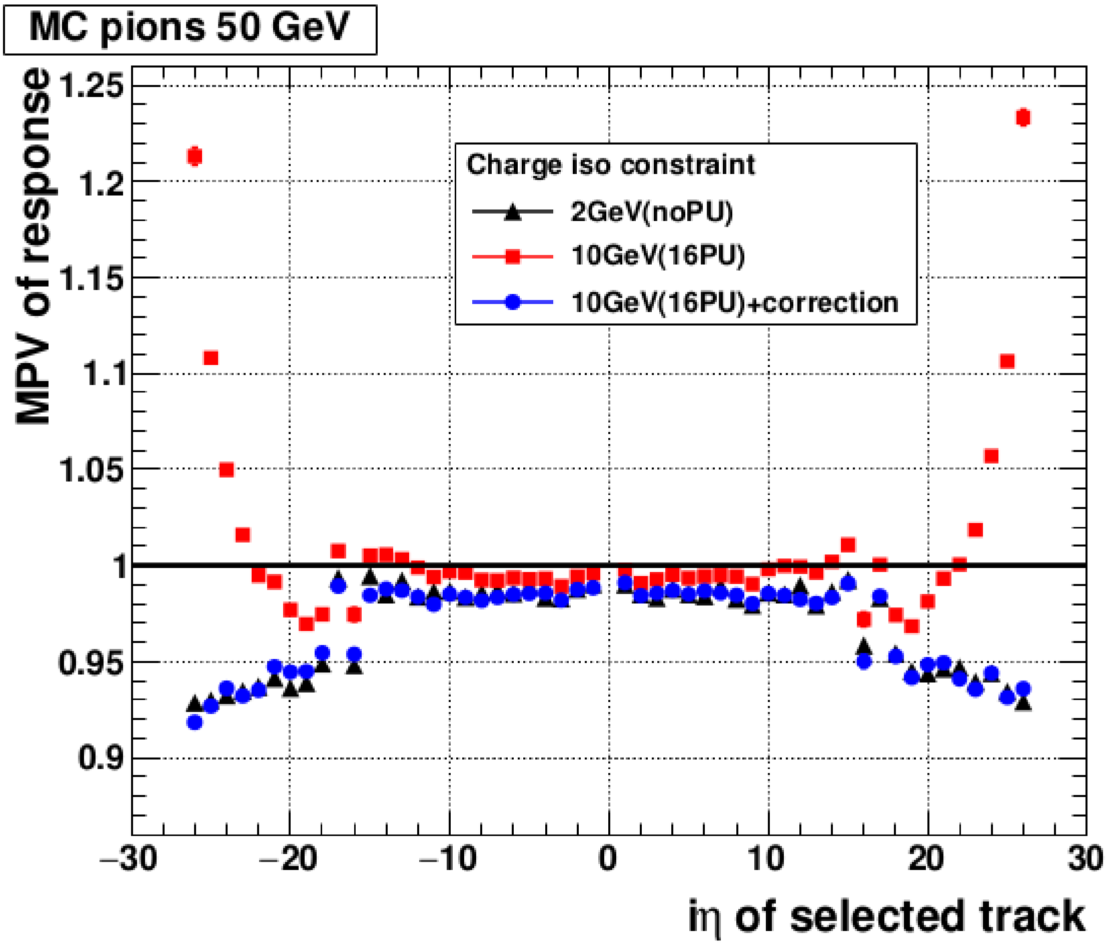

Figure 7.4: Most Probable Value of the response distribution as function of the $i\eta$ of incoming track showing the effect of PU corrections.

7.6.1 Iterative Procedure

The method used for calibration has an iterative approach. At the m-th iteration, a new correction factor c_i^{m+1} is calculated using two possible options:

$$c_i^{m+1} = c_i^m \left(1 + \frac{\sum_j w_{ij}^{(m)} * \left(\frac{p_j}{E_j^{(m)}} - RR\right)}{\sum_j w_{ij}^{(m)}}\right) \tag{7.4}$$

$$c_i^{m+1} = c_i^m \left(1 + \frac{\sum_j w_{ij}^{(m)} * \left(\frac{E_j^{(m)}}{p_j} - RR\right)}{\sum_j w_{ij}^{(m)}}\right) \tag{7.5}$$

where the sum is over j events which contribute to the i-th sub-detector, RR is the reference response to which the mean response should be equalized, p_j is the track momentum, $w_{ij}^{(m)}$ is the weight of the sub-detector in the cluster energy $E_j^{(m)}$:

$$w_{ij}^{(m)} = \frac{c_i^{(m)} * e_{ij}}{E_j^{(m)}}, E_j^{(m)} = \sum_{i=1}^{n_j} c_i^{(m)} * e_{ij} \tag{7.6}$$

From the above two options, the iterative process equalizes the mean response of the detector around the value RR which is 1 by default. If the most probable value for the sample differs from the sample mean, the reference response should be set to $RR = \frac{MEAN}{MPV}$. .The statistical uncertainty is estimated from the RMS of the response distribution for the subsample used for the i-th sub-detector.

$$\Delta C_i^{(m+1)} = \Delta R_i^{(m)} * \frac{\sqrt{\sum_j (w_{ij}^{(m)})^2}}{\sum_j w_{ij}^{(m)}} \tag{7.7}$$

The iterative process is repeated until the difference between coefficients at subsequent steps becomes three times smaller than the statistical uncertainty.

7.6.2 Single Pion samples tests

The convergence of the iterative procedure has been tested with simulated samples of single pions at 50 GeV. I has been observed that equation 4.4 causes a bias in the response ratio distribution whereas equation 4.5 is much more stable. Convergence is achieved after 20 to 30 iterations. Initial values of the correction factors (CF's) are set to be 1.

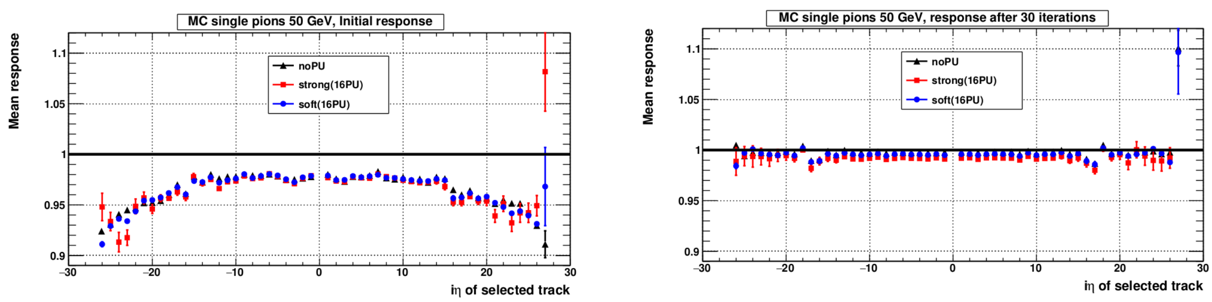

(a) (b)

Figure 7.5: Distribution of MPV as a function of iη for (a) before iteration and (b) after iteration.

Fig7.5 shows equalization of the mean response after 30 iterations for the samples with and without PU using tight and loose charge isolation. The iterative procedure results in the equalization of mean response at the level of $\sim 1\%$. The correction factors for with and without PU are in agreement within $\pm 2\%$. The effect of the uncertainty in the track momentum measurement on the estimation of the correction factor is tested using the simulated pion samples and replacing the measured track momentum with the generator level track momentum. The difference in correction factors is observed at the level of 0.1%.

7.7 Calibration on Run II data samples

The calibration procedure is applied to the collision data collected during the 2016 data taking period. Different calibration options were tested and correction factors for different data taking periods were compared.

7.7.1 PU correction cross-check

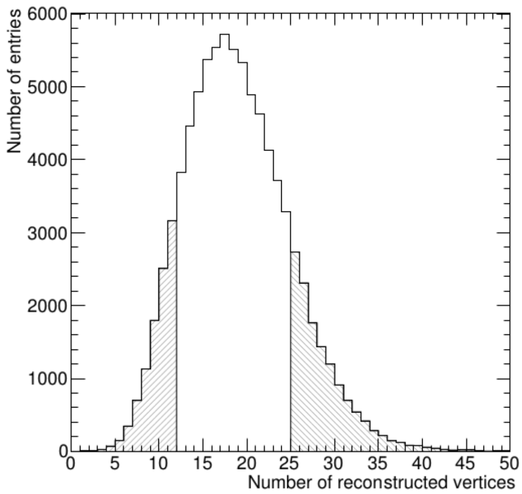

(a)

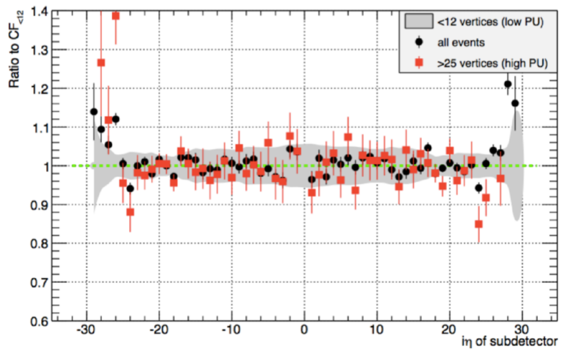

(b)

Figure 7.6: (a) Distribution of N_{vtx} from the JetHT 2016 G data set and (b) Ratio of correction factors extracted from the entire sample and from the sub-samples with $N_{vtx} > 25$ (red squares) to the factors extracted from the sub-sample with $N_{vtx} < 12$. Uncertainties for the sample with $N_{vtx} < 12$ are shown with gray band.

A cross check to the PU correction is performed using subsamples corresponding to events having different number of reconstructed vertices (N_{vtx}). The distribution of N_{vtx} for the events selected using loose charge isolation constraint from the sample 2016 G is shown in Fig7.6. The correction factors are extracted from the entire sample as well as subsamples with low PU ($N_{vtx} < 12$) and high PU ($N_{vtx} > 25$). Fig 7.6 shows the ratio of correction factors obtained from the entire sample and from the two subsamples. Though the subsamples with low and high PU show different results at $|i\eta| > 25$, the correction factors for the entire sample agree within uncertainties with those for the subsample with low PU.

The application of the loose charge isolation along with the PU correction described in previous sections gives a possibility to get $\sim$7 times more statistics for calibration in the barrel (HB:$|i\eta| < 14$) and in the transition region (TR: $15 \leq |i\eta| \leq 17$) and more than 40 times larger statistics in the endcap region (HE: $18 \leq |i\eta| \leq 26$) compared to tight charge isolation. With L3 iterative procedure, equalization within $\pm 1.5\%$ is achieved for subdetectors up to $|i\eta| \leq 25$.

7.7.2 Extracted correction factors

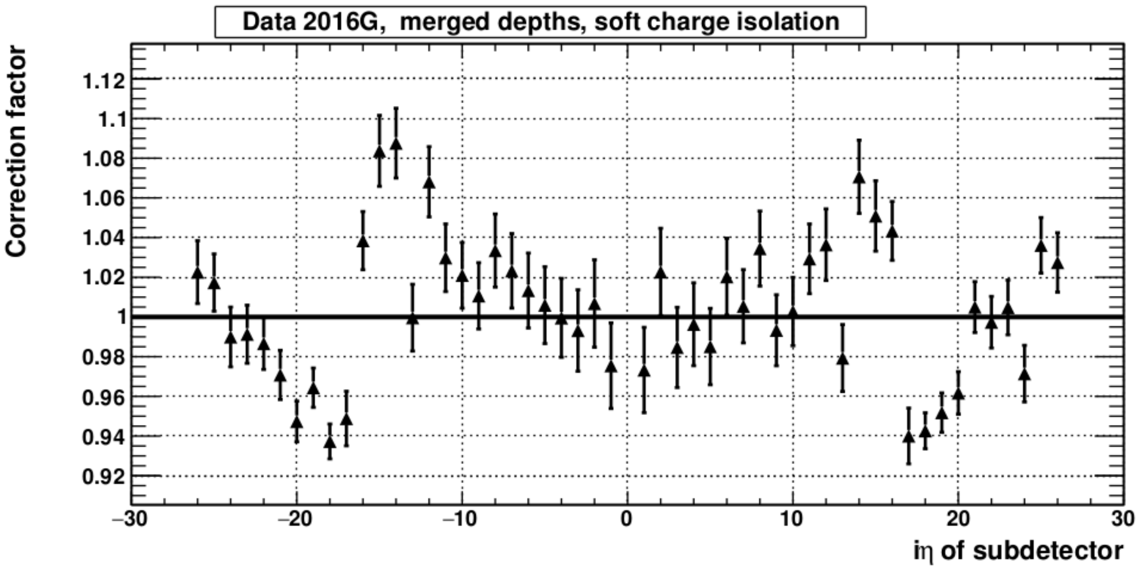

Figure 7.7: Correction factors which are extracted from the 2016 G data sample. The correction factors are assumed to be the same for different depths from the same $|i\eta|$ ring.

The extracted correction factors are shown in Fig7.7. The statistical uncertainty in the correction factors from the samples 2016 D, E, G is below 1%. Fig 7.8 shows the ratio of correction factors from the samples 2016B and 2016E to the factors extracted from the sample 2016 G. The correction factors from samples 2016E and 2016 G agree within uncertainties, while the factors from the sample 2016B tend to be lower in the barrel region by $\sim 3\%$.

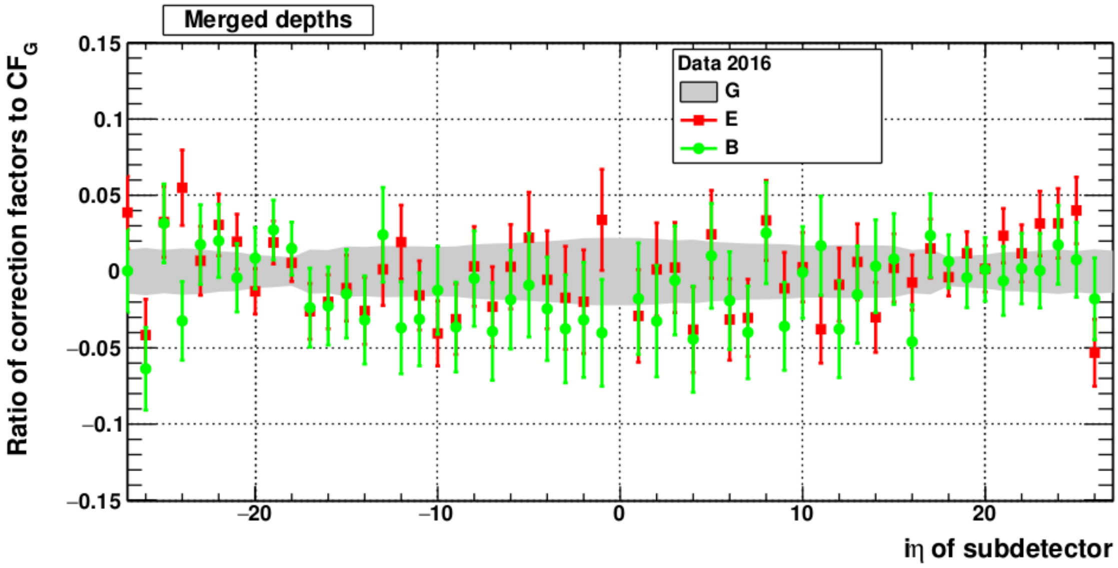

Figure 7.8: Ratio of correction factors extracted from 2016 B and 2106 E data samples to the factors extracted from the 2016 G sample. The correction factors are assumed to be the same for different depths from the same $|i\eta|$ ring.

7.8 Conclusion

Energy scale factors for barrel and endcap hadron calorimeter are studied and estimated using isolated charged hadrons from the 2016 collision data. Selection of well isolated charged hadrons on the calorimeter surface leads to very few tracks in the endcap calorimeter which is mitigated of by making the isolation criteria relaxed and using a correction procedure for overlapping showers from PU a method tuned using Monte Carlo samples. An iterative method is developed for obtaining the correction factors for a given hadron calorimeter tower which is used to obtain correction factors from 2016 data. Pile-up dependence are studied and are properly taken into account in the process of estimating the correction factors. These extracted correction factors were used in the legacy re-reconstruction of the 2016 data which is took place in early 2017.